

PHOTOLITHOGRAPHIC FABRICATION OF ELECTROACTIVE
POLYMER MICROSTRUCTURES AND ELECTROCHEMICALLY
MODULATED OPTICAL DIFFRACTION GRATINGS

By

TROY S. BERGSTEDT

A DISSERTATION PRESENTED TO THE GRADUATE SCHOOL
OF THE UNIVERSITY OF FLORIDA IN PARTIAL FULFILLMENT
OF THE REQUIREMENTS FOR THE DEGREE OF
DOCTOR OF PHILOSOPHY

UNIVERSITY OF FLORIDA

1999

For Paula and “Little B”

ACKNOWLEDGEMENTS

If we weren't all crazy, we would go insane...
Jimmy Buffett

I owe a great debt of gratitude to my research advisor, Kirk Schanze, for instructing me in the ways of science, guiding me through the rough spots, sharing the triumph of new discoveries, lighting a fire under me when it was necessary, and occasionally helping me to put one out. A tribute is also to be paid to the Schanze group members with whom I have had the pleasure of crossing paths, including Lucian Lucia, Nancy Thornton, Yingsheng Wang, Rich Burton, and Kevin Ley. Special thanks go to my labmate, roommate, and brother-in-arms, Brian Hauser, who struggled along beside me during those times when *nothing* seemed to work. I would also like to thank John Reynolds for his experience and advice, which were critical elements of the work in Chapter 4.

I would like also to thank my parents, Kenneth and Linda, for their enduring support, encouragement, faith, and pride in me and my efforts.

And finally, I thank my beautiful wife Paula, who endured the life of a grad school widow, followed me across the country, and stood beside me all the while. Without her in my corner, none of this would have been possible.

TABLE OF CONTENTS

ACKNOWLEDGEMENTS	iii
ABSTRACT	vi
CHAPTERS	
1 INTRODUCTION	1
Objective and Introductory Concepts	1
Chemically Modified Electrodes	1
Lithography	7
Diffraction Gratings	10
2 OPTICAL DIFFRACTION GRATINGS FABRICATED FROM A POLYPYRIDYL RUTHENIUM(II) REDOX POLYMER	15
Introduction	15
Results	18
Photopolymer Film Fabrication	18
Electrochemistry and Spectroelectrochemistry	28
Quantification of Electrode Surface Coverage	33
Diffraction Experiments	40
Refractive Index Determination	43
Discussion	45
Film Characterization	45
Diffraction Experiments	54
Experimental	60
Chemical Syntheses	62
Electrochemical/Optical Experiments	64
3 MIXED AMPLITUDE / PHASE GRATINGS BASED ON A BENZYLVIOLGEN MOIETY	66
Introduction	66
Results	68
Photopolymer Film Fabrication	68

Electrochemistry and Spectroelectrochemistry	72
Quantification of Electrode Surface Coverage	82
Extinction Coefficients	88
Diffraction Experiments	89
Refractive Index Determination	100
Electrolyte Effects	103
Discussion	105
Film Morphology	105
Electrochemistry	108
Spectroelectrochemistry	109
Diffraction Efficiency Modulation	110
Experimental	115
Synthesis of Vinylbenzylviologen (VBV ²⁺)	116
Electrochemical/Optical Experiments	117
4 TRANSMISSION GRATINGS BASED ON ELECTRONICALLY CONDUCTIVE POLYTHIOPHENE	118
Introduction	118
Results	121
Synthesis	121
Photolithography	124
Film Characterization	125
Diffraction Experiments	132
Discussion	139
Film Characterization	139
Diffraction Experiments	142
Experimental	149
Syntheses	150
Electrochemical/Optical Experiments	155
Film Preparation/Lithographic Patterning	156
Electropolymerization	156
APPENDIX	158
REFERENCES	163
BIOGRAPHICAL SKETCH	170

Abstract of Dissertation Presented to the Graduate School
of the University of Florida in Partial Fulfillment of the
Requirements for the Degree of Doctor of Philosophy

PHOTOLITHOGRAPHIC FABRICATION OF ELECTROACTIVE
POLYMER MICROSTRUCTURES AND ELECTROCHEMICALLY
MODULATED OPTICAL DIFFRACTION GRATINGS

By

Troy S. Bergstedt

August, 1999

Chairman: Professor Kirk S. Schanze
Major Department: Chemistry

A photolithographic methodology has been employed to prepare thin polymer films of electrochemically active materials on a conductive, optically transparent substrate. These films are patterned within the plane of the substrate with feature linewidths on the order of several microns. Three types of films are described, one prepared from a polypyridyl ruthenium (II) monomer having acrylate functionality, one employing a styrene-based viologen monomer, and the third comprised of a polythiophene with pendant acrylate functionality.

Upon adsorption onto the electrode surface, these materials largely retain their electrochemical and spectroelectrochemical characteristics. Grating-patterned arrays of these electroactive materials possess an additional interesting characteristic, the ability to

diffract light in a manner which can be reversibly controlled by a chemical or electrochemical signal. The chemical synthesis, photolithographic film fabrication technique, characterization, and diffraction experiments will be presented and discussed.

CHAPTER 1 INTRODUCTION

Objective and Introductory Concepts

Often, when one sets out in pursuit of a particular goal, the journey may be sidetracked so that the final destination is quite different than had been initially projected. With the intent of investigating materials to be employed for a photoinduced charge transfer scheme, we (perhaps fortuitously) found that these polymers, when deposited onto transparent electrodes in spatially addressable three-dimensional structures, possessed unexpected optical properties. It was discovered that grating patterned arrays of electroactive polymer stripes exhibited optical diffraction properties which could be varied by a reversible electrochemical stimulus. The work detailed in the following chapters chronicles our path along this tangent. While chapters 2-4 describe the properties of differing materials, three key concepts remain common throughout, namely the utility and electrochemical properties of chemically modified electrode surfaces, photolithography, and optical diffraction gratings. Due to the importance of these subjects to the discussion of the work to follow, a brief introduction of each is appropriate.

Chemically Modified Electrodes

By deliberate adsorption of a chemical species onto an electrode surface, one can produce a chemically modified electrode (CME) in which the chemical, electrochemical,

optical, spectroscopic, and other properties are imparted to the electrode.^{1,2} By appropriate selection of the adsorbed molecular species, the electrode can be made to possess the selective characteristics suitable for a diverse range of specific applications. For example, an electrocatalytic surface can be obtained by functionalization of the electrode surface with molecules that can sensitize an oxidation or reduction of a chemical species in the contacting electrolyte solution. By the same token, this type of electrode can be employed rather in an analytical sense, to detect the presence and/or concentration of a dissolved analyte by measurement of the current flow to or from the electrode. Surface adsorption also allows for practical utilization of a material's spectroscopic properties, both absorptive and emissive.³ Potential real-world applications in this regard include electrochromics,^{4,5} photodetection,^{6,7} and electroluminescence.

In addition to consideration of the specific molecular species with which to functionalize an electrode surface, one must determine the manner in which the material is to be deposited. As the study of CMEs has grown, so has the number of surface modification strategies. These can be categorized into two general classes, based on the amount of material residing on the electrode surface: monolayer films and multilayer or polymer films. As the name implies, a single molecular layer of adsorbed or chemically bound chemical species (essentially creating a two-dimensional molecular regime) characterizes the former. Langmuir-Blodgett deposition techniques employ hydrophobic ordering and adsorption effects to create well-ordered, compact films⁸⁻¹⁰ (by extension of this procedure, multilayer films can be prepared as well by sequential depositions). A second strategy for monolayer coverage is chemisorption, exemplified by the tendency of

alkenes to irreversibly adsorb onto platinum,¹¹ as well as a similar affinity of aromatic π systems for carbon surfaces.¹² Self-assembled monolayers (SAMs) have been studied extensively, and can also form very stable surface films. The self-assembly technique relies on a reactive pendant tether which attaches molecules to the surface by covalent bonding with the electrode material. The two most widely employed attachment strategies are thiol self-assembly on gold surfaces¹³⁻¹⁷ and silane attachment to metal oxide surfaces.^{6,18-26}

While monolayer films are generally very well defined and can exhibit ideal electrochemical behavior, the main drawback is the very small amount of material deposited on the electrode surface, which precludes practical use in all but the most sensitive analytical applications. This, in large part, has fueled the growth of films comprised of multilayer quantities of adsorbed material. Here, again, several approaches are possible. Polymers can be grown directly on the surface by means of electropolymerization, or preformed polymers can be deposited by spin-casting, dipping, or drop evaporation. The electrochemically active species can comprise the backbone structure of the polymer as in the case of electronically conducting polymers (so-called synthetic or plastic metals), it may be attached pendant to a nonconductive backbone (redox-conductive polymers), or it may be electrostatically bound to an oppositely charged host polymer (e.g. a cationic species ion-exchanged into polystyrene sulfonate^{27,28}). While there are benefits to be reaped in employing a polymeric CME for a desired application, care must be taken in order to maintain favorable electrochemical properties. As is often observed, multilayer quantities of adsorbed material can inhibit the electrochemical response of the electrode in degrees ranging from

trivial to severe in magnitude. In order to understand this, let us first look at an ideal model, fully reversible cyclic voltammetry of a thin layer of a redox-active material. A schematic representation of this is shown in Figure 1.1.^{1,2}

For an ideal redox layer immobilized on an electrode surface, both transport of the redox center to the site of the electron transfer reaction and the electron transfer step itself are fast. The Ox/Red composition of the redox film maintains equilibrium with the applied potential, which obeys the Nernst equation at all E_{app} . For $\text{Ox} + n\text{e}^- \rightarrow \text{Red}$,²⁹

$$E = E^\circ + \frac{RT}{nF} \ln \frac{C_O}{C_R} \quad (1-1)$$

Both the reductive and oxidative current peaks are symmetrical about the peak current and the same in both directions. For a reductive wave, the current is given by^{2,29}

$$i = \frac{-4i_p \exp\left[\left(nF/RT\right)(E - E_{surf}^\circ)\right]}{\left\{1 + \exp\left[\left(nF/RT\right)(E - E_{surf}^\circ)\right]\right\}^2} \quad (1-2)$$

The current peak i_p appears at the surface wave formal potential E_{surf}° and is given by

$$i_p = \frac{(nF)^2 A \Gamma_T v}{4RT} \quad (1-3)$$

where F is the Faraday constant, A is the electrode area, v is the potential scan rate, and Γ_T is the total electroactive coverage of the film:

$$\Gamma_T = \Gamma_{Ox} + \Gamma_{Red} = VC_{Ox} \quad (1-4)$$

Instead of calculating the surface coverage based on the resting-state film volume V and the concentration of oxidized species C_{Ox} , for which exact values can be quite uncertain, it is more common to calculate Γ_T by integration of the total charge Q under the current wave shown by the shaded region in Figure 1.1 (Equation 1-5). Care must be taken to

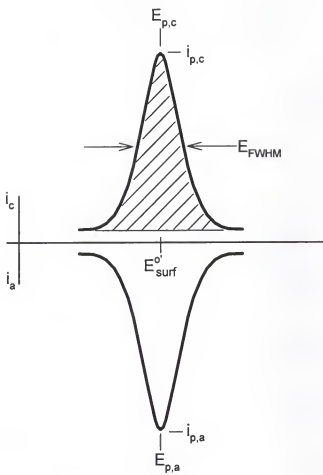


Figure 1.1. Characteristics of an ideal cyclic voltammogram for a surface-confined redox species. (Reference 1)

$$\Gamma_T = \frac{Q}{nFA} \quad (1-5)$$

ensure that the proper baseline is established in order to properly determine the charge under the current wave, as the wave is often superimposed atop a double-layer charging current (the vertical displacement of the two surface waves shown in the figure).

The significant diagnostic features³⁰ of the cyclic voltammogram shown in Figure 1.1 are identical reductive and oxidative peak potentials ($\Delta E_p = 0$), symmetrical shapes for both reductive and oxidative surface waves, proportionality between the peak current i_p and the potential sweep rate v , the integrated charge Q (and thus Γ_T) is constant and independent of v , and a peak width E_{FWHM} of $90.6/n$ mV.

In practice, however, fully ideal behavior is seldom observed. Compared to the analogous description for solution-phase voltammetry, equation 1-3 lacks a term to describe diffusion effects. This is appropriate for a thin-layer model, because since the redox species is immobilized on the electrode surface, molecular diffusion to the electrode surface is obviated. In the case of a thicker redox polymer film, though, electron transfer occurs through site-site hopping and charge percolation to the more remote regions of the film (see Figure 1.2). This requires molecular motion within the

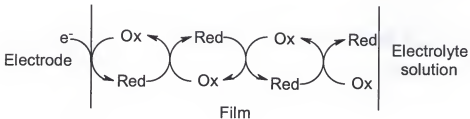


Figure 1.2. Charge percolation through a redox conductive film.

constraints of the film so that the oxidized and reduced film species can come in close proximity to facilitate electron transfer. In addition, charge neutrality must be maintained within the film during the redox process, so charge-compensating electrolyte ions and solvent molecules must diffuse into or out of the film. These combined effects can be combined into a single charge transfer diffusion coefficient, D_{CT} . When D_{CT} is large, the cyclic voltammogram appears quite like that shown in Figure 1.1. As diffusional effects become more prominent, symmetry of the surface waves is lost as diffusional tails appear and peak potentials start to separate, and deviations from the i_p vs. v proportionality are observed. In extreme situations in which D_{CT} becomes very small, diffusional tails and peak separations become pronounced, and the voltammogram appears similar to that of the dissolved redox species in solution. In fact, i_p becomes proportional to $v^{1/2}$ and is given by the same equation employed in solution linear sweep voltammetry:

$$i_p = (2.69 \times 10^5) n^{3/2} A D_{CT}^{1/2} v^{1/2} C_{ox} \quad (1-6)$$

Lithography

One way in which to maximize the potential of organic materials for device applications is to spatially define how the material is deposited onto a substrate. Several types of applications can greatly benefit from this, including organic semiconductor technology, pixelation of displays based on electroluminescent materials (organic LEDs), 'synthetic metal' wires and interconnects,³¹ optical waveguides, and, in the case of the work reported here, optical diffraction gratings. Patterning of films can be achieved in one of two general ways, either by spatially controlling the initial deposition or growth of

the film (such as electropolymerization or self-assembly onto a patterned electrode surface),^{14,16} or by manipulation of the material once a film is cast (e.g. lithography).¹⁵

Lithography has been the workhorse of the semiconductor industry since the invention of the integrated circuit in 1960.³² The process has undergone numerous changes and enhancements during this time, aimed at the miniaturization of microelectronics. The contact printing technique employed in the work to be described in the subsequent chapters is the earliest form of photolithography, and is suitable for fabrication of three-dimensional structures with feature dimensions on the order of several microns. The premise of photolithography is to employ ultraviolet radiation to transfer an image from an opaque, patterned mask to an underlying polymer film, called a resist or photoresist, which coats an underlying substrate. Subsequent chemical development of the film differentiates between the masked and irradiated regions of the resist, selectively removing the more soluble material. The process is detailed schematically in Figure 1.3. A substrate (a silicon wafer in the case of integrated circuit fabrication) coated with a photoresist film is brought into direct contact with a mask having opaque and transparent regions. Irradiation of the resist through the mask occurs only in the transparent regions, which induces a photochemical change in the exposed areas. If a positive photoresist is employed, this reaction may be a polymer cleavage, or a similar reaction which increases its solubility relative to the non-irradiated material. Development in a suitable solvent then produces a positive-tone lithographic image, in which the features imparted to the resist match the opaque features of the lithographic mask. Alternatively, if a negative resist is used in this process, irradiation leads to polymer crosslinking, or some similar photochemical reaction which reduces the

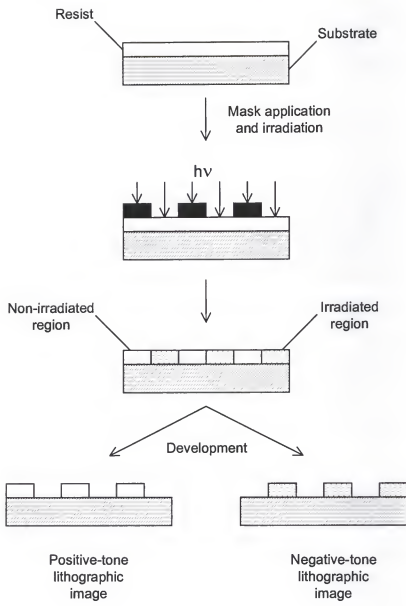


Figure 1.3. Lithographic patterning of a photoresist.

solubility of the irradiated polymer. Solvent development in this case produces a lithographic image which is a 'negative' of the pattern printed on the mask. In the production of integrated circuits and other device fabrications, subsequent treatment not shown in the figure involves either etching of the now-exposed regions of the substrate, or deposition of another material (e.g. by vapor deposition) in these areas. In either case, the final step in the process is to strip away any remaining resist material, leaving the spatially modified substrate.

There are a few drawbacks and limitations to be considered when employing a contact printing methodology. First, the hard physical contact between the lithographic mask and the photoresist can damage both the mask and the film due to surface roughness and particulate matter. In addition, adhesion of the resist to the mask can lead to damage of both upon separation. Any modification to the lithographic mask, whether by damage or adhesion of foreign material, will lead to image errors in all subsequent uses of the mask. Feature size of an imparted image is highly dependent on the wavelength of the irradiating light. As feature dimensions approach the wavelength of the light source, nonideal image transfer can occur due to edge diffraction by the mask. For this reason, the use of ultraviolet light is essential in order to minimize blurring of the features transferred to the resist. Finally, positive photoresists provide inherently higher resolution capabilities than negative resists due to swelling effects of the latter, which reduce image transfer fidelity.

Diffraction Gratings

As light passes through a material, its velocity is diminished relative to the speed of light in a vacuum. The ratio of the vacuum speed of light, c , to the velocity in a given

material, ν , is defined as the material's refractive index, n . In the discussion to follow,

$$n = c/\nu \quad (1-7)$$

we will be concerned with the complex index of refraction, $n(x, \lambda)$, which consists of a real component $n(x, \lambda)$ and an imaginary component $k(x, \lambda)$, each a function of the position along the grating, x , and the probe wavelength, λ .^{33,34} As light impinges upon

$$n(x, \lambda) = n(x, \lambda) + ik(x, \lambda) \quad (1-8)$$

a transmission grating, its speed is reduced upon passing through the grating material relative to that of the light traveling through the grating gaps. This results in beams emerging from the grating which differ *in phase* relative to each other. The spatially periodic variation of the complex refractive index in a transmission grating leads to constructive and destructive interference of these beams, producing the diffraction pattern depicted in Figure 1.4. The various orders of diffraction ($m = \pm 1, 2$ in the figure), resulting from a monochromatic beam impinging at an angle θ with respect to the z axis, appear at angles ϕ_m as defined by the grating equation:³⁵⁻³⁷

$$\phi_m = \sin^{-1}[(m\lambda/d) - \sin \theta], \quad (1-9)$$

where λ is the optical wavelength, d is the spacing between adjacent grating lines, and m is the diffracted order. In the case where $\theta = 0$, this simplifies to

$$\phi_m = \sin^{-1}(m\lambda/d). \quad (1-10)$$

The imaginary component k of the complex refractive index is related to the optical density, OD, by the equation³⁴

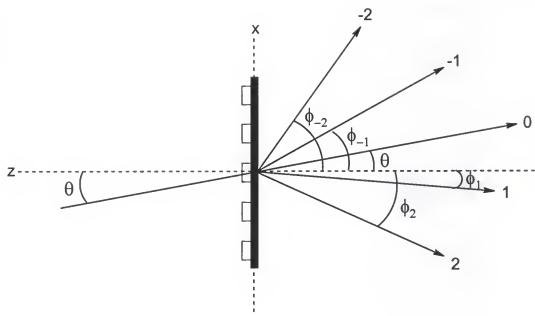


Figure 1.4. Representation of the diffraction pattern produced upon illumination of a grating-patterned photopolymer film.

$$k = \frac{2.3\lambda(\text{OD})}{4\pi T}. \quad (1-11)$$

It is clear, then, that variations in both the real (refractive index) and imaginary (absorbance) terms can affect the diffractive properties of a transmission grating. This dependence is shown in equation 1-12, the diffraction efficiency (DE, defined here as the ratio of a first-order diffracted beam intensity to that of the zero-order undiffracted beam) equation for a sinusoidal grating,^{33,34} where OD is the optical density of the grating

$$\text{DE} = \exp \left[\frac{-2.3\text{OD}}{\cos \theta} \left[\sinh^2 \frac{\pi \Delta k T}{\lambda \cos \theta} + \sin^2 \frac{\pi \Delta n T}{\lambda \cos \theta} \right] \right] \quad (1-12)$$

material, θ is the Bragg angle ($\theta = 0$ in the experiments to follow), T is the grating material thickness, λ is the probe wavelength, and Δn and Δk are, respectively, the peak-null variations of the real and imaginary complex refractive index components. Diffraction by a transmission grating can arise by periodic variation of the optical density only (i.e. $\Delta k \neq 0$, $\Delta n = 0$), in which case it is termed an amplitude grating. In this instance, the second term of equation 1-12 dominates, while the contribution of the third term is eliminated. On the other hand, a grating which possesses variations in Δn only is described by terms 1 and 3 of the equation, and is said to be a phase grating. Quite often, both Δk and Δn contribute to diffraction, so that a mixed grating is the result.

Fayer et al. have demonstrated the interrelationship of phase and amplitude contributions in laser-induced excited state gratings.^{33,34} It has been shown that at a probe frequency coincident to λ_{max} of an excited state absorption band, diffraction is governed by Δk only: under these conditions there is no phase grating contribution. As the probe frequency is moved off-resonance with the absorbance, however, the phase

grating contribution begins to play an important role. The induced variation of Δn reaches a maximum at a wavelength corresponding to the half-height of the absorbance band. As the probe frequency is moved farther off-resonance, the observed diffraction efficiency drops as both Δk and Δn diminish. The former, however, falls off more quickly than the latter, so that at wavelengths beyond the absorption band ($\Delta k = 0$), there is still a significant contribution of Δn . In these studies, Fayer et al. have demonstrated how a single grating can alternately exhibit amplitude, phase, or mixed characteristics, depending solely on the wavelength to which the probe laser is tuned.

CHAPTER 2

OPTICAL DIFFRACTION GRATINGS FABRICATED FROM A POLYPYRIDYL RUTHENIUM(II) REDOX POLYMER

Introduction

The rich and varied chemistry of polypyridyl ruthenium(II) complexes has been prevalent in the literature for many years, finding utility in areas such as photo- and electrochemistry and electrocatalysis.³⁸⁻⁴¹ These compounds exhibit several favorable characteristics, including a stable metal-to-ligand charge-transfer (MLCT) excited state which can be ‘tuned’ by appropriate ligand modification, several accessible redox states, each with its own characteristic color, and the ability to make families of related compounds for parallel studies.

Incorporation of these compounds into films on metal or semiconductor substrates can provide a means of exploiting the desired properties to a much greater degree than that possible in solution. Indeed, there have been numerous studies reported in the literature involving fabrication of modified electrode surfaces which are comprised, at least in part, of ruthenium complexes of this type (Figure 2.1).^{4,12,27,28,42,43} Fabrication of electrodes in this manner is potentially important for applications such as molecule-based microelectronic device fabrication,⁴⁴ photochemical synthesis,^{45,46} electrocatalysis,⁴⁷ chemical sensing, and electrochromic devices.^{4,5} In order for the full potential of these surfaces to be realized, spatial definition of the deposition of the films

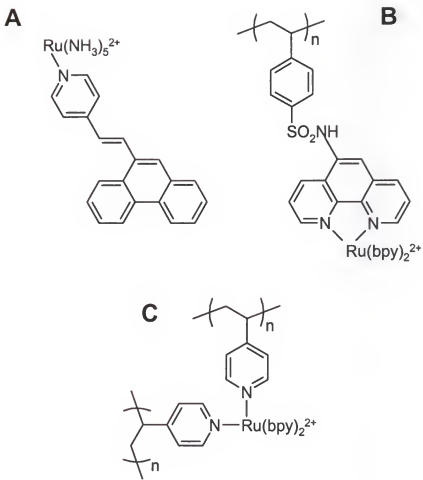


Figure 2.1. Examples of strategies for electrode surface modification with Ru(II) complexes.

A: Chemisorption of a pendant phenanthrene onto a carbon electrode (ref. 12).

B: Pendant attachment to a preformed sulfonyl chloride-substituted polymer (refs. 27, 28).

C: Electropolymerization of vinyl-substituted pyridine ligands (refs. 4, 42).

would be very beneficial. While the ability to establish structural control by buildup of multilayer films is well established, there have been comparatively few examples of spatial control of film deposition within the plane of the substrate.^{4,5,42,48,49}

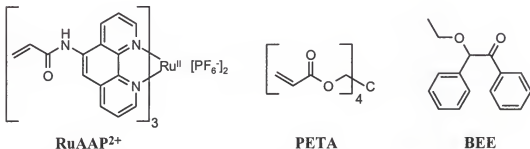


Figure 2.2. Components of spin-cast films for photolithographic patterning.

Using the complex tris(5-acrylamido-1,10-phenanthroline)ruthenium(II) hexafluorophosphate (RuAAP²⁺) as a photocrosslinkable monomer, a comparatively simple lithographic strategy to pattern redox-active films has been developed.⁴⁹⁻⁵¹ Irradiation of spin-cast films of the monomeric RuAAP²⁺ complex in the presence of a highly functionalized co-monomer (pentaerythritol tetraacrylate, PETA) and a photoinitiator (benzoin ethyl ether, BEE) through a lithographic mask leads to efficient formation of negative-tone images of the mask. Using this technique, patterned films having features on the order of several μm can be routinely fabricated with the use of a suitably patterned mask. Irradiation through a grating-patterned mask with relatively high spatial frequency (100 lines/mm) produces films which behave as optical diffraction gratings, splitting light from a laser probe into several diffractive orders. Interestingly, the diffraction efficiency of these redox-active grating-patterned films can be reversibly

modulated by an electrochemical signal. The fabrication of these films and the electrochemical and optical properties of these films will be discussed.

Results

Photopolymer Film Fabrication

Film composition. These films are largely comprised of the redox-active polypyridyl ruthenium(II) complex RuAAP²⁺. The synthetic route employed for preparation of the monomer is outlined in Figure 2.4 and described in detail in the Experimental section. RuAAP²⁺ possesses three acrylamide functional groups per monomer molecule which serve as the active sites for the light-induced polymerization and crosslinking process. The second film component, PETA, serves a twofold purpose. The four acrylate groups per monomer provide extensive crosslinking to the resulting polymer network, imparting stability and insolubility to the film. Also, the very high viscosity and low volatility of this liquid make it an ideal solvent component, facilitating the formation of homogeneous films. Films which do not contain PETA tend to give a microcrystalline surface morphology which is not conducive to the lithographic process. The final film component, BEE, is added in small proportion and serves as the photoinitiator for the

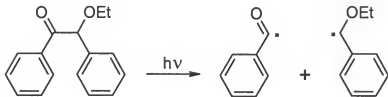


Figure 2.3. Norrish cleavage of benzoin ethyl ether to form benzoyl and benzyl ether radicals.

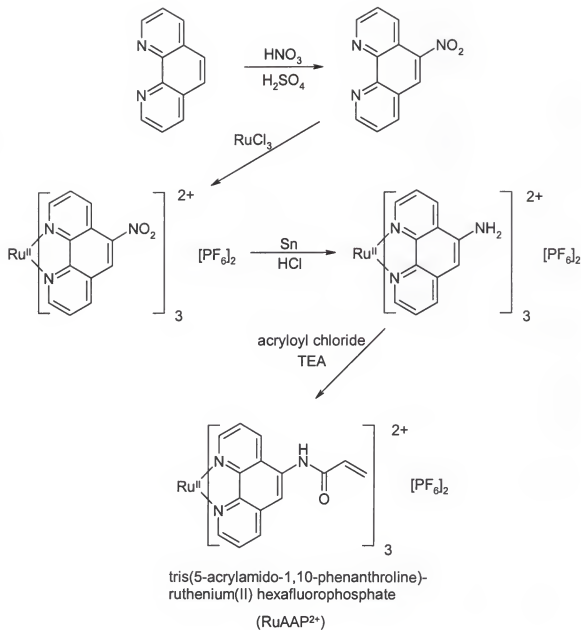


Figure 2.4. Synthetic route for preparation of RuAAP²⁺.

free-radical polymerization process. Upon irradiation, BEE undergoes a Norrish Type I cleavage to form a benzoyl and a benzyl ether radical (Figure 2.3),⁵² both of which are capable of initiating the polymerization of acrylate monomers.⁵³

Lithographic technique. The general lithographic process employed for fabrication of these patterned films is outlined in Figure 2.5. The substrate used for film deposition is an indium-tin oxide- (ITO) coated glass optically transparent electrode (OTE). In order to prepare thin polymer films having uniform thickness and distribution, a spin-coating technique is employed. A concentrated solution of RuAAP²⁺, PETA, and BEE is spin-cast onto the substrate and is allowed to dry briefly in ambient air. It is then placed in direct contact with a chrome-on-glass lithographic mask and irradiated face-on through the mask in a manner analogous to the contact printing technique described in Chapter 1. In the film areas not covered by the mask, light-induced Norrish cleavage of benzoin ethyl ether initiates the radical copolymerization of RuAAP²⁺ and PETA. In these regions, the film becomes highly crosslinked due to the multifunctional nature of both PETA and the ruthenium complex itself, imparting insolubility to the film. In the regions of the film where irradiation is blocked by the mask, photoinitiation by BEE does not occur and the film remains unpolymerized and soluble in suitable organic solvents. The final film development step consists of sequential immersion in a series of solvents which selectively dissolve and rinse away the unpolymerized regions of the film, producing a negative-tone lithographic image of the mask.

Table 2.1 lists the quantities of the three chemical components used during film preparation. The most convenient way to prepare the monomer/initiator solutions used for spin-coating is to directly weigh out the solid RuAAP²⁺ monomer and dissolve it in

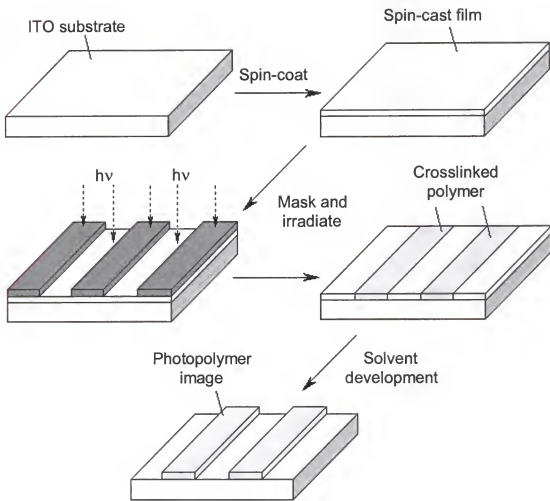


Figure 2.5. Lithographic procedure for fabrication of patterned photopolymer films.

Table 2.1. Composition data for PETA and BEE stock solutions and monomer/initiator solutions used for spin-coating.

Component	Stock Solutions ^a			Spin-Coating Mixture ^a		
	mg/µL	µmol/µL	µL used	mg added	µmol added	Concentration, M (in 15 µL)
RuAAP ²⁺	-	-	-	6	5.3	0.35
PETA	0.33	0.94	9	3	8.51	0.57
BEE	0.021	0.092	6	0.126	0.55	0.037

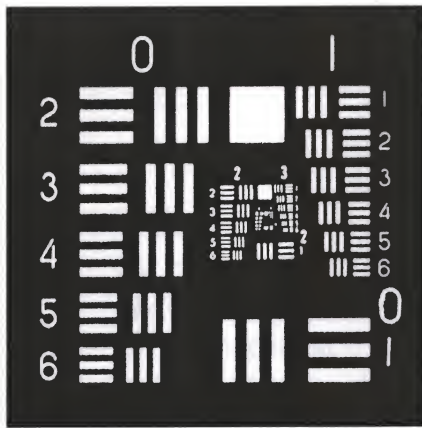
a DMF solvent.

stock solutions of PETA and BEE, due to the high viscosity of PETA and the typically small quantities used of these two components. The stock solution of PETA is prepared by diluting 1 g of the viscous liquid with dimethylformamide to a volume of 3 mL. The photoinitiator stock solution is prepared by dissolving 0.021 g of benzoin ethyl ether in 1 mL of dimethylformamide. Typical spin-coating solutions are prepared by dissolving 6 mg of RuAAP²⁺ in 9 µL of PETA stock and 6 µL of BEE stock, or in multiples thereof, maintaining a 2:1 mass ratio of RuAAP^{2+:}PETA and 10% (mol/mol w.r.t. RuAAP²⁺) BEE concentration. The resulting concentrations of RuAAP²⁺, PETA, and BEE in a solution prepared in this manner are 0.35, 0.57, and 0.037 M, respectively. Onto the ITO substrate is placed 3–4 µL of the monomer/initiator solution, delivered by capillary or autopipet, and the solution is manually spread over the substrate surface using a glass rod. The ITO substrate is placed in the spin-coater and spun at 4000–6000 rpm for 15 s to remove excess solution and give a uniform film thickness. After a brief air-drying period, the spin-cast film is irradiated face-on through the mask with a Pyrex-filtered medium-pressure mercury lamp (intensity \approx 60 mW·cm⁻²) at a distance of ca. 1 in. for 45–

60 minutes. Following exposure, the coated substrate is removed from the mask and developed by sequential immersion and gentle agitation in absolute ethanol, methylene chloride, and 1:1 absolute ethanol:methylene chloride (15-20 s in each), and dried under a gentle stream of nitrogen. If the feature resolution of the patterned film is unsatisfactory (presence of background film in unirradiated areas, as determined by optical microscopy), it can often be improved by prolonged (1-2 min.) immersion in the developing solvents.

The quality of these photopolymer films depends in large part upon the duration of the film irradiation process. The best results are obtained by exposure for 45-60 minutes, producing a well-resolved photopolymer image that is stable to prolonged immersion in organic solvents. Shorter irradiation times may produce images with better feature resolution, but these films appear to be, by optical microscopic inspection, significantly thinner and less stable to the development process. In most cases, the features produced by short irradiation times (less than 30 minutes) are partially or completely lifted off the substrate surface by the developing solvents.

Optical transmission and scanning electron microscope images of *poly*-RuAAP²⁺/PETA films fabricated by the above procedure are shown in Figures 2.7 and 2.8. The patterned films shown in Figure 2.7 were produced by irradiation through a USAF 1957 test pattern reticle depicted in Figure 2.6. The linewidths of the features of the repeating pattern follow an algorithm based upon the group number located at the top of the pattern and the element number located to the side of each group of vertical and horizontal lines. The table in Figure 2.6 lists the feature linewidths, organized by group number and



Element #	Group #			
	4	5	6	7
1	31.3	15.6	7.8	3.9
2	27.9	13.9	7.0	3.5
3	24.8	12.4	6.2	3.1
4	22.1	11.0	5.5	2.8
5	19.7	9.8	4.9	2.5
6	17.5	8.8	4.4	2.2

Figure 2.6. USAF 1957 test pattern used for lithographic patterning. Top: representation of the repeating pattern used for fabrication of the *poly*-RuAAP²⁺/PETA films shown in Figure 2.5. Group numbers are designated at the top of each pattern and element numbers are situated to the side of the horizontal and vertical features. Bottom: table indicating the feature linewidths in μm of the groups shown in Figure 2.5.

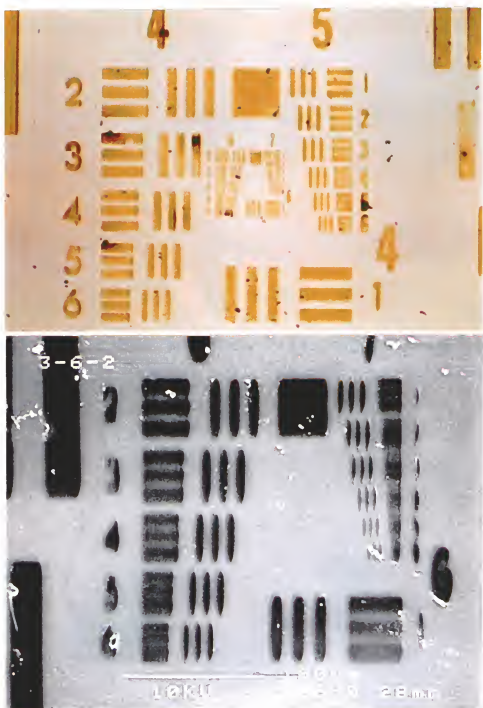


Figure 2.7. Optical transmission and scanning electron microscope images of *poly-RuAAP²⁺/PETA* films fabricated using the USAF 1957 lithographic mask. Top: optical microscope image showing groups 4-7 of the test pattern. The yellow-orange features are the photopolymer film against the lighter background of the borosilicate glass substrate. Bottom: SEM image of groups 6 and 7, showing the photopolymer film as dark regions against the bare glass substrate.

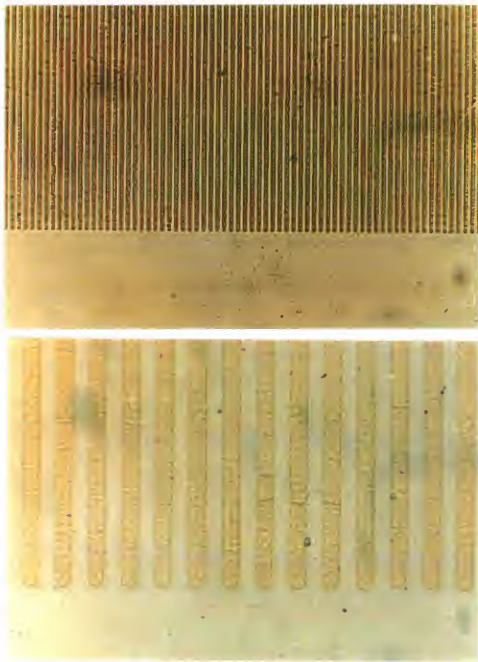


Figure 2.8. Optical transmission microscope images of a grating-patterned *poly-RuAAP²⁺/PETA* film. Top: 200x magnification. Bottom: 1000x magnification. The photopolymer lines are the darker regions against the lighter shade of the bare borosilicate glass substrate.

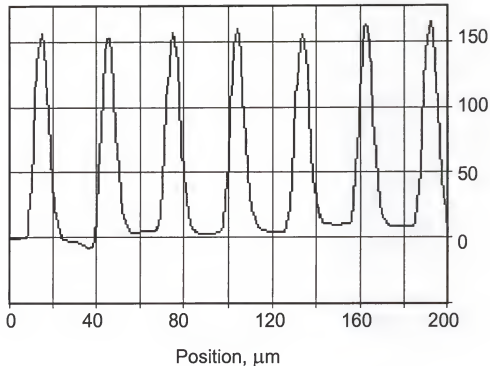


Figure 2.9. Profilometry data from a grating-patterned *poly*-RuAAP²⁺/PETA film on an ITO substrate. A photopolymer film having linewidths of 5 μm separated by 25 μm gaps was scanned using a 12 μm profilometer stylus tip. The scale on the bottom axis gives the horizontal position across the patterned film, and the scale on the right axis shows the measured thickness in nm.

element number within the group. Comparison of these values with the images shown in Figure 2.7 reveals that film features as small as 2.2 μm (group 7, element 6) can be attained by this method, although reproducibility at this resolution is limited. The observed blending of the horizontally oriented pattern elements is due to a large vertical angular distribution of impinging light from the mercury lamp. The vertically oriented film elements are well resolved since the lamp is dimensionally much narrower, so the lateral angular distribution is also quite narrow. Vertical resolution can be enhanced by confining the impinging light to that which is approximately perpendicular to the substrate surface (see examples in Chapters 3 and 4). Film features having linewidths of 5 μm (group 6, element 5) can be produced quite reliably and thus this is the scale chosen for fabrication of grating-patterned films. The film shown in the microscope images of Figure 2.8 was fabricated by irradiation through a grating-patterned reticle having equal line- and gapwidths of 5 μm (100 lines/mm). Film fabrication at this resolution reliably produces images that very closely match the features of the lithographic mask. Profilometry data of grating-patterned films (Figure 2.9) indicates that films 150 nm thick can be routinely produced.

Electrochemistry and Spectroelectrochemistry

As expected, the ruthenium complex RuAAP²⁺ largely maintains its electrochemical properties when incorporated into the polymeric matrix. The cyclic voltammetric response of the monomer in solution (Figure 2.10) shows the expected Ru^{2+/3+} redox couple with anodic and cathodic waves at 1.44 and 1.34 V, respectively. These potentials are measured vs. a Ag wire quasi-reference electrode, which is used due

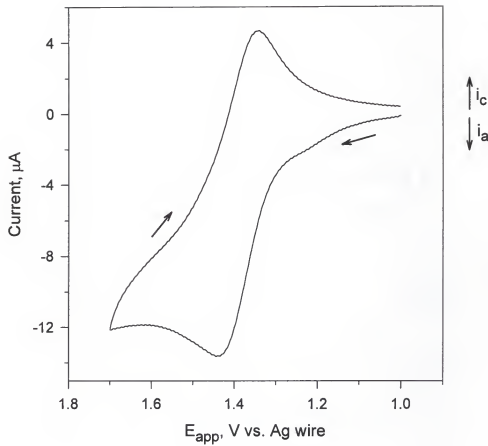


Figure 2.10. Cyclic voltammetry of RuAAP²⁺ monomer in solution. Conditions: ITO working electrode (0.0792 cm² active area), 0.1 M (n-Bu₄N)PF₆/acetonitrile electrolyte solution, Ag wire quasi-reference electrode, 100 mV·s⁻¹ scan rate.

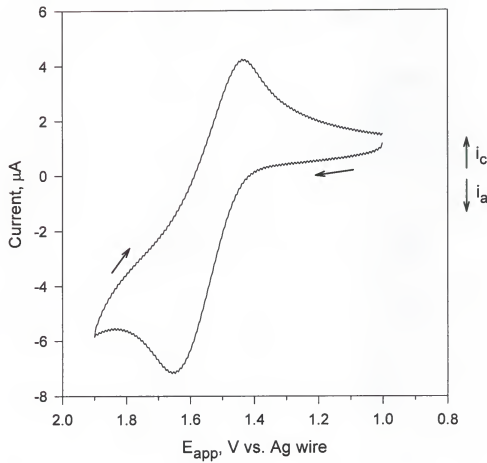


Figure 2.11. Cyclic voltammetry of a grating-patterned $\text{poly-RuAAP}^{2+}/\text{PETA}$ photopolymer film. Conditions: ITO working electrode substrate (0.0792 cm^2 active electrode area, 0.0396 cm^2 film area), 0.1 M ($n\text{-Bu}_4\text{N}\text{PF}_6$) CH_2Cl_2 electrolyte solution, Ag wire quasi-reference electrode, $100 \text{ mV}\cdot\text{s}^{-1}$ scan rate.

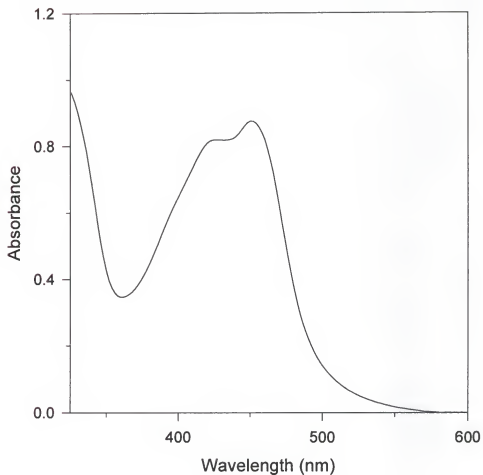


Figure 2.12. Visible MLCT absorption band of RuAAP²⁺ monomer in solution. 0.05 mM solution in acetonitrile, 1 cm cell pathlength.

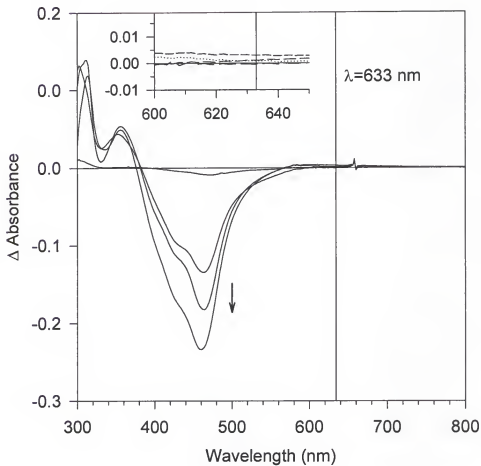


Figure 2.13. Spectroelectrochemical data from a *poly*-RuAAP²⁺/PETA grating-patterned film. Spectra were measured at 0.0, 1.0, 1.25, 1.55, and 1.7 V applied potential, allowing 30 s for equilibration prior to absorbance measurement. Delta absorbance was calculated by subtraction of the film absorbance at 0.0 V. The vertical line indicates the wavelength of the He-Ne laser probe (632.8 nm) used for diffraction studies. Inset: expansion of the region around the wavelength of the He-Ne laser probe (vertical line).

to size constraints in the electrochemical cell. Cyclic voltammetry of a *poly*-RuAAP²⁺/PETA photopolymer film (Figure 2.11) exhibits an anodic wave at 1.66 V and a cathodic wave at 1.44 V on the reductive return scan, demonstrating at least partial reversibility of the redox process

The UV-visible absorption characteristics of the ruthenium complex are also maintained upon inclusion in the polymer matrix. Solution-phase absorbance data of the RuAAP²⁺ monomer is shown in Figure 2.12. The MLCT absorption band at $\lambda_{\text{max}} = 452$ nm is characteristic of polypyridyl Ru(II) complexes of this type.⁵⁴ This behavior is preserved upon incorporation in the polymer film, as shown in Figure 2.13. The Figure depicts the spectroelectrochemical response of a grating-patterned *poly*-RuAAP^{2+/3+}/PETA film as the applied electrode potential is stepped in sequence from 0.0 V to 0.0, 1.25, 1.55, and 1.70 V, corresponding to progression through the RuAAP^{2+/3+} redox couple. The delta absorbance values shown in the figure were calculated by subtraction of the film absorbance at 0.0 V. The decrease in absorbance is due to bleaching of the *poly*-RuAAP²⁺ MLCT absorption band upon electrochemical oxidation of the film.

Quantification of Electrode Surface Coverage

Absorbance-based calculation. From solution absorption studies, the molar absorptivity, ϵ , of RuAAP²⁺ can be calculated by the Beer-Lambert equation (2-1), where A is the observed absorbance, and b and C are the cell pathlength and the concentration

$$A = \epsilon b C \quad (2-1)$$

of the absorbing species, respectively. A plot of absorbance at $\lambda_{\text{max}} = 452$ vs. concentration (Figure 2.14) is linear with a slope of $1.79 \times 10^4 \text{ L} \cdot \text{mol}^{-1}$. For a cell of

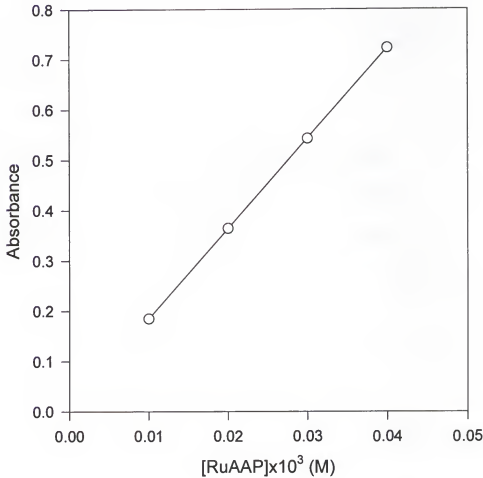


Figure 2.14. Plot of RuAAP²⁺ monomer MLCT absorbance vs. concentration. Absorbances at $\lambda_{\text{max}} = 452$ nm were recorded at RuAAP concentrations of 0.01, 0.02, 0.03, and 0.04 mM in acetonitrile in a 1 cm quartz cell. Linear regression ($r^2 = 0.99999$) provides a slope of 1.79×10^4 L·mol⁻¹, corresponding to a molar absorptivity of 1.79×10^4 L·mol⁻¹·cm⁻¹.

pathlength = 1 cm, this results in a calculated ϵ value of $1.79 \times 10^4 \text{ L}\cdot\text{mol}^{-1}\cdot\text{cm}^{-1}$ ($1.79 \times 10^7 \text{ cm}^2\cdot\text{mol}^{-1}$). Assuming that this value does not change significantly for the chromophore upon inclusion into the polymer matrix, ϵ can be applied to calculations involving *poly*-RuAAP²⁺/PETA films. While in this case the exact values of b and C are not known, they can conveniently be combined into one term, Γ_A (2-2). If the concentration is expressed in

$$\Gamma_A(\text{mol}\cdot\text{cm}^{-2}) = b(\text{cm})\cdot C(\text{mol}\cdot\text{cm}^{-3}) \quad (2-2)$$

$\text{mol}\cdot\text{cm}^{-3}$ and the pathlength is expressed in cm, Γ_A will have units of $\text{mol}\cdot\text{cm}^{-2}$. This parameter quantifies the surface coverage of absorbing sites in a given surface area, and is a useful measurement for characterization of chemically modified electrodes. Considering that the film absorbance was measured using a grating-patterned film in which only half of the electrode surface is covered by the polymer film, equation 2-1 becomes

$$2A = \epsilon\Gamma_A \quad (2-3)$$

(ϵ expressed in $\text{cm}^2\cdot\text{mol}^{-1}$). Rearrangement to solve for surface coverage gives

$$\Gamma_A = \frac{2A}{\epsilon}. \quad (2-4)$$

To apply these calculations, absorbance data (Table 2.2, column 3) was collected from three identically fabricated *poly*-RuAAP²⁺/PETA grating-patterned films to give an average absorbance of 0.282 at $\lambda_{\text{max}} = 458 \text{ nm}$. Inserting this value into equation 2-4 results in a calculated average RuAAP²⁺ surface coverage (Table 2.2, column 5) of $\Gamma_A = 3.15 \times 10^{-8} \text{ mol}\cdot\text{cm}^{-2}$. Also collected in Table 2.2 is spectroelectrochemical absorbance

data from the same substrates. In column 4 is listed the decrease in absorption at λ_{\max} upon electrochemical oxidation at an applied potential of 1.70 V (vs. Ag wire), and the resulting calculated surface coverage values, $\Gamma_{\Delta A}$, are listed in column 6.

Table 2.2. Poly-RuAAP²⁺ absorbance data.

Electrode #	λ_{\max} (nm)	Absorbance	Δ Absorbance ^a	Γ_A^b (mol·cm ⁻²)	$\Gamma_{\Delta A}^c$ (mol·cm ⁻²)
1	456	0.325	0.234	3.63×10^{-8}	2.61×10^{-8}
2	458	0.264	0.184	2.95×10^{-8}	2.06×10^{-8}
3	458	0.258	0.166	2.88×10^{-8}	1.85×10^{-8}
ave =		0.282	0.195	3.15×10^{-8}	2.17×10^{-8}

a Absorbance bleaching at λ_{\max} upon film oxidation at +1.7 V.

b Calculated surface coverage using absorbance values from column 3.

c Calculated electroactive surface coverage using delta absorbance values from column 4.

Electrochemically-derived calculation. A complementary calculation of the electrode surface coverage can be done using cyclic voltammetry data. The applied potential in volts can be converted to time in seconds by dividing by the scan rate, in this case $0.01 \text{ V}\cdot\text{s}^{-1}$. The charge passed by oxidation of the film, Q_f (coulombs, C), is calculated by integration of the current over time (eq. 2-5), which is in turn converted to moles by dividing by the Faraday constant (eq. 2-6, $F = 9.648 \times 10^4 \text{ C}\cdot\text{mol}^{-1}$). The ratio of this value over the redox-active film area, A_f (cm², film area = $0.5 \times$ electrode area for

a grating-patterned film), gives the electrochemically calculated surface coverage, Γ_E , in mol·cm⁻² (eq. 2-7).

$$Q_f = \int i \, dt \quad (2-5)$$

$$n = \frac{Q_f}{F} \quad (2-6)$$

$$\Gamma_E = \frac{n}{A_f} \quad (2-7)$$

Combination of equations 2-5, 2-6, and 2-7 gives the final expression

$$\Gamma_E = \frac{Q_f}{F A_f}. \quad (2-8)$$

Collected in Table 2.3 is cyclic voltammetric data from several identically-prepared *poly*-RuAAP²⁺/PETA grating-patterned films and the resulting surface coverage values.

Composition-based calculation. A third method of calculating the surface coverage of RuAAP²⁺ is based upon consideration of the initial composition of the spin-cast film prior to irradiation. For a given volume of photopolymer film, V_f , its mass can be calculated if the film density, d_f , is known or approximated (2-9). Assuming that the

$$\text{mass}_{\text{film}} = V_f \cdot d_f \quad (2-9)$$

$$\text{mass}_{\text{Ru}} = 0.67 \cdot \text{mass}_{\text{film}} \quad (2-10)$$

$$n_{\text{Ru}} = \frac{\text{mass}_{\text{Ru}}}{\text{MW}_{\text{Ru}}} \quad (2-11)$$

$$\Gamma_C = \frac{n_{\text{Ru}}}{A_f} \quad (2-12)$$

film composition does not change significantly upon polymerization, the mass percentage of RuAAP²⁺ in the film is known based upon the initial composition of the spin-coating

Table 2.3. *Poly-RuAAP²⁺* electrochemical and surface coverage data.

Electrode (Region) ^a	q_a ^b (μ C)	q_c ^c (μ C)	q_{ave} ^d (μ C)	Γ_E ^e $\text{mol}\cdot\text{cm}^{-2}$
1(A)	22.7	18.3	20.5	5.37×10^{-9}
1(B)	24.9	21.5	23.2	6.07×10^{-9}
1(C)	18.7	16.2	17.5	4.58×10^{-9}
2(A)	27.7	21.1	24.4	6.39×10^{-9}
2(B)	25.2	19.3	22.3	5.84×10^{-9}
3(A)	39.0	35.1	37.1	9.71×10^{-9}
3(B)	36.1	33.9	35.0	9.16×10^{-9}
3(C)	37.4	35.9	36.7	9.61×10^{-9}

Conditions: grating-patterned *Poly-RuAAP²⁺*/PETA film, 0.1 M (n-Bu₄N)PF₆/CH₂Cl₂ electrolyte, 0.7 to 1.8 V vs. Ag wire, 100 mV·s⁻¹ scan rate.

a Three individual patterned electrodes were used in various film regions.

b Integration of anodic current wave.

c Integration of cathodic current wave.

d Average value of q_a and q_c to correct for baseline estimation error, equivalent to the charge passed in anodic wave, assuming electrochemical reversibility. This is the value

used for the calculation in Equation 2-8.

e Active electrode surface area exposed to electrolyte solution = 0.0792 cm² (1/8 in circular aperture), $A_f = 0.0396$ cm².

mixture. In the present case, RuAAP²⁺ comprises 67% of the total mass, neglecting the comparatively smaller mass contribution of BEE (2-10). From this value the number of moles of RuAAP²⁺, n_{Ru} , is calculated by division by its molecular weight (2-11). Division by the surface area of the film, A_f , results in the composition-based RuAAP²⁺ surface coverage, Γ_C (2-12). To apply the calculations, a single stripe of *poly*-RuAAP²⁺/PETA film can be considered, having a width of 5 μm (5×10^{-4} cm), a length of 2 mm (0.2 cm), and an assumed rectangular cross-section. From profilometry data, the thickness is known to be 150 nm (1.5×10^{-7} cm), resulting in a film volume of 1.5×10^{-9} cm^3 . Inserting an assumed film density of 1.0 $\text{g}\cdot\text{cm}^{-3}$, a RuAAP²⁺ molecular weight of 1138.81 $\text{g}\cdot\text{mol}^{-1}$, and a surface area of 1×10^{-4} cm^2 into equations 2-9 to 2-12, a Γ_C value of 8.83×10^{-9} $\text{mol}\cdot\text{cm}^{-2}$ is calculated.

Table 2.4 summarizes the collective results of the surface coverage calculations based upon film absorbance intensity of the RuAAP²⁺ MLCT band, the spectroelectrochemical bleaching of the MLCT band upon electrochemical film oxidation, integration of the cyclic voltammetric current waves, and the known initial composition of the unexposed monomeric spin-cast films.

Table 2.4. Summary of *poly*-RuAAP²⁺ surface coverage calculations.

Calculation Method	Γ ($\text{mol}\cdot\text{cm}^{-2}$)
MLCT Absorbance	2.82×10^{-8}
MLCT Bleaching	1.95×10^{-8}
Electrochemical	7.09×10^{-9}
Composition	8.83×10^{-9}

Diffraction Experiments

Grating-patterned *poly*-RuAAP²⁺/PETA films behave as optical diffraction gratings and diffract light. Illumination of the film with a He-Ne laser probe produces a diffraction pattern in which diffracted beams of several orders can be seen, as illustrated by Figure 2.15. Interestingly, it has been found that the diffraction efficiency of these films can be reversibly modulated by an electrochemical signal. To investigate this behavior, the experimental setup and conditions described in the Appendix was used.

Shown in Figure 2.16 is a typical diffraction efficiency modulation experiment. Four applied potential cycles between 0.0 and 1.8 V at a scan rate of 10 mV s⁻¹ are shown, corresponding to the *poly*-RuAAP²⁺ and *poly*-RuAAP³⁺ redox states, respectively (section a). At the onset of film oxidation at approximately 1.2 V, as indicated by the flow of anodic current (section b, dashed line), the intensity of a first-order diffracted beam (section b, solid line) begins to fall, which is interpreted as a decrease in diffraction efficiency. The diffracted beam intensity continues to decrease, to approximately 77 percent of the initial level, until the potential scan is reversed and the film is subsequently re-reduced, as indicated by cathodic current flow. At this point, the diffracted beam intensity rises, and eventually recovers to approximately 93 percent of its initial level at the end of the triangular potential sweep. This behavior is observed in the three subsequent potential scans, with the diffracted beam intensity falling to 75-77 percent upon film oxidation, and rising to approximately 93 percent, the level established by the first cycle, upon return to a reductive electrode potential. After the fourth potential scan, however, irreproducibility of the diffraction efficiency modulation is observed. Table 2.5

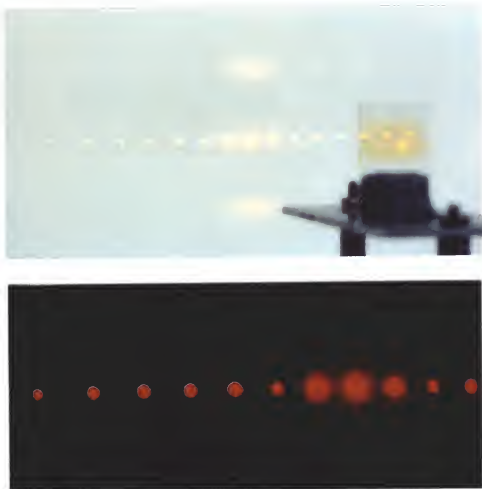


Figure 2.15. Diffraction of light by a grating-patterned $\text{poly-RuAAP}^{2+}/\text{PETA}$ film. Top: light from a helium-neon laser impinging upon the vertically-oriented polymer grating (right foreground) is split into seven visible orders of diffraction to either side of the central undiffracted beam. Bottom: seven orders of diffraction to the left and three to the right of the zero-order beam.

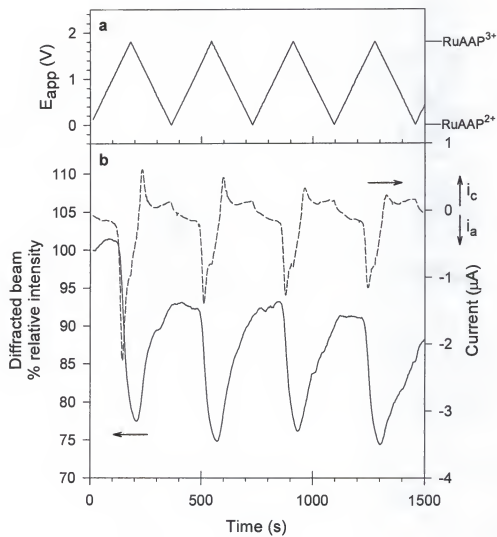


Figure 2.16. Electrochemical modulation of the diffraction efficiency of a poly- RuAAP^{2+} /PETA grating-patterned film. Conditions: ITO working electrode substrate (0.0792 cm^2 active electrode area, 0.0396 cm^2 film area), 0.1 M (n-Bu₄N)PF₆/CH₂Cl₂ electrolyte solution, Ag wire quasi-reference electrode. (a) Applied potential scanned through the Ru(2+/3+) redox couple at 10 mV/s ; (b) dashed line: current response, scale on right axis; solid line: relative intensity of first order diffracted beam, scale on left axis.

lists the results of four diffraction experiments through eight consecutive potential scans (the data depicted in Figure 2.16 corresponds to potential scans 1-4 of Experiment 1 in the table). After the fourth cycle, the relative diffracted beam intensity modulation (column 5) deteriorates with each subsequent potential scan. The drop in the diffracted beam intensity upon oxidation of the film is diminished, as is the level to which the intensity recovers upon re-reduction. This irreproducibility over successive potential scans is observed in Experiments 2 through 4 of Table 2.5 as well, and is especially evident in Experiment 2, in which the diffracted beam intensity modulation decreases from 27% during the first cycle to 4% over the course of the next eight scans.

Refractive Index Determination.

As described in Chapter 1, the diffraction efficiency of a phase grating is dependent upon the difference of refractive index between the grating material and the surrounding medium, which in this case is a bathing liquid. When this variation is large, the diffraction efficiency is high, and when the refractive indices are equal, no diffraction is observed. Systematic variation of the refractive index of the bathing liquid and measurement of the intensity of a diffracted beam can then determine the refractive index of the grating material.⁵⁵ A plot of diffracted beam intensity vs. refractive index should be parabolic, with the minimum corresponding to the refractive index of the grating. To carry out the experiment, a grating-patterned film was mounted in the electrochemical cell used for the diffraction experiments and the cell was filled with a series of solvents of known refractive index. The film was illuminated with a He-Ne laser, and the intensity of one first-order diffracted beam was measured using a photodiode. Table 2.6 lists the solvents used, their refractive indices, and the resulting diffracted beam intensity. Shown

Table 2.5. Continuous-sweep electrochemical diffraction efficiency modulation data for four *poly*-RuAAP²⁺/PETA grating-patterned films.

Experiment #	Potential Scan ^a	Intensity	Intensity	Intensity
		Maximum (%) ^b	Minimum (%) ^c	Modulation (%) ^d
1	1	100	77	23
	2	93	75	18
	3	93	77	16
	4	92	75	17
	5	89	73	16
	6	88	74	14
	7	88	76	12
	8	88	78	10
2	1	100	73	27
	2	92	72	20
	3	90	72	18
	4	88	70	18
	5	84	68	16
	6	82	72	10
	7	80	78	2
	8	80	76	4
3	1	100	75	25
	2	91	74	17
	3	90	73	17
	4	89	73	16
	5	87	74	13
	6	87	73	14
	7	85	73	12
	8	84	74	10
4	1	100	73	27
	2	93	75	18
	3	90	69	21
	4	82	67	15
	5	83	69	14
	6	84	71	13
	7	86	72	14
	8	85	73	12

Conditions: ITO working electrode substrate (0.0792 cm² active electrode area, 0.0396 cm² film area), 0.1 M (n-Bu₄N)PF₆/CH₂Cl₂ electrolyte solution.

a Electrode potential scanned between 0.0 and 1.8 V vs. Ag wire at 10 mV·s⁻¹.

b Maximum relative diffracted beam intensity at the onset of each potential scan cycle. The intensity prior to the first scan of each experiment is established as 100%.

c Minimum relative diffracted beam intensity attained during each potential scan cycle.

d Percent relative intensity change of the diffracted beam during each potential scan cycle (% max - % min).

in Figure 2.17 is a plot of the data obtained, which indicates a *poly*-RuAAP²⁺/PETA film refractive index of ~1.61.

Table 2.6. Data for determination of *poly*-RuAAP²⁺/PETA film refractive index.

Solvent	Refractive index	Photodiode output (mV)
Methanol	1.326	1220
Heptane	1.385	719
Carbon tetrachloride	1.459	350
Benzene	1.498	209
Chlorobenzene	1.523	120
Ethylene bromide	1.538	83
o-Dichlorobenzene	1.551	53
Bromoform	1.587	0.4
Methylene iodide	1.749	329

Discussion

Film Characterization

Electrochemistry. As described in Chapter 1, the thin-layer electrochemical model predicts that surface-confined redox species should exhibit several electrochemical properties which differ from those of analogous solution-phase studies. The 'ideal' film will exhibit no anodic-cathodic current peak separation ($\Delta E_p = 0$), narrow oxidative and reductive waves (90.6/n mV full width at half-maximum) which are symmetrical both about the peak potential and with each other, and proportionality of peak currents to the applied potential scan rate. As can be seen by comparison of Figures 2.10 and 2.11, the

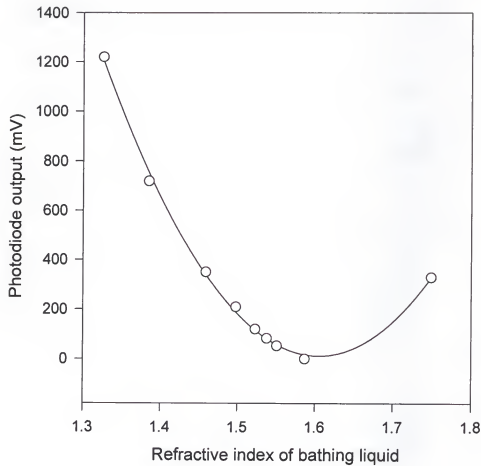


Figure 2.17. Plot of photodiode output vs. bathing liquid refractive index. Intensities of a first-order diffracted beam were measured for a grating-patterned *poly*-RuAAP²⁺/PETA film in contact with the solvents of known refractive indices listed in Table 2.6 (circles). The solid line is the result of a second order fit of the data ($r^2 = 0.998$). The curve minimum at ca. 1.61 corresponds to the refractive index of the polymer film.

electrochemical response of a *poly*-RuAAP²⁺/PETA film more closely resembles the solution electrochemistry of the monomer than it does the ideal described here.

Because the current does not return to zero between the oxidative and reductive potential scans, is it difficult to determine the true peak currents atop a sloping baseline in order to test the linearity of the peak currents with the potential scan rate. It has been suggested²⁹ that if the actual baseline cannot be established, the actual cathodic peak current i_{pc} can be determined from the baseline-uncorrected cathodic peak current (i_{pc})₀ relative to the zero current baseline and the current at the switching potential (i_{sp})₀ by the expression:

$$\frac{i_{pc}}{i_{pa}} = \frac{(i_{pc})_0}{i_{pa}} + \frac{0.485(i_{sp})_0}{i_{pa}} + 0.086 \quad (2-13)$$

For a Nernstian wave, the ratio i_{pc}/i_{pa} should equal 1, regardless of the scan rate, the switching potential E_λ (provided $E_\lambda > 35/n$ mV past the peak potential), or diffusion coefficients.

Shown in Figure 2.18 and collected in Table 2.7 are the data obtained from cyclic voltammetric experiments conducted on the same *poly*-RuAAP²⁺/PETA grating-patterned film at several scan rates and the calculated i_{pc}/i_{pa} values, from which the cathodic peak currents are determined. Shown in Figure 2.19 is a plot of the anodic and cathodic peak currents vs. the potential scan rate, which clearly demonstrates that the predicted linear relationship for surface-confined species is not observed, but is approached only at the slowest scan rates. When the peak currents are plotted vs. the square root of the scan rate (Figure 2.20), however, a linear relationship is evident. This

linearity with $v^{1/2}$ again indicates that the electrochemical properties of these films are more typical of solution-phase behavior, in which the kinetics is limited by a diffusion process.

Further evidence of a kinetic hindrance are the nonzero peak separations, which increase at higher scan rates, also shown in Table 2.7. The source of the kinetic limitation may be surmised by consideration of the processes occurring within the film during the redox process. There may be slow electron transfer between the surface-confined species and the electrode surface, or a slow rate of charge transport between redox sites within the film itself. Alternatively, the rate may be limited by restricted flow of counterions and accompanying solvent molecules between the film and the bathing electrolyte solution, which is required to maintain charge neutrality within the film, or by restricted solvation or structural reorganization which may result from a change in oxidation state.

A likely cause of any or all of the above possible kinetic limitations may be the high composition of PETA within the film. The insulating nature of PETA may inhibit the electron transfer interaction between the redox sites within the polymer and the electrode surface. Also, assuming that there is random copolymerization of PETA and RuAAP²⁺ upon exposure, with no domains enriched in either component, intervening PETA molecules will increase the separation between the RuAAP²⁺ sites, hindering the redox-conductivity through the film. Further, due to the potential for a very high degree of crosslinking within the film due to the multifunctionality of both film components, film permeability and mobility may be quite restricted, which would limit counterion flux and restrain structural rearrangements during the redox processes.

Table 2.7. Scan rate-dependent electrochemical data for a *poly*-RuAAP²⁺/PETA grating-patterned film.

ν^a (mV·s ⁻¹)	E_s^b (V)	i_{pa}^c (μ A)	$(i_{pc})_0^d$ (μ A)	$(i_{sp})_0^e$ (μ A)	$(i_{pc}/i_{pa})_{calc}^f$	$(i_{pc})_{calc}^g$ (μ A)	ΔE_p^h (V)
5	1.80	1.22	0.57	1.46	1.13	1.38	0.16
10	1.80	1.87	1.01	1.85	1.10	2.07	0.16
20	1.90	2.81	1.61	3.10	1.19	3.35	0.16
50	1.90	4.94	2.89	4.42	1.10	5.45	0.20
100	1.90	7.11	4.22	5.85	1.08	7.66	0.23

a Electrode potential scan rate.

b Switching potential.

c Anodic peak current.

d Baseline-uncorrected cathodic peak current.

e Measured current at the switching potential.

f Cathodic:anodic current ratio calculated by Equation 2-13.

g Baseline-corrected calculated cathodic peak current.

h Anodic-cathodic peak current separation.

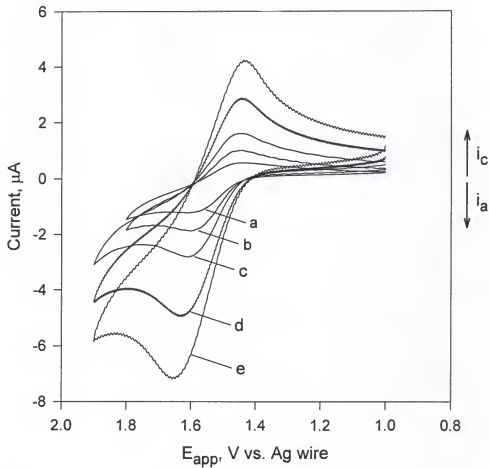


Figure 2.18. Cyclic voltammetry of a grating-patterned $\text{poly-RuAAP}^{2+}/\text{PETA}$ photopolymer film at several applied potential scan rates. Conditions: ITO working electrode substrate (0.0792 cm^2 active area), 0.1 M ($n\text{-Bu}_4\text{N}$) $\text{PF}_6^-/\text{CH}_2\text{Cl}_2$ electrolyte solution, Ag wire quasi-reference electrode, scan rate: (a) $5 \text{ mV}\cdot\text{s}^{-1}$ (b) $10 \text{ mV}\cdot\text{s}^{-1}$ (c) $20 \text{ mV}\cdot\text{s}^{-1}$ (d) $50 \text{ mV}\cdot\text{s}^{-1}$ (e) $100 \text{ mV}\cdot\text{s}^{-1}$.

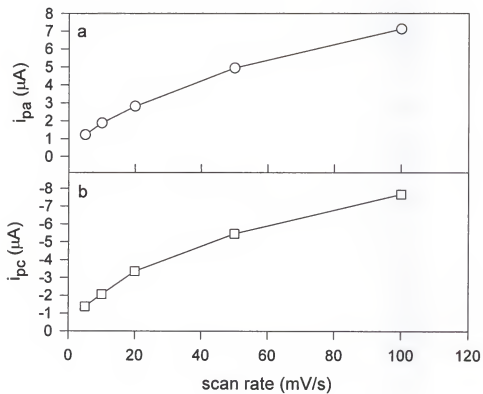


Figure 2.19. Nonlinear relationship of peak current with scan rate for a *poly*-RuAAP²⁺/PETA grating-patterned film. (a) Anodic peak currents (circles); (b) Baseline-corrected cathodic peak currents (squares). Peak currents measured at scan rates of 5, 10, 20, 50, and 100 $\text{mV}\cdot\text{s}^{-1}$, 0.1 M (n-Bu₄N)PF₆ / CH₂Cl₂ electrolyte.

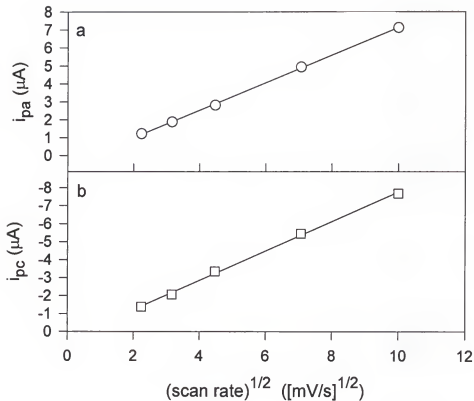


Figure 2.20. Linear relationship of peak current with the square root of scan rate for a *poly*-RuAAP²⁺/PETA grating-patterned film. (a) Anodic peak currents (circles) and the fit by linear regression ($r^2 = 0.9995$); (b) Baseline corrected cathodic peak currents (squares) and the fit by linear regression ($r^2 = 0.9985$). Peak currents measured at scan rates of 5, 10, 20, 50, and 100 $\text{mV}\cdot\text{s}^{-1}$, 0.1 M (n-Bu₄N)PF₆ / CH₂Cl₂ electrolyte.

The surface waves of a *poly*-RuAAP²⁺/PETA film are significantly broader than the 90.6 mV predicted by the thin-layer electrochemical model for a one-electron redox process, and are not symmetrical about the peak potential. Both of these effects may arise due to deviation from the theoretical assumption that all of the redox sites within the film have the same E°_{surf} . Local variations in the polymer structure or environment may lead to a distribution of E°_{surf} values, which can severely alter the shape of the surface waves. Such distribution of redox potentials within the film could possibly lead to a partially irreversible film oxidation process, arising from temporal charge trapping within the film due to impeded charge transfer between the RuAAP²⁺ sites. This type of phenomenon could partially explain the apparent electrochemical instability of the films to repeated potential cycling, along with other considerations, including film dissolution and alternate forms of irreversible film oxidation.

Surface coverage calculations. The four methods of surface coverage calculation (MLCT absorbance, MLCT oxidative bleaching, cyclic voltammetry, and film composition) listed in Table 2.4 produce fairly consistent results, considering the assumptions made in the calculations and the film characteristics. The most reliable of these methods is the electrochemical integration of the surface waves. This direct measurement represents the electroactive RuAAP²⁺ content of the polymer films. Although the composition-based calculation agrees fairly well with the electrochemically-derived value, it must be regarded with caution, since two significant approximations are involved in its development. The assumption that the initial monomeric RuAAP²⁺ and PETA ratio in the spin-casting solution holds true for the resulting polymer is quite tenuous. The respective rates of polymerization of the two

monomers may differ substantially, leading to an enhancement of one component over the other in the final composition. Also, the approximated film density of 1 g·mL⁻¹ may be inaccurate, although it can reasonably be assumed to be within 10 - 20% of the actual value. Because of these two considerations, a value calculated by this means should be viewed only as an initial estimation rather than as the definitive surface coverage.

Of the four calculations described, the MLCT absorbance method gives the highest surface coverage value. This is not unreasonable, since this value represents the total RuAAP²⁺ content, only a fraction of which may actually be electrochemically active. The lower Γ value calculated by electrochemical MLCT bleaching supports this, demonstrating that the absorption band is not fully bleached at oxidizing potentials. This value is, however, nearly three times that calculated electrochemically by integration of the surface waves. Since both of these calculations involve the redox-active RuAAP²⁺ content, a better correlation would be expected. The MLCT electrochemical bleaching calculation of Γ is based upon the assumption that the molar absorptivity of the monomer would not significantly change upon inclusion into a polymer film. Deviations from Beer's Law typically arise under conditions of high concentration (>0.1 M). Based upon the electrochemically-determined surface coverage ($\Gamma=7 \times 10^{-9}$ mol·cm⁻²) and a typical film thickness (150 nm) from profilometry data, the "concentration" of RuAAP²⁺ in these films can be estimated at 0.47 M. At this high concentration, Beer's Law should not be expected to hold true, thereby explaining the overestimation of Γ by the absorbance data.

Diffraction Experiments

Modulation of diffraction efficiency. The data shown in Figure 2.16 and listed in Table 2.5 demonstrate that the intensity of diffracted light from a grating-patterned *poly-*

RuAAP²⁺/PETA film can be varied by an electrochemical signal. It is apparent that the RuAAP^{2+/3+} redox process occurring within the film brings on the diffraction efficiency modulation effect. Figure 2.16 clearly shows that the onset of DE modulation occurs concomitant with oxidation of the film, as evidenced by the anodic current and the corresponding drop in the intensity of the diffracted beam. This diffraction efficiency change reverses upon scan reversal and the onset of cathodic current arising from re-reduction of the RuAAP³⁺ sites within the film. Moreover, the partial loss of redox activity exhibited by the film between the first and second potential sweep scans is mirrored in large part by the failure of the diffracted beam intensity to recover fully to the initial level established at the beginning of the experiment. An unfortunate limitation to these diffraction modulation experiments is the lack of long-term stability to repeated potential scanning. After several scans, the magnitude of the modulation is diminished, with an effective loss of diffraction switching ability typically complete within twenty potential cycles. This behavior is mirrored in cyclic voltammetry experiments under continuous scanning conditions. Shown in Figure 2.21 are fifteen consecutive oxidative scans between 0.7 and 1.9 V which demonstrate a significant loss of film electroactivity over this period.

This instability to repeated potential cycling may be attributed to degradation of the film, either by dissolution of loosely incorporated RuAAP²⁺ molecules, or small oligomers, and/or by an irreversible trapping of RuAAP³⁺ complexes within the film due to hindered ionic transport or impeded charge transfer between redox sites within the film. It is not necessary for all of the RuAAP²⁺ sites within the film to be either lost or irreversibly trapped to account for the complete loss of film activity. It is likely that only

a fraction of the RuAAP²⁺ sites within the film are accessible to the electrode surface, either by direct contact or remotely through charge exchange between redox sites. Loss of activity in these regions could account for loss of observed modulation ability, while the RuAAP sites which are not accessible and do not participate in the redox events remain intact.

Origin of diffraction efficiency modulation. Since the refractive index of the photopolymer film is higher than that of the electrolyte solution, it can be inferred that upon oxidation of the film, the refractive index of the film decreases, since a lower refractive index difference gives rise to decreased diffraction efficiency. In order to elucidate the source of the refractive index change, one must examine the processes occurring during the redox process. In order for the oxidation process to occur, there must be accompanying mass transport of electrolyte counterions into or out of the film in order to maintain charge balance. The oxidation process increases positive charge within the film, so either positively charged ions must flow out of the film, or anions must flow in. Since there are no positively charged counterions within the film, this charge balance must be achieved by transport of hexafluorophosphate anions from the electrolyte solution into the film. It seems counterintuitive that an increase in anionic concentration should lead to a *decrease* in refractive index, so it is unlikely that this mass transport process is the sole source of the diffraction efficiency modulation.

It has been reported elsewhere^{56,57} that redox processes occurring in polymer films can lead to reversible changes in the thickness of these films. The explanation for this behavior is that redox processes increase or decrease like-charge repulsions between molecular sites within the film and lead to film expansion or contraction, respectively. In

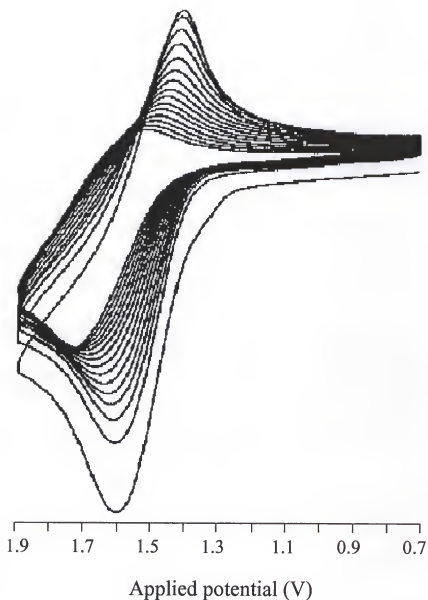


Figure 2.21. Continuous-sweep cyclic voltammetry of a *poly*-RuAAP²⁺/PETA film. Conditions: ITO working electrode substrate, 0.1 M (n-Bu₄N)PF₆ / CH₂Cl₂ electrolyte solution, 0.7 to 1.9 V vs. Ag wire quasi-reference electrode, 15 scans, 100 mV·s⁻¹ scan rate.

the case of the ruthenium-based films in the present study, oxidation of the films leads to an increase in positive charge, which would lead to an expansion of the polymer film. If the film thickness does indeed increase upon oxidation of the film, this effect could conceivably give rise to decreased refractive index as implied by the diffraction results. Given the expected high degree of crosslinking within the film, one may expect that repulsion-induced molecular motion should be restricted to a large degree. It is uncertain if what would be expected to be a small variation in the physical dimensions of the film should lead to a refractive index variation of the degree necessary to account for an approximate 20% change in diffraction efficiency. In the absence of concurrent film thickness and diffraction efficiency modulation data, no decisive conclusion concerning the role of this phenomenon can be drawn.

The spectroelectrochemical data shown in Figure 2.13 demonstrate that the absorbance characteristics of the film change with the redox state of the ruthenium component. If the film were behaving as an absorption grating, the observed bleaching of the MLCT band at 458 nm could lead to a decrease in the diffraction efficiency of wavelengths of light falling within this absorption band. However, as shown in the expansion of the region around the wavelength of the He-Ne laser probe (Figure 2.13, inset), absorbance variation in this region is attributable only to random blank correction errors, and no real absorbance changes at the probe wavelength can be measured.

As described in Chapter 1, the change in film absorption is accompanied by a refractive index variation that extends to longer wavelengths than the absorption band itself. Although there is no apparent absorption change at the probe wavelength, the

refractive index variation at this wavelength can be calculated. Examination of the diffraction efficiency equation below reveals that for the initial state of the grating, all of

$$DE = \exp \left[\frac{-2.3OD}{\cos \theta} \right] \sinh^2 \frac{\pi \Delta k T}{\lambda \cos \theta} + \sin^2 \frac{\pi \Delta n T}{\lambda \cos \theta} \quad (2-14)$$

the variables are known or can be determined experimentally. Assuming an optical density of zero for both the grating film and the electrolyte regions between the grating lines causes the first term in the equation to have a value of 1. Since the film is nonabsorptive at 633 nm in its resting state as well, the peak-null difference Δk in the second term is zero, and the second term is eliminated. The peak-null difference of the refractive indices Δn is simply the refractive index of the bathing electrolyte solution (1.347) subtracted from the experimentally determined film refractive index (1.610). Insertion of this value, along with the values $T = 150$ nm, $\lambda = 633$ nm, and the beam incidence angle $\theta = 0$ results in a calculated initial diffraction efficiency of 0.038.

Although the initial diffraction efficiencies of the films were not measured to provide confirmation of this value, comparison with the calculated DE for the oxidized film can yield the diffraction efficiency modulation ΔDE , for which experimental data is available. In the oxidized state, the grating film exhibits no change in optical density (recall Figure 2.13) at 633 nm, so again the peak-null difference of the imaginary component Δk is zero. What is not experimentally known is the refractive index of the film in its oxidized state (thus Δn is unknown), so the diffraction efficiency cannot be determined directly. Manipulation of the equation in the iterative manner described by Hauser,⁵⁸ however, allows us to calculate how much of a change in the refractive index peak-null difference, $\Delta(\Delta n)$, is required in order to obtain diffraction efficiency

modulations of magnitudes comparable to those observed experimentally. Beginning with the values used in the calculation above, the refractive index of the grating material is incrementally decreased, which, by subtracting from the initial DE calculated above, yields a range of Δ DE values. Shown in Figure 2.22 is a plot of these Δ DE values vs. the change in the refractive index peak-null difference, $\Delta(\Delta n)$. The curve indicates that in order to observe DE modulations of 10-27% (see Table 2.5), Δn must decrease by 0.014 to 0.039, respectively. This corresponds to a decrease in the film refractive index, initially at 1.610, to between 1.571 and 1.596 upon electrochemical oxidation. This somewhat broad range of $\Delta(\Delta n)$ values is illustrative of the limited reversibility of the diffraction efficiency modulation *within a given experiment*. As shown in Table 2.5, the initial Δ DE values are grouped much more tightly, ranging only from 23 to 27%. Consideration of only the first-scan Δ DE values results in a narrower range of refractive index modulations, $\Delta(\Delta n) = 0.033$ to 0.039, which is descriptive of the *potential* DE modulation capability of these *poly*-RuAAP²⁺ gratings.

Experimental

N,N-dimethylformamide was purified by vacuum distillation and stored over molecular sieves. Acetonitrile and methylene chloride for electrochemical experiments were distilled over calcium hydride. Tetrabutylammonium hexafluorophosphate was recrystallized twice from ethanol/water. All other solvents and reagents used are reagent grade and used as received without further purification, unless otherwise noted. Column chromatography was performed using neutral alumina (Brockman Activity III) from

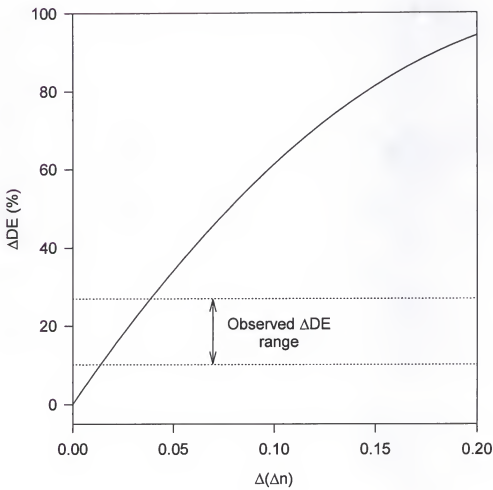


Figure 2.22. Determination of the refractive index modulation for a *poly*-RuAAP²⁺ grating.

Fisher. ^1H and ^{13}C NMR spectra were recorded on a General Electric QE-300 or a Varian VXR-300 spectrometer. Elemental analyses were performed by the University of Florida Department of Chemistry Analytical Services. An Integrated Technologies P-6000 spin coater was used for spin casting of films prior to lithographic exposure. Photopolymer film thickness was measured using a Sloan Dektak profilometer with a 12 μm stylus tip. Optical transmission microscope images were obtained using a Nikon F4s 35 mm SLR camera attached to a Nikon Optiphot-POL microscope. Scanning electron microscope images were obtained using a JEOL JSM-6400 SEM at the University of Florida Major Analytical Instrumentation Center.

Chemical Syntheses

Synthesis of 5-nitro-1,10-phenanthroline (5-np). Modification of the method of Smith and Cagle⁵⁹ was used as follows: 1,10-phenanthroline (5 g, 27.7 mmol, Aldrich) was dissolved in 25 mL of fuming H_2SO_4 and heated to ca. 160° C in an oil bath. Concentrated HNO_3 (15 mL) was added to the solution dropwise with stirring to maintain a solution temperature of 165-170° C. After final addition, heating was continued while the solution was stirred for an additional 30 minutes. After cooling, the reaction mixture was poured over ca. 500 g of ice and 30% NaOH was added to adjust to a pH of 7, inducing precipitation of the product. The yellow solid was collected by filtration on a medium-porosity glass frit, washed with H_2O , and dried under vacuum at room temperature. Yield: 4.29 g (69%). ^1H NMR (300 MHz, CDCl_3): 87.79 (m, 2H), 8.42 (dd, 1H), 8.67 (s, 1H), 9.00 (dd, 1H), 9.29 (dd, 1H), 9.34 (dd, 1H).

The following two compounds were prepared by modification of the methods reported by Gillard and Hill⁶⁰.

Synthesis of Ru^{II}(5-np)₃(PF₆)₂. Ruthenium trichloride trihydrate (1.7 g, 6.5

mmol, Aldrich) was dissolved in 150 mL H₂O and 9 drops of 0.1 M HCl was added. The solution was heated to boiling and 5-nitro-1,10-phenanthroline (4.8 g, 21.3 mmol) was added. After a 10 minute reflux period, NaH₂PO₂·H₂O (1.03 g, 9.72 mmol) was added and reflux was continued for 1.5 hours. After cooling, the reaction mixture was filtered and to the filtrate was added 3 equivalents of NH₄PF₆ (Aldrich) dissolved in a small amount of H₂O. The resulting orange precipitate was collected by filtration on a glass frit and dried under vacuum at room temperature. The crude product was purified by column chromatography on alumina, eluting with 30% CH₃CN/CH₂Cl₂. Yield: 3.3 g (48%) of purified product. ¹HNMR (300 MHz, CD₃CN): δ 7.77 (m, 2H), 8.15 (m, 1H), 8.20 (m, 1H), 8.81 (dt, 1H), 9.09 (dt, 1H), 9.16 (s, 1H). ¹³CNMR (300 MHz, CD₃CN): δ 117.1, 126.9, 127.1, 128.2, 133.5, 138.7, 144.9, 148.0, 149.2, 154.5, 156.1. Anal. Calcd. for C₃₆H₂₁N₉O₆P₂F₁₂Ru: C, 40.54; H, 1.98; N, 11.82. Found: C, 40.52; H, 2.07; N, 11.79.

Synthesis of Ru^{II}(5-ap)₃(PF₆)₂. (5-ap) = 5-amino-1,10-phenanthroline. Ru^{II}(5-np)₃(PF₆)₂ (1.0 g, 0.937 mmol) was dissolved in 30 mL of concentrated HCl. Tin powder (2.0 g, 16.8 mmol) was added and the mixture was heated to reflux for 45 minutes. After cooling, the pH was adjusted to ca. 11 by addition of 30% NaOH, and several equivalents of NH₄PF₆ dissolved in H₂O was added, resulting in the formation of an orange precipitate, which was collected by filtration on a glass frit. The solid was washed with acetone, and the filtrate was dried over anhydrous MgSO₄, filtered, and evaporated under reduced pressure, yielding the red solid product (0.56 g, 61%). The product could not be chromatographed, and was used without purification for the next step in the synthetic

sequence. ^1H NMR (300 MHz, CD_3CN) of: 85.50 (s, 6H), 7.18 (s, 3H), 7.39 (m, 3H), 7.60 (m, 6H), 7.99 (m, 3H), 8.18 (qd, 3H), 8.58 (qd, 3H).

Synthesis of $\text{Ru}^{\text{II}}(5\text{-aap})_3(\text{PF}_6)_2$ (RuAAP^{2+}). (5-aap) = 5-acrylamido-1,10-phenanthroline. $\text{Ru}^{\text{II}}(5\text{-aap})_3(\text{PF}_6)_2$ (0.40 g, 0.41 mmol) was dissolved in 20 mL CH_2Cl_2 and 15 mL CH_3CN (both solvents dried over calcium hydride). Triethylamine (0.25 g, 2.5 mmol) and acryloyl chloride (0.56 g, 6.2 mmol, Aldrich) were added to the stirred solution, inducing formation of an orange precipitate. After 40 hours, the reaction mixture was evaporated to dryness under reduced pressure. The red solid was dissolved in a mixture of acetone and H_2O and NH_4PF_6 (ca. 10 equivalents) was added. Upon removal of the acetone under reduced pressure, the resulting red solid was collected by filtration on a glass frit, dissolved in a small amount of CH_3CN , and re-precipitated by dropwise addition to Et_2O . The red solid was purified by column chromatography on alumina, eluting with 50% $\text{CH}_3\text{CN}/\text{CH}_2\text{Cl}_2$ to afford the orange-red solid product (0.35 g, 85%). ^1H NMR (300 MHz, CD_3CN): 85.92 (dd, 3H), 6.48 (dd, 3H), 6.67 (dd, 3H), 7.59 (septet, 3H), 7.66 (septet, 3H), 7.96 (tt, 3H), 8.07 (td, 3H), 8.54 (dd, 3H), 8.70 (s, 3H), 8.72 (d, 3H), 9.04 (s, 3H). ^{13}C NMR (300 MHz, CD_3CN): 8125.0, 128.0, 128.1, 129.3, 134.8, 139.9, 146.2, 149.2, 150.3, 155.8, 157.4. Anal. Calcd. for $\text{C}_{45}\text{H}_{33}\text{N}_9\text{O}_3\text{P}_2\text{F}_{12}\text{Ru}\cdot 2\text{H}_2\text{O}$: C, 46.01; H, 3.30; N, 10.73. Found: C, 45.96; H, 3.02; N, 10.59.

Electrochemical/Optical Experiments

Indium-tin oxide (ITO) glass optically transparent electrodes (Delta Technologies, Stillwater, MN) were used as the substrates for photopolymer film fabrication. Prior to

film fabrication, the substrates were washed with acetone and dried under a stream of nitrogen. When mounted in the electrochemical cell, the active electrode area exposed to the electrolyte solution was 0.0792 cm^2 . Cyclic voltammograms were recorded using a Bioanalytical Systems CV-27 voltammograph alone or in conjunction with a MacLab/4e analog-to-digital converter (ADInstruments) and electrochemical software. All reported potentials are relative to a Ag wire quasi-reference electrode ($\approx +0.05\text{ V}$ vs. SSCE in 0.1 M (n-Bu₄N)PF₆/CH₃CN) which was employed due to space constraints in the electrochemical cell used for the optical studies. The electrolyte solutions used for the experiments were 0.1 M tetrabutylammonium hexafluorophosphate in either acetonitrile (dissolved monomer) or methylene chloride (photopolymer film). UV-visible absorbance was measured using a Hewlett-Packard 8452A diode-array spectrophotometer. Spectroelectrochemical experiments were performed using the HP 8452A in conjunction with the BAS CV-27 voltammograph. Instrumentation used for the optical diffraction studies is described in the Appendix.

CHAPTER 3
MIXED AMPLITUDE/PHASE GRATINGS BASED ON
A BENZYLVIOLGEN MOIETY

Introduction

Viologen compounds (N,N' -diquaternized 4,4'-bipyridines) have long been employed for numerous applications.⁶¹ While the simplest of these molecules, methyl viologen (paraquat), found early utility in the agricultural field as an effective contact herbicide,⁶² chemists have exploited the favorable properties of these compounds in a wide range of interesting applications. Viologens are excellent electron acceptors, and have thus been widely employed in photochemical electron transfer^{63,64} and spatial charge separation schemes, and their electron transfer mediation abilities have been exploited for use as phase-transfer and biomolecule redox catalysts. Viologens incorporated into electroactive films on electrode surfaces have found use in mediated charge trapping,⁶⁵ fabrication of microelectrochemical devices,^{6,66} and electrochromism.⁶⁷ There have been numerous strategies reported for formation of viologen-containing films on electrode surfaces, several of which are illustrated in Figure 3.1.^{27,28,56,63,68-72}

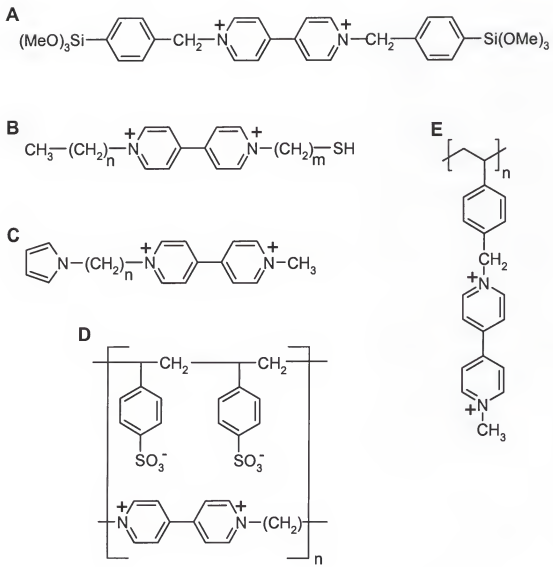


Figure 3.1. Several strategies for immobilization of viologens onto electrode surfaces.
 A: Hydrolysis polymerization of Si(OMe) groups (ref. 56).
 B: Thiol self-assembly onto a gold surface (ref. 69).
 C: Attachment to electropolymerizable monomers (ref. 70).
 D: Electrostatic binding to an anionic polymer (refs. 27, 28).
 E: Polymerization of a vinyl-substituted viologen (ref. 63).

Results

Photopolymer Film Fabrication

Film composition. The films described in this chapter are largely comprised of the redox monomer vinylbenzyl viologen, VBV^{2+} .^{49,50} The structure shown in Figure 3.2 represents one of three structural isomers in the mixture of monomers actually used, which differ in the position of the vinyl functionality on the terminal phenyl substituents. Based upon the isomer ratio of 70% *meta*- and 30% *para*-substitution of the vinylbenzyl chloride mixture used for the synthesis (Figure 3.3), the resulting isomers are 1,1'-bis[(3-vinylphenyl)methyl]-4,4'-bipyridinium (*meta*-*meta*, 49%), 1-(3-vinylphenyl)methyl-1'-(4-vinylphenyl)methyl-4,4'-bipyridinium (*meta*-*para*, 42%), and 1,1'-bis[(4-vinylphenyl)methyl]-4,4'-bipyridinium (*para*-*para*, 9%). It is expected that the three isomers should polymerize equally well, so this mixture was used for film fabrication and, for the sake of convenience, is collectively referred to simply as vinylbenzyl viologen, VBV^{2+} .

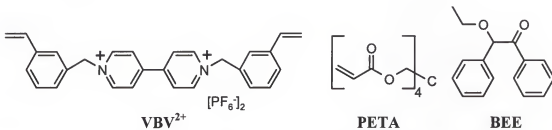


Figure 3.2. Components of spin-cast films for photolithographic patterning.

Photopolymerization of VBV^{2+} occurs via the styrene appendages, which presumably copolymerize with the added crosslinking agent pentaerythritol tetraacrylate (PETA) as described in Chapter 2. In the present films, PETA again also serves as a convenient co-solvent, allowing for formation of homogeneous films and preventing

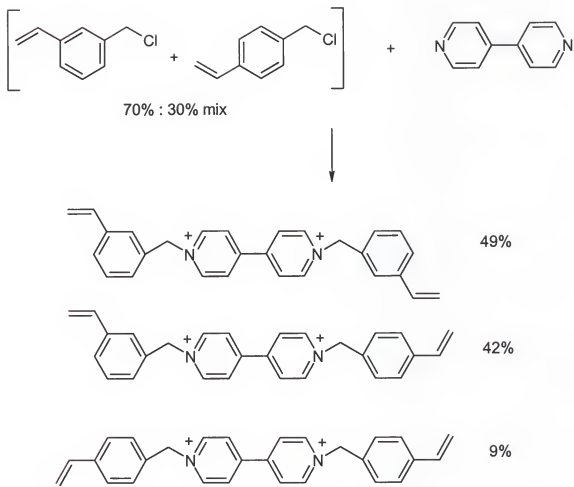


Figure 3.3. VBV^{2+} preparation and product mixture. The percentages shown are statistical approximations based upon the isomer composition of the vinylbenzyl chloride reagent mixture used in the reaction.

crystallization of VBV^{2+} after spin-casting and carrier solvent evaporation. The third film component, benzoin ethyl ether (BEE), initiates the polymerization process through light-induced Norrish Type I cleavage to form a benzoyl and a benzyl ether radical. Both of these radicals are capable of initiating the polymerization of the acrylate appendages of PETA, although it is uncertain if the benzyl ether radical can initiate the polymerization of the styrene-based VBV^{2+} monomer directly.

Lithographic technique. The lithographic polymerization and patterning methodology described in Chapter 2 and outlined in Figure 2.5 is employed for fabrication of *poly*- VBV^{2+} /PETA photopolymer films. Listed in Table 3.1 are the quantities of the three chemical components used for spin-casting of the monomeric film prior to exposure. A stock solution of PETA (0.33 mg/ μL) is prepared by diluting 1 g of the viscous liquid with dimethylformamide to a volume of 3 mL. The photoinitiator stock solution is prepared by dissolving 0.021 g of BEE in 1 mL of dimethylformamide. To prepare solutions for spin-coating, 6 mg of VBV^{2+} is dissolved in 6 μL of the BEE stock solution and 9 μL of the PETA stock (or multiples thereof), corresponding to VBV^{2+} , BEE, and PETA concentrations of 0.59 M, 0.57 M, and 0.037 M, respectively. A capillary or autopipet is used to place 3-4 μL of this solution onto the ITO substrate and the solution is manually spread over the surface using a glass rod. The ITO slide is placed in a spin-coater and spun at 4000-6000 rpm for 15 s to remove excess solution and produce a thin homogeneous film. After a brief drying period in ambient air, the film is placed in direct contact with a chrome-on-glass lithographic mask and irradiated face-on using a medium-pressure mercury lamp (intensity $\approx 60 \text{ mW}\cdot\text{cm}^{-2}$) at a distance of ca. 1 in. for 2-3 minutes. Following exposure, the irradiated film is removed from the mask

and the negative-tone *poly*-VBV²⁺/PETA lithographic image is developed by sequential immersion and gentle agitation in methanol, methylene chloride, and 1:1 methanol:methylene chloride (15-20 s each), and is dried under a gentle stream of nitrogen. The lateral resolution of the lithographic features is inspected by optical microscopy, and if necessary, any remaining background film in the unirradiated areas can be removed or diminished by prolonged immersion (1-2 min.) in the developing solvents.

Table 3.1. Composition data for PETA and BEE stock solutions and monomer/initiator solutions used for spin-coating.

Component	Stock Solutions ^a			Spin-Coating Mixture ^a		
	mg/ μ L	μ mol/ μ L	μ L used	mg added	μ mol added	Concentration, M (in 15 μ L)
VBV ²⁺	-	-	-	6	8.8	0.59
PETA	0.33	0.94	9	3	8.51	0.57
BEE	0.021	0.092	6	0.126	0.55	0.037

a DMF solvent.

Although the photoinitiator concentration (6% overall, 3% per polymerization site) in the films prior to exposure is slightly lower than that used for the *poly*-RuAAP²⁺/PETA films described in Chapter 2 (10% overall, 3.3% per polymerization site), the polymerization process is much more efficient. Exposure times required for satisfactory image formation are reduced from 45 min. to 2 min., while typical film thickness is increased to 400-450 nm, as indicated by profilometry data (Figure 3.4) and edge-on scanning electron microscopy of a freeze-fractured grating-patterned film (Figure 3.5). This increase in polymerization efficiency can be attributed to UV-visible

absorbance differences between RuAAP²⁺ and VBV²⁺. RuAAP²⁺ absorbs strongly at wavelengths in the same region required for Norrish cleavage of BEE ($\lambda_{\text{max}} = 266$ nm),⁵² while VBV²⁺ does not significantly absorb in this region, allowing for more efficient absorption by and cleavage of the photoinitiator.

The lateral lithographic resolution of these films is demonstrated by optical transmission microscope and scanning electron microscope images. In Figure 3.6 are optical microscope images of a film patterned using the USAF 1957 test pattern depicted in Figure 2.6, magnified to show groups 4-7. An expansion of elements 1-3 of group 7, having linewidths of 3.9, 3.5, and 3.1 μm , are shown in the scanning electron microscope image of Figure 3.7. Although some thin background film is present between the polymer lines (arising from edge diffraction by the lithographic mask), there is reasonable reproduction of the mask features down to linewidths of approximately 4 μm . There is a marked improvement in the resolution of the horizontal lines of these patterns over those of the *poly*-RuAAP²⁺/PETA films shown in Figure 2.6. This was achieved by limiting exposure of the film to light which was impinging approximately perpendicular to the surface of the substrate. In effect, the film was irradiated through a 1 in. long opaque 'tunnel' situated between the lamp and the lithographic mask. Shown in Figure 3.8 are optical microscope images of a grating-patterned *poly*-VBV²⁺ film, employed in the diffraction efficiency modulation experiments, having line- and gapwidths of 5 μm .

Electrochemistry and Spectroelectrochemistry

Viologen compounds typically possess three accessible redox states: the dicationic ground state, the singly-reduced cation radical, and the fully reduced neutral species. This behavior is observed for the VBV²⁺ monomer in solution, as shown in

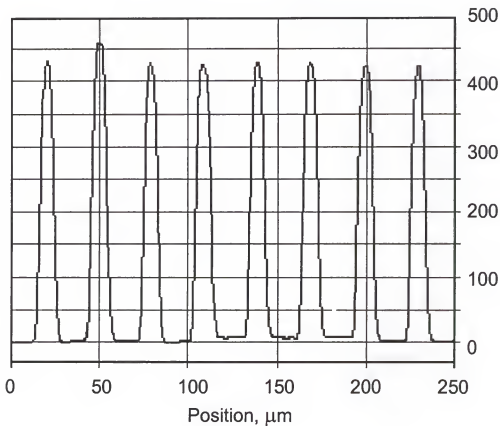


Figure 3.4. Profilometry data from a grating-patterned *poly*-VBV²⁺/PETA film on an ITO substrate. A photopolymer film having linewidths of 5 μm separated by 25 μm gaps was scanned using a 12 μm profilometer stylus tip. The scale on the bottom axis gives the horizontal position across the patterned film, and the scale on the right axis shows the measured thickness in nm.



Figure 3.5. Scanning electron microscope image showing the thickness of a grating-patterned poly-VBV²⁷/PETA photopolymer film. The coated substrate was scored on the uncoated surface perpendicular to the orientation of the grating pattern, frozen by immersion in liquid nitrogen, and broken to reveal a cross-section of the film. The dark region in the bottom half of the image is the glass substrate, and the 5 μm wide polymer lines are the two gray regions approximately centered in the image. The white areas above and around the polymer cross-sections are unfocused polymer 'flakes' distant from the fractured edge.

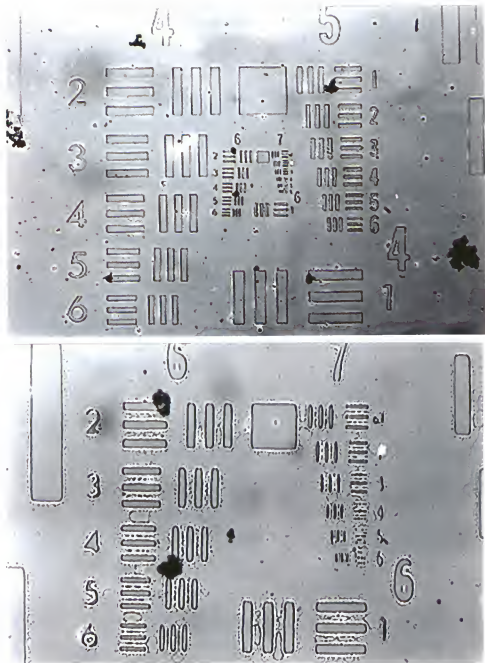


Figure 3.6. Optical transmission microscope images of a poly-VBV^{2+} /PET film patterned using the USAF 1951 target mask. The nearly colorless photopolymer film comprises the small pattern features outlined against the bare ITO electrode substrate. Top: 100x magnification showing groups 4-7. Bottom: 400x magnification of groups 6 and 7.

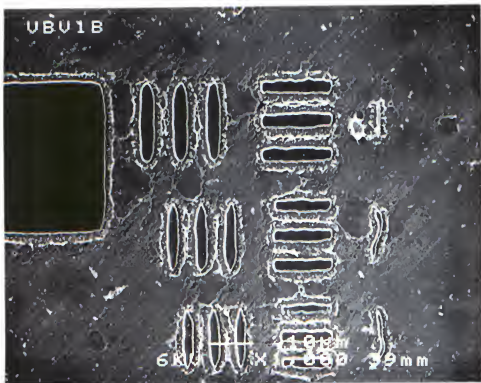


Figure 3.7. Scanning electron microscope image of a *poly*-VBV²⁺/PETA photopolymer film patterned using the USAF 1951 target mask. Elements 1-3 of group 7 are shown, which have line- and gapwidths of 3.9, 3.5, and 3.1 μ m.

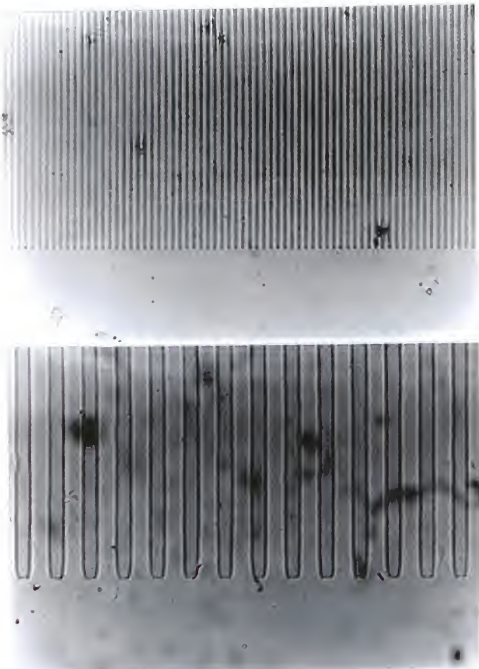


Figure 3.8. Optical transmission microscope images of a grating-patterned poly-VBV^{2+} /PETA photopolymer film. Top: 200x magnification. Bottom: 1000x magnification. The photopolymer lines are the darker regions against the lighter shade of the borosilicate glass substrate.

Figure 3.9, with E° values of -0.13 and -0.53 V for generation of the cation radical and neutral species, respectively. As anticipated, the electrochemical behavior is in large part preserved upon incorporation into a polymeric matrix. Figure 3.10 shows the cyclic voltammetric response of a grating-patterned *poly*-VBV²⁺/PETA film on an ITO electrode substrate. The E° values for both of the redox couples are shifted slightly positive, to 0.0 and -0.45 V for the first and second reductions, respectively. Another noticeable feature is the apparent enhancement of the second reductive wave in comparison to the first, marked by increased peak currents and narrower and sharper surface waves.

The changes of the films' UV-visible absorbance as a function of redox state is shown in Figure 3.11. The figure shows the spectroelectrochemical response as the electrode potential is incrementally stepped through the first and second reductive waves, holding each potential for 30 s prior to absorbance measurement to allow for equilibration of the redox process. At 0.2 V vs. Ag wire the film is in its unreduced redox state, which does not significantly absorb at visible wavelengths. Upon stepping the electrode potential to -0.2 V, corresponding to reduction to VBV⁺, two absorbance bands appear at λ_{\max} values of 375 and 550 nm. These bands disappear upon full reduction of the film at -0.7 V and are replaced by a single intense absorbance at $\lambda_{\max} = 400$ nm. As the applied potential is stepped back in a positive direction (not shown), this band gradually disappears until it is fully replaced by the VBV⁺ absorbances at -0.1 V. Further oxidation of the film leads to complete loss of film absorbance by 0.3 V. This behavior is consistent with the cyclic voltammetric data shown in Figure 3.10.

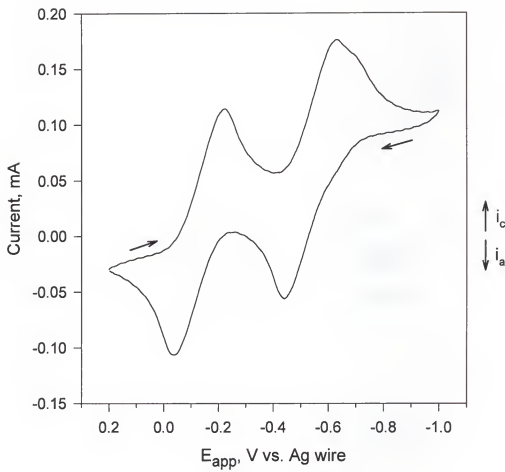


Figure 3.9. Solution cyclic voltammetry of VBV^{2+} monomer. Conditions: ITO working electrode, N_2 -degassed 0.1 M (n-Bu₄N)PF₆/CH₃CN electrolyte, Ag wire quasi-reference electrode, 10 mV·s⁻¹ scan rate.

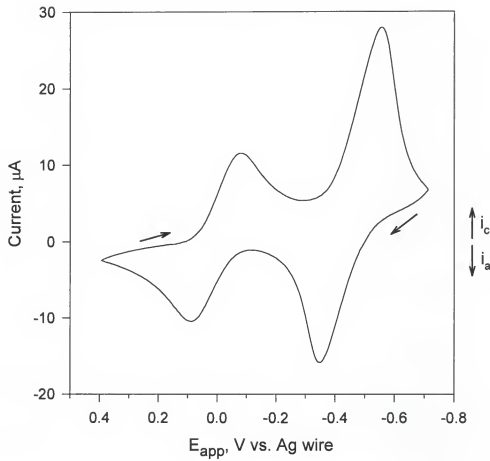


Figure 3.10. Cyclic voltammetry of a *poly*-VBV²⁺/PETA grating-patterned film. Conditions: ITO working electrode substrate, N₂-degassed 0.1 M (n-Bu₄N)PF₆/CH₃CN electrolyte, Ag wire quasi-reference electrode, 10 mV·s⁻¹ scan rate.

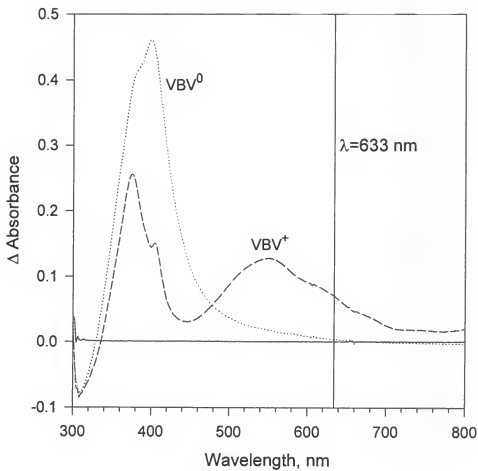


Figure 3.11. Spectroelectrochemical data from a *poly*- VBV^{2+} /PETA grating-patterned film. Absorption spectra were measured at 0.2, -0.3, and -0.7 V vs. Ag wire quasi-reference electrode. Delta absorbance was calculated by subtraction of the film absorbance at 0.3 V. The vertical line indicates the wavelength of the He-Ne laser probe (633 nm) used for diffraction studies.

Interestingly, the observed spectroscopic and electrochemical behavior is quite different for unpatterned *poly*-VBV²⁺/PETA films. Shown in Figure 3.12 is reductive spectroelectrochemical data for a polymer film which was prepared by flood exposure through unpatterned Pyrex glass. Spectra were measured in 100 mV increments from 0.4 to -0.7 V, holding at each potential step for 30 s prior to absorbance measurement. For unpatterned films, only the first reduction is apparently accessible, as indicated by the absence of the absorption band transition shown in Figure 3.11. Even at applied potentials past -1.0 V, no absorptive change associated with the neutral viologen species is observed. The return oxidative sequence shown in Figure 3.13 further illustrates the sluggish electrochemical and spectroscopic response, as indicated by the persistence of the absorption bands associated with the viologen cation radical at applied potentials which are ordinarily sufficiently positive to regenerate the nonabsorbing dicationic state. This irreversibility is clearly demonstrated in the cyclic voltammetric data shown in Figure 3.14. The first potential scan exhibits a cathodic current peak at -0.05 V, corresponding to reduction to the viologen cation radical. At more negative potentials, there is a slight indication of possible partial reduction to the neutral state, but the absence of anodic current flow on the return scan demonstrates the irreversibility of the reductive redox process. A second subsequent scan shows essentially complete loss of electroactivity of the polymer film within this potential range.

Quantification of Electrode Surface Coverage

The redox-active cross-sectional surface coverage values, Γ , for *poly*-VBV²⁺/PETA films can be calculated in the same manner as described in Chapter 2, equations 2-5 through 2-8. Integration of the surface wave current over time (eq. 2-5) gives the

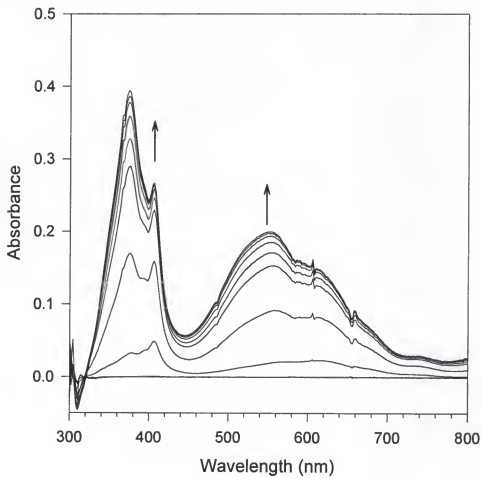


Figure 3.12. Reductive spectroelectrochemical data from an unpatterned *poly*-VBV²⁺/PETA film prepared by flood exposure without the use of a lithographic mask. Absorption spectra were measured in 100 mV increments from 0.2 to -0.7 V vs. Ag wire, allowing equilibration for 30 s prior to each measurement. The arrows indicate the growth of the two absorption bands with increasingly negative applied potentials.

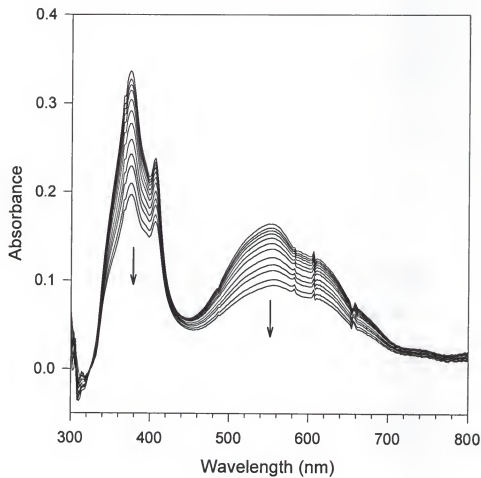


Figure 3.13. Spectroelectrochemical data depicting the re-oxidation of a *poly*-VBV²⁺/PETA film subsequent to the reductive process shown in Figure 3.13. Absorption spectra were measured in stepwise 100 mV increments from -0.7 to 0.4 V, holding each potential for 30 s prior to each measurement. The arrows indicate the incomplete absorptive loss upon application of increasingly positive applied potentials.

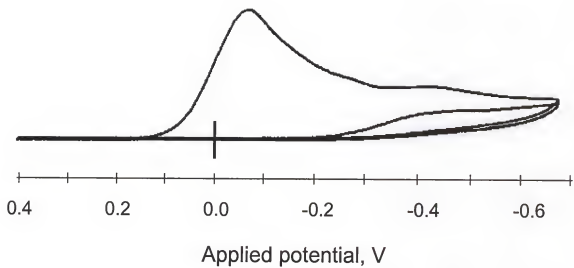


Figure 3.14. Cyclic voltammetry of an unpatterned *poly*-VBV²⁺/PETA photopolymer film. Conditions: N₂-degassed 0.1 M (n-Bu₄N)PF₆/DMF electrolyte, ITO working electrode substrate, 2 scans, 0.4 to -0.7 V vs. Ag wire, 10 mV·s⁻¹ scan rate.

charge passed by reduction of the film, q_f (coulombs, C), which is in turn converted to moles by dividing by the Faraday constant (eq. 2-6, $F = 9.648 \times 10^4 \text{ C} \cdot \text{mol}^{-1}$). Division by the area of the film, A_f (cm^2 , $A_f = 0.5 \times$ electrode area for a grating-patterned film), provides the electrochemically calculated surface coverage, Γ_E ($\text{mol} \cdot \text{cm}^{-2}$, eq. 2-7, 2-8). Collected in Table 3.2 are cyclic voltammetric data from ten grating-patterned *poly*-VBV²⁺/PETA films and the corresponding surface coverage values calculated from Equation 2-8. The average surface coverage value of $\Gamma_E = 3.18 \times 10^{-8} \text{ mol} \cdot \text{cm}^{-2}$ agrees well with those reported by Bookbinder and Wrighton for structurally similar benzylviologen polysiloxane films.⁶

A composition-based calculation of surface coverage analogous to that described in Chapter 2 can be used to verify the value calculated above. Again, a rectangular stripe of *poly*-VBV²⁺/PETA is considered, having a width of $5 \mu\text{m}$ ($5 \times 10^{-4} \text{ cm}$), a length of 2 mm (0.2 cm), and a thickness of 400 nm ($4 \times 10^{-5} \text{ cm}$) based upon the profilometry data in Figure 3.4. The mass of the film can be calculated by multiplying the volume of this film section ($V_f = 4.0 \times 10^{-9} \text{ cm}^3$) by the film density, d_f (eq. 3-1). Based upon the initial

$$\text{mass}_{\text{film}} = V_f \cdot d_f \quad (3-1)$$

$$\text{mass}_{\text{VBV}} = 0.67 \cdot \text{mass}_{\text{film}} \quad (3-2)$$

$$n_{\text{VBV}} = \frac{\text{mass}_{\text{VBV}}}{\text{MW}_{\text{VBV}}} \quad (3-3)$$

$$\Gamma_C = \frac{n_{\text{VBV}}}{A_f} \quad (3-4)$$

spin-coating mixture, VBV²⁺ is assumed to account for 67% of the total film mass, and so the mass of VBV²⁺ (eq. 3-2) and subsequently the number of moles of VBV²⁺

Table 3.2. *Poly-VBV*²⁺ electrochemical and surface coverage data.

Electrode #	q_c^a (μ C)	q_a^b (μ C)	q_{ave}^c (μ C)	Γ_E^d (mol·cm ⁻²)
1	115.92	94.99	105.46	2.76×10^{-8}
2	104.25	94.19	99.22	2.60×10^{-8}
3	122.04	111.73	116.89	3.06×10^{-8}
4	120.59	125.02	122.81	3.21×10^{-8}
5	101.59	128.96	115.28	3.02×10^{-8}
6	122.76	144.10	133.43	3.49×10^{-8}
7	141.36	159.23	150.30	3.93×10^{-8}
8	144.34	157.78	151.06	3.95×10^{-8}
9	109.56	99.82	104.69	2.74×10^{-8}
10	120.43	112.78	116.61	3.05×10^{-8}
ave =				3.18×10^{-8}

Conditions: grating-patterned *Poly-VBV*²⁺/PETA film, 0.1 M (n-Bu₄N)PF₆/DMF electrolyte (N₂ degassed), 0.2 to -0.5 V vs. Ag wire (*Poly-VBV*^{2+/+} couple), 100 mV·s⁻¹ scan rate.

a Integration of cathodic current wave.

b Integration of anodic current wave.

c Average value of q_c and q_a to correct for baseline estimation error; value used for surface coverage calculation.

d Active electrode surface area exposed to electrolyte solution = 0.0792 cm², surface area of grating-patterned film = 0.0396 cm².

(eq. 3-3) in the film can be calculated. The theoretical surface coverage can then be calculated by dividing this value by the area of the film, A_f (eq. 3-4). Inserting an assumed approximate film density of $1.0 \text{ g}\cdot\text{cm}^{-3}$, a VBV^{2+} molecular weight of $680.46 \text{ g}\cdot\text{mol}^{-1}$, and a cross-sectional surface area of $1.0 \times 10^{-4} \text{ cm}^2$ into the equations results in a calculated surface coverage of $\Gamma_C = 3.94 \times 10^{-8} \text{ mol}\cdot\text{cm}^2$. While this value of Γ_C is by no means conclusive, it does provide a reasonable estimation, and is comparable to the electrochemically determined surface coverage.

Extinction Coefficients.

Due to the questionable validity of using solution-derived UV-visible absorbance data for calculations involving high refractive index films,^{ref} spectroelectrochemical data is not used for calculation of surface coverage. Equation 2.4 can be rearranged, however, to calculate the extinction coefficients, ϵ , based upon spectroelectrochemical data and the Γ_E value calculated above:

$$\epsilon = \frac{2A}{\Gamma_E}. \quad (3-5)$$

Collected in Table 3.3 are spectroelectrochemical data from six grating-patterned *poly*- VBV^{2+} /PETA films. The electrode potential was stepped in 100 mV increments between 0.3 and -0.7 V vs. Ag wire, holding each potential for 30 s prior to absorbance measurement. Film absorbances at -0.2 (two bands) and -0.7 V (single absorbance) are listed, corresponding to VBV^+ and VBV^0 , respectively. Inserting this data into equation 3-5 above results in average extinction coefficients for VBV^+ of $1.35 \times 10^7 \text{ cm}^2\cdot\text{mol}^{-1}$ ($13,500 \text{ M}^{-1}\cdot\text{cm}^{-1}$) and $7.16 \times 10^6 \text{ cm}^2\cdot\text{mol}^{-1}$ ($7160 \text{ M}^{-1}\cdot\text{cm}^{-1}$) for the 376 nm and 550 nm

bands, respectively, and a value of $\epsilon = 2.98 \times 10^7 \text{ cm}^2 \cdot \text{mol}^{-1}$ ($29,800 \text{ M}^{-1} \cdot \text{cm}^{-1}$) for the single VBV^0 absorption band at 400 nm.

Diffraction Experiments.

Swept-potential DE modulation experiments. As was described in Chapter 2 for *poly*-RuAAP²⁺/PETA films, grating-patterned *poly*- VBV^{2+} /PETA films also behave as optical diffraction gratings and split light from a laser probe into several diffractive orders. In a manner analogous to that described in the previous chapter, the diffraction efficiency (DE) of these gratings can be modulated by a reductive electrochemical signal. An interesting feature of these films, however, is the dual-wave redox nature of VBV^{2+} , which allows for two-stage DE modulation correlated with the $\text{VBV}^{2+/+}$ and $\text{VBV}^{+/0}$ redox couples.

DE modulation arising from the $\text{VBV}^{2+/+}$ transition in 0.1 M (n-Bu₄N)PF₆/DMF is shown in Figure 3.15. As the electrode potential is scanned between 0.1 and -0.4 V vs. Ag wire (part **a**), the reduction and reoxidation of the film species is apparent from the cathodic and anodic current flow (part **b**). Coupled to the reduction/oxidation process are modulations of the intensities of a first-order diffracted beam and the zero-order undiffracted beam (parts **c** and **d**, respectively). As cathodic current begins to flow during the first reductive potential scan, the intensity of the diffracted beam begins to rise accordingly, reaching a level approximately 68% higher than the initial intensity, while the undiffracted beam intensity falls approximately 13%. Subsequent scans, however, exhibit diminished current flow and beam intensity modulation with each consecutive cycle.

Table 3.3. Spectroelectrochemical data and extinction coefficient calculations for several grating-patterned *poly*-VBV²⁺/PETA films.

Exp. #	VBV ⁺		A ₂ (λ _{max}) ^{a,c}	VBV ⁺		VBV ⁰ (cm ² ·mol ⁻¹)
	A _{1a} (λ _{max}) ^{a,b}	A _{1b} (λ _{max}) ^{a,b}		ε _{1a} ^{b,d} (cm ² ·mol ⁻¹)	ε _{1b} ^{b,d} (cm ² ·mol ⁻¹)	
1	0.256 (376)	0.128 (548)	0.461 (400)	1.61 x 10 ⁷	8.05 x 10 ⁶	2.90 x 10 ⁷
2	0.229 (376)	0.123 (550)	0.475 (400)	1.44 x 10 ⁷	7.74 x 10 ⁶	2.99 x 10 ⁷
3	0.219 (376)	0.120 (550)	0.476 (400)	1.38 x 10 ⁷	7.55 x 10 ⁶	2.99 x 10 ⁷
4	0.226 (374)	0.119 (548)	0.567 (400)	1.42 x 10 ⁷	7.48 x 10 ⁶	3.57 x 10 ⁷
5	0.186 (376)	0.100 (552)	0.461 (398)	1.17 x 10 ⁷	6.29 x 10 ⁶	2.90 x 10 ⁷
6	0.174 (374)	0.093 (552)	0.406 (398)	1.09 x 10 ⁷	5.85 x 10 ⁶	2.55 x 10 ⁷
ave.	0.215	0.114	0.474	1.35 x 10 ⁷	7.16 x 10 ⁶	2.98 x 10 ⁷

a Delta absorbance values calculated by subtraction of film absorbance at 0.3 V.

b Applied potential = -0.2 V vs. Ag wire.

c Applied potential = -0.7 V vs. Ag wire.

d Calculated using $\Gamma_E = 3.18 \times 10^{-8} \text{ mol} \cdot \text{cm}^{-2}$.

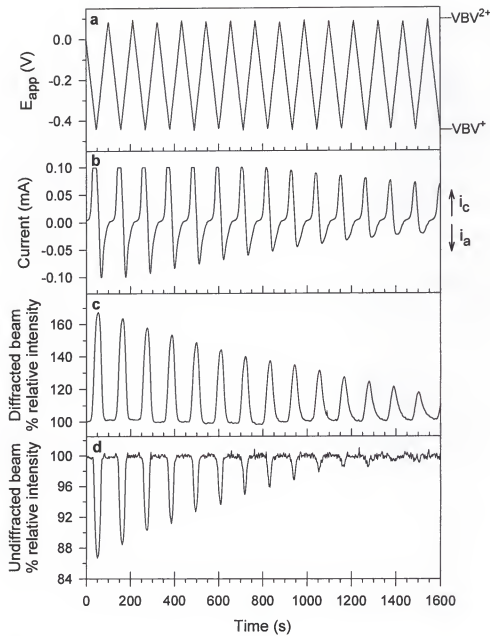


Figure 3.15. Cyclic voltammetric modulation of the diffraction efficiency of a *poly*- VBV^{2+} /PETA grating-patterned film. Conditions: 0.1 M (n-Bu₄N)PF₆/DMF electrolyte, Ag wire quasi-reference electrode, ITO working electrode substrate, 10 mV·s⁻¹ scan rate. (a) Applied potential scanned through the $\text{VBV}^{2+/+}$ redox couple. (b) Cyclic-voltammetric current response. (c) Relative intensity of a first-order diffracted beam. (d) Relative intensity of the transmitted zero-order undiffracted beam.

Electrolyte effects. This instability can be attributed, at least in part, to the solubility of the parent monomer, VBV^{2+} in the electrolyte solution. The initial state of the polymer is as the PF_6^- salt, which is quite soluble in polar organic solvents such as DMF. It is likely that trapped VBV^{2+} monomers and/or small oligomers are simply dissolving in the electrolyte solution as the experiment proceeds, leading to loss of electrochemical response. Film stability can be enhanced, however, by changing the anionic portion of the electrolyte. The chloride salt of monomeric VBV^{2+} is insoluble in organic solvents and dissolves only in H_2O , so using a chloride-containing electrolyte salt can significantly reduce film dissolution. This is demonstrated in the first seven applied potential cycles (for $t = 0$ to 1000 s, part a) of Figure 3.16, in which the experiment is conducted using $(\text{n-Bu}_4\text{N})\text{Cl}/\text{DMF}$ as the bathing electrolyte solution. Cycling through the $\text{VBV}^{2+/+}$ couple in this case results in anion exchange of Cl^- (which is present in large excess) for PF_6^- via charge-compensating counterion flow during the redox process. Formation of the organic-insoluble chloride salt in this manner leads to stable and reproducible modulation of both the diffracted and undiffracted beam intensities (parts b and c of the figure) during redox cycling.

Collected in Table 3.4 is data comparing the stability of *poly*- VBV^{2+} /PETA films to successive redox scanning in hexafluorophosphate and chloride-containing electrolyte solutions. Listed are the observed relative changes in diffracted beam intensity during the first (Δdiff_1) and fifth (Δdiff_5) reductive potential scans, and the percent loss of DE modulation ability over five cycles ($\Delta\{\Delta\text{diff}_{1-5}\}$). Although the DE modulation stability

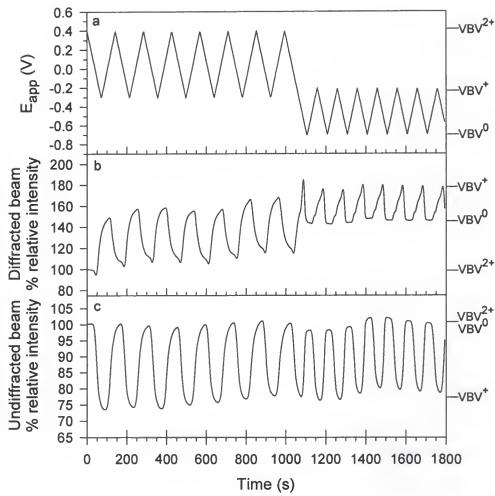


Figure 3.16. Electrochemical modulation of the diffraction efficiency of a poly-VBV^{2+} /PETA grating-patterned film. Conditions: 0.1 M (n-Bu₄N)Cl/DMF electrolyte, Ag wire quasi-reference electrode, 10 mV·s⁻¹ scan rate. (a) Applied potential scanned through the $\text{VBV}^{2+/0}$ and $\text{VBV}^{+/0}$ couples. (b) Relative intensity of a first-order diffracted beam. (c) Relative intensity of the zero-order undiffracted beam.

shows some variation from film to film in either electrolyte, it is clear that reproducibility is significantly enhanced in the presence of chloride anions.

Bidirectional DE modulation. Figure 3.16 also demonstrates the dual-stage DE modulation which can be achieved by cycling the electrode potential individually through the $\text{VBV}^{2+/+}$ and $\text{VBV}^{+/0}$ redox couples. As the potential is scanned from 0.4 to -0.3 V vs. Ag wire ($\text{VBV}^{2+/+}$), a rise in the first-order diffracted beam intensity and a decrease in the intensity of the transmitted light is again observed, both of which return to their initial levels upon scan reversal. As the potential is scanned through the $\text{VBV}^{+/0}$ couple (-0.2 to -0.7 V), however, the reverse behavior is observed: further reduction to VBV^0 leads not to a second subsequent increase in diffracted beam intensity, but rather a *decrease*. The undiffracted beam also follows a reverse behavior upon full reduction, *increasing* in intensity as VBV^0 is electrochemically generated.

This interesting behavior can be more clearly seen in an expansion of the region from $t = 850$ s to 1250 s, shown in Figure 3.17. The figure shows 1.5 potential sweep cycles through the $\text{VBV}^{2+/+}$ couple and two cycles through $\text{VBV}^{+/0}$, and the resulting diffracted beam intensity variations correlated to electrode current. As the electrode potential is scanned negatively from 0.4 V, the onset of cathodic current flow indicates reduction to VBV^+ . The intensity of the diffracted beam begins to rise at the point labeled *i*, which is already well into the reductive wave. The intensity rises as further film reduction takes place, and continues even after scan reversal. The intensity then begins to fall at the point labeled *ii*, which correlates to the oxidative peak current arising from re-oxidation to VBV^{2+} . The diffracted beam intensity again rises as the film is reduced during the second reductive potential scan, and continues to rise until further film

Table 3.4. Collected swept-potential diffraction efficiency modulation data for grating-patterned *poly*-VBV²⁺/PETA films.

Exp. # ^a	Electrolyte ^b (0.1 M)	Δdiff ₁ ^c (%)	Δdiff ₅ ^d (%)	Δ(Δdiff ₁₋₅) ^e (%)
1	TBAH/DMF	27	8	70
2	TBAH/DMF	40	17	57
3	TBAH/DMF	60	40	33
4	TBAH/DMF	25	15	40
5	TBAH/DMF	39	20	49
6	TBAH/DMF	33	16	52
7	TBAH/DMF	20	10	50
8	TBAH/DMF	42	15	64
9	TBAH/DMF	51	38	25
10	TBAH/DMF	30	12	60
11	TBACI/DMF	19	16	16
12	TBACI/DMF	33	31	6
13	TBACI/DMF	50	50	0
14	TBACI/DMF	40	33	17
15	TBACI/DMF	50	50	0
16	TBACI/DMF	49	48	2
17	TBACI/DMF	48	44	8
18	TBACI/DMF	73	69	5
19	TBACI/DMF	60	56	7
20	TBACI/DMF	76	67	12

^a Conditions: 0.4 to -0.2 V vs. Ag wire (VBV^{2+/+} couple), 10 mV·s⁻¹ scan rate.

^b N₂-degassed solutions. TBAH = (n-Bu₄N)PF₆; TBACI = (n-Bu₄N)Cl.

^c Relative change in first-order diffracted beam intensity during first potential cycle.

^d Relative change in first-order diffracted beam intensity during fifth potential cycle.

^e Percent loss of diffracted beam intensity modulation over five potential cycles:

$$\Delta(\Delta\text{diff}_{1-5}) = (1 - [\Delta\text{diff}_5 / \Delta\text{diff}_1]) \times 100\%.$$

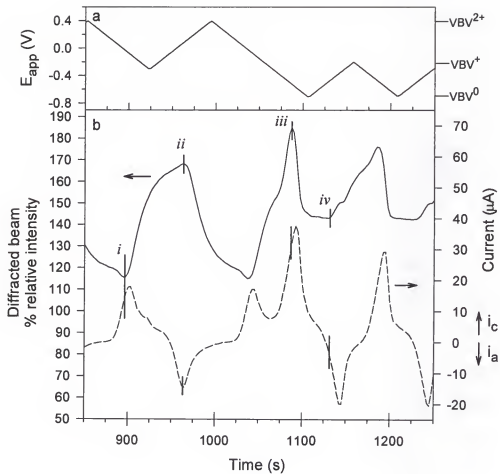


Figure 3.17. Bidirectional electrochemical modulation of the diffraction efficiency of a $poly\text{-}VBV^{2+}$ /PETA grating-patterned film. (a) Applied potential scanned through the $VBV^{2+/+}$ couple (1.5 cycles) and the $VBV^{+/0}$ couple (2 cycles). (b) Solid line: relative intensity of a first-order diffracted beam, scale on left axis. Dashed line: current response, scale on right axis. Lower-case roman numerals mark the diffraction intensity transitions correlated to the cyclic voltammetric current response.

reduction to VBV^0 , as indicated by the second sharper cathodic current peak. At the point labeled *iii*, the DE modulation changes direction, leading to a rapid decrease in diffracted beam intensity as the full reduction to VBV^0 proceeds. The diffracted beam intensity quickly stabilizes at a level of ca. 140% until scan reversal. As VBV^+ is regenerated at point *iv*, the diffracted beam intensity then begins to rise to the level corresponding to the film in the VBV^+ state, until the modulation process is repeated in the next reductive cycle.

Potential-step experiments. The diffraction efficiency of *poly*- VBV^{2+} /PETA gratings can also be modulated by application of a stepwise, rather than scanned, electrochemical signal. Figure 3.18 shows a DE modulation experiment in which the electrode potential is stepped between a nonreducing starting potential of 0.4 V and a potential sufficiently negative to singly reduce the VBV^{2+} sites in the film (-0.15 V). The data shows that while DE modulation is indeed occurring, the 30 s duration of each potential step is insufficient to reach a stable diffracted beam intensity level. Extending the potential step time to 2 minutes (Figure 3.19) yields slightly better results, but the expected intensity plateau is still not achieved within this time period, demonstrating the sluggish electrochemical response of the film. Table 3.5, experiments 1-9, lists data for potential-step experiments through the $\text{VBV}^{2+/0}$ redox couple. Variation of potential step periods reveals that a step duration of greater than or equal to 180 s is required in order to achieve stabilization of diffracted and undiffracted beam intensities (experiments 7-9).

Stepping the potential through the $\text{VBV}^{+/0}$ redox couple, though, affords significantly improved temporal response. This is illustrated in the experiment shown in Figure 3.20. The electrode potential is initially stepped from 0.4 to -0.15 V and held for

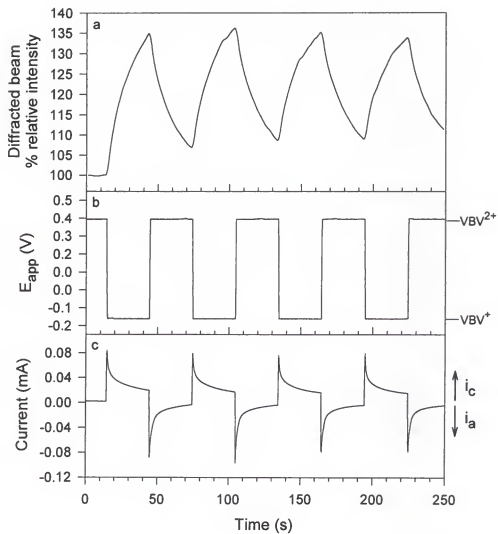


Figure 3.18. Potential-step electrochemical modulation of the diffraction efficiency of a poly-VBV^{2+/+}PETA grating-patterned film. Conditions: 0.1 M (n-Bu₄N)Cl/DMF electrolyte, Ag wire quasi-reference electrode, ITO working electrode substrate, 30 s step time. (a) Relative intensity of a first-order diffracted beam. (b) Applied potential stepped through the VBV^{2+/+} couple. (c) Electrode current response.

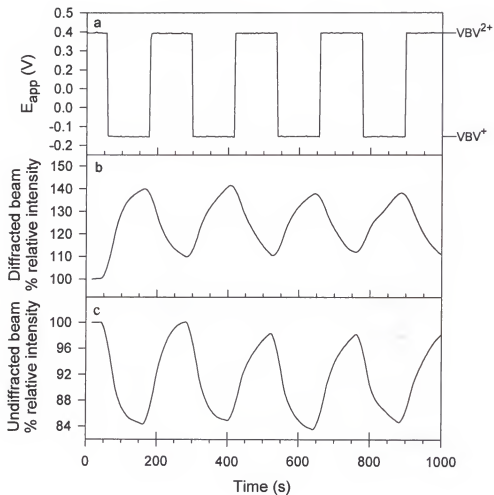


Figure 3.19. Extended potential-step electrochemical modulation of the diffraction efficiency of a *poly*-VBV²⁺/PETA grating-patterned film. Conditions: 0.1 M (n-Bu₄N)Cl/DMF electrolyte, Ag wire quasi-reference electrode, ITO working electrode substrate, 2 min. step time. (a) Relative intensity of a first-order diffracted beam. (b) Relative intensity of the zero-order undiffracted beam. (c) Potential stepped through the VBV^{2+/+} couple.

2 minutes, leading to a slow increase in diffracted beam intensity as film-confined VBV^+ is generated. Upon stepping the applied potential to -0.6 V to fully reduce the film to VBV^0 , the diffracted beam intensity rapidly drops and stabilizes at approximately 117% of the initial level established at the onset of the experiment. Stepping the potential back to -0.2 V causes the intensity to rapidly rise and plateau at 130% as VBV^+ is regenerated. The response of the undiffracted beam mirrors the behavior of the diffracted beam in terms of the direction of the intensity change. However, the three undiffracted beam intensity levels established by the three redox states ($\text{VBV}^{2+} = 100\%$, $\text{VBV}^+ = 80\%$, $\text{VBV}^0 = 98\%$) are not as distinct as those observed for the diffracted beam ($\text{VBV}^{2+} = 100\%$, $\text{VBV}^+ = 130\%$, $\text{VBV}^0 = 117\%$). Further VBV^{+0} potential-step DE modulation data are listed in experiments 10-14 of Table 3.5.

Refractive Index Determination

The refractive index of *poly*- VBV^{2+} /PETA films was calculated in the same manner as described in Chapter 2. A grating-patterned film was mounted in the electrochemical cell used for the diffraction studies and the cell was filled with a series of solvents of known refractive index. The intensity of a first-order diffracted beam was measured using a photodiode, and the diode voltage output reading was plotted vs. the known refractive index of each solvent. Although this first set of data exhibited a poor second-order curve fit, it provided an initial refractive index approximation in the range of 1.56 to 1.57. This region was expanded by repeating the experiment using mixtures of bromobenzene ($n_D = 1.557$) and bromoform ($n_D = 1.587$), and the measurements obtained are collected in Table 3.6. Photodiode outputs from the 1:1, 3:2, 2:1, and 9:1 bromobenzene: bromoform solvent mixtures were plotted and fit to a second-order

Table 3.5. Collected stepped-potential diffraction efficiency modulation data for grating-patterned poly-VBV²⁺/PETA films.

Exp. #	DE ₀ ^a (%)	Step time ^b (s)	VBV ^{2+/+}		VBV ^{+/0}	
			Δdiff ^{c,d} (%)	Δundiff ^{c,e} (%)	Δdiff ^{d,f} (%)	Δundiff ^{e,f} (%)
1	4.9	30 ^g	+30	-1		
2	2.0	75 ^g	+32	-0.8		
3	3.1	120 ^g	+36	-13		
4	1.5	120 ^g	+58	-23		
5	7.1	120 ^g	+30	-16		
6	5.6	180 ^g	+49	-14		
7	7.8	180	+27	-26		
8	9.7	180	+30	-19		
9	5.8	240	+40	-5		
10	4.8	30			-15	+0.5
11	3.8	120			-25	+15
12	8.7	120			-18	+19
13	3.4	120			-11	+8
14	4.3	120			-11	+12
Ave.	5.2		+37	-13	-16	+11
Std. Dev.	2.4		10	9	6	7

Conditions: N₂-degassed (n-Bu₄N)Cl/DMF electrolyte, Ag wire reference electrode.

a Initial diffraction efficiency of a first-order diffracted beam at 0.4 V prior to experiment.

b Length of time potential is held after each step.

c 0.4 to -0.2 V potential step (VBV^{2+/+} couple).

d Relative change in diffracted beam intensity upon stepping to the more negative potential.

e Relative change in undiffracted beam intensity upon stepping to the more negative potential.

f -0.15 to -0.55 V potential step (VBV^{+/0} couple).

g DE modulation effect did not stabilize within this potential step period.

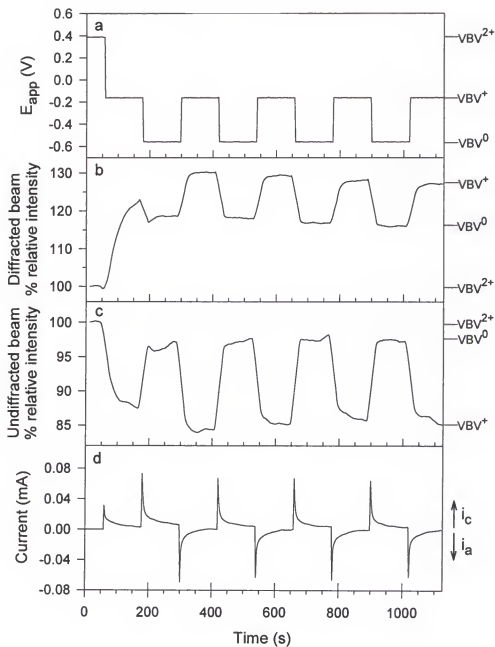


Figure 3.20. Two-stage modulation of the diffraction efficiency of a grating-patterned *poly*- VBV^{2+} /PETA film. Conditions: 0.1 M (n-Bu₄N)Cl/DMF electrolyte, Ag wire quasi-reference electrode, ITO working electrode substrate, 2 min. potential steps. (a) Applied potential stepped through the VBV^{+0} redox couple. (b) Relative intensity of a first-order diffracted beam. (c) Relative intensity of the zero-order transmitted beam. (d) Electrode current response.

regression (Figure 3.21). The curve minimum at 1.564 agrees with the experimentally observed value, which falls between 1.563 and 1.565.

Table 3.6. Data for determination of poly-VBV²⁺/PETA film refractive index.

Br-C ₆ H ₅ :CHBr ₃ ratio ^a	Refractive Index	Photodiode Output (mV)
1:1	1.572	34 ^b
3:2	1.569	12 ^b
2:1	1.567	7 ^b
3:1	1.565	~0
4:1	1.563	~0
5:1	1.562	1
9:1	1.560	10 ^b

a The refractive indices of Br-C₆H₅ and CHBr₃ are 1.557 and 1.587, respectively.

b Data point in curve fit, Figure 3.21.

Electrolyte Effects

With the goal of determining experimental conditions in which the diffraction efficiency could be turned on and off electrochemically rather than just 'dimmed', attempts were made to set the initial conditions (at non-reducing potentials) so that DE=0 by matching the refractive indices of the film and the electrolyte solution.

Electrochemical variation of refractive index would then lead to a nonzero diffraction efficiency (the 'on' state). Based upon the experimental determination of the photopolymer film refractive index described above, several high refractive index solvents were investigated for possible use as electrolyte solvents. Based upon electrolyte salt solubility, three possible candidates were identified: 50% acetone/CH₂I₂,

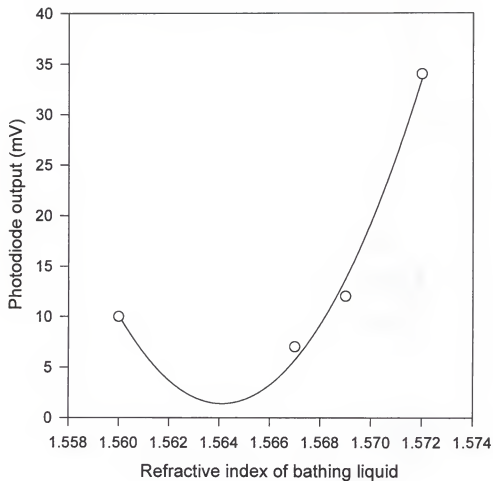


Figure 3.21. Experimental determination of the refractive index of a $\text{poly-VBV}^{2+}/\text{PETA}$ grating-patterned film by variation of the bathing liquid. Circles: data points from Table 3.x (1:1, 3:2, 2:1, and 9:1 $\text{Br-C}_6\text{H}_5:\text{CHBr}_3$ ratios). Line: fitted curve from a second-order regression of the four data points ($r^2 = 0.989$).

80% benzonitrile/CH₂I₂, and nitrobenzene. Cyclic voltammetry of a poly-VBV²⁺/PETA film in these three solvents/solvent mixtures is shown in Figure 3.22. While the cyclic voltammetry in the acetone/CH₂I₂ electrolyte solution appears comparable to that in DMF, the other two exhibited diminished electrochemical response. This was attributed to the inability of these solvents to sufficiently swell the polymer film to the degree required to allow for permeability of electrolyte ion migration required for the redox process to occur. A disappointing hindrance to the use of the acetone/CH₂I₂ electrolyte in DE modulation experiments, however, was the limited long-term miscibility of these two solvents. Over time, the solvents would appear to partially separate, although no clear phase boundary was observed. As a result, a gradual variation of the resting state diffraction efficiency occurred as a refractive index gradient formed within the cell.

Discussion

Film Morphology

Although no chemical analysis was performed on these materials, knowledge of the synthetic procedures and inferences from the experimental details provide evidence of a nonhomogeneous nature of the VBV²⁺/PETA films. The assumption that the two monomers would form a random copolymer is most likely not entirely accurate, and may in fact be quite false. A key consideration is the different functionality of the two monomers. PETA, an acrylate, and VBV²⁺, a styrene derivative, have different free-radical polymerization reactivities, so the likely scenario is that of a blend of two polymers, rather than a single copolymer. This is supported by consideration of the reactivity of the initiating species, BEE. As was stated in Chapter 2, both the benzyl and benzoyl radical species that are produced by Norrish cleavage of the initiator are capable

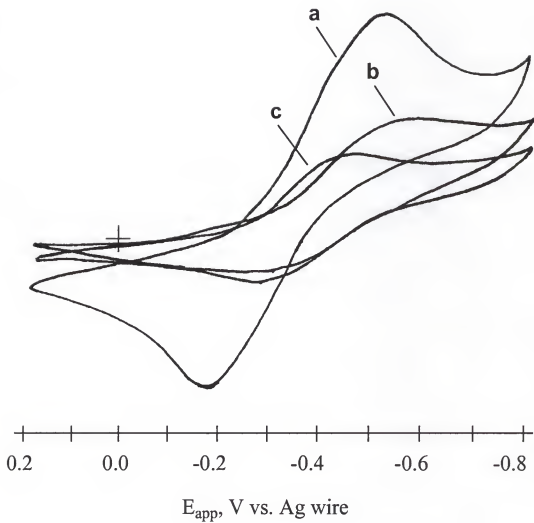


Figure 3.22. Dependence of cyclic voltammetric response of a poly-VBV^{2+} /PETA film on the electrolyte solvent. Conditions: 100 mV·s⁻¹ scan rate, ITO working electrode substrate, Ag wire reference electrode, 0.1 M (n-Bu₄N)PF₆ electrolyte, solvent: (a) 50% acetone/CH₂I₂; (b) 80% benzonitrile/CH₂I₂; (c) nitrobenzene.

of initiating acrylate polymerization. However, the less reactive benzyl radical is known to be a poor initiator for styrene.⁵³ One would expect, then, that the degree of VBV^{2+} polymerization may be quite low compared to that of PETA. Another possible inhibition to copolymer formation is the relative polarities of the two monomers. VBV^{2+} is a quite polar molecule, which may not be very soluble in nonpolar PETA. Upon casting of the monomeric film, there undoubtedly remains a significant amount of DMF (an excellent solvent for VBV^{2+}), which due to its high boiling point may persist even after the lithographic and development procedures. It is quite possible given the above considerations that phase separation occurs within the film both prior to and after photopolymerization, resulting in *poly*- VBV^{2+} -rich domains within a *poly*-PETA matrix.

Experimental details support a conclusion of a phase-separated morphology as well. Recall the comparative cyclic voltammetric response of grating-patterned and flood-irradiated films shown in Figures 3.10 and 3.14. Unpatterned films act to passivate the electrode surface, whereas the lithographic films exhibit satisfactory electrochemical response. The passivation by unpatterned films is almost certainly an effect of severely inhibited ionic mass transfer across the film-solution interface. Only by exposing the inner film regions by way of photopatterning can electrolyte diffusion occur. The implication here is that of a highly crosslinked outer barrier with a degree-of-polymerization gradient established in the inner regions of the film. Further support is offered by the DE modulation experiment shown in Figure 3.15. When a *poly*- VBV^{2+} /PETA grating film is in contact with (n-Bu₄N)PF₆, the electrochemical and DE modulation response diminishes with each reductive cycle, which has been attributed to the loss of electroactive material from the film. Since there is no visible loss of film

integrity after such an experiment, this implies that only the electroactive component, VBV^{2+} , is diffusing from the electrode surface. In order for this to occur, the extent of VBV^{2+} polymerization must be quite low, as must the degree of incorporation into the bulk polymer matrix.

Electrochemistry

Comparison of the cyclic voltammetric data of dissolved VBV^{2+} (Figure 3.9) and a *poly*- VBV^{2+} /PETA film (Figure 3.10) reveals some interesting characteristics. The first obvious feature is the enhancement of the wave corresponding to the VBV^{+0} couple relative to the first reductive wave in Figure 3.10. This phenomenon is not uncommon for surface-confined viologen species, and in fact has been the subject of several studies.^{56,73-75} In each case, these studies have demonstrated a significantly higher (ca. 10-fold or more) electron transfer rate for the viologen $+0$ couple compared to the viologen $2+/+$ couple. The observable effect of this rate difference is an enhanced and sharper surface wave for the second reductive couple as is observed in the *poly*- VBV^{2+} /PETA films.

While the exact source of this rate difference remains uncertain, several plausible suggestions have been put forth. Lewis et al.⁵⁶ and Kepley and Bard⁵⁷ have independently demonstrated (employing concurrent profilometry and ellipsometry techniques, respectively) that film thickness decreases upon reduction, presumably due to reduced like-charge repulsions. This may increase the effective redox site concentration, thereby facilitating electron hopping between neighboring redox sites (recall Figure 1.2). Lewis et al. have demonstrated, however, that this factor cannot fully account for the observed rate difference. Dalton and Murray⁷⁴ have suggested that differences in the

work terms for the electrostatic interactions between the charged viologen sites may play a role as well. He cites several examples in which the electron transfer rate for a highly charged redox couple is higher than that for similar ones of lesser charge.

A second feature of the *poly*-VBV²⁺/PETA cyclic voltammetry is the large peak separation ΔE_p for both redox couples. Interestingly, the second reduction exhibits the larger ΔE_p of the two, in direct contrast with observations by Dalton and Murray.⁷⁴ Increased peak separation implies an inhibited charge transfer diffusion process (small D_{CT}), which at first glance seems to contradict the observed rate enhancement for the second redox couple. Again, the work of Wrighton and Bard mentioned above offers some explanation. The diffusion term accounts not only for the site-site electron hopping, but for ionic mass transport as well. In its fully reduced form, the film is compacted to its highest degree so that the requisite solvent and counterion flux into the film is expected to be significantly more inhibited.

Spectroelectrochemistry

As shown in Figure 3.11, the initially colorless *poly*-VBV²⁺/PETA films exhibit distinct color changes upon sequential reduction. The absorbance spectrum of the singly-reduced film, however, is significantly different from the typical spectrum of a viologen cation radical species in dilute solution, which displays a sharp absorption with vibronic structure at $\lambda_{max} \approx 395$ nm a broad absorption band at ca. 600 nm. It is well known that viologen cation radicals can form dimers or higher order aggregates, both in concentrated solution and in condensed films.^{61,76-79}

This aggregation leads to a blue shift of the two absorption bands and a subtle loss of fine structure, as well as the appearance of a low energy absorbance in the near IR

region. UV-visible-NIR spectra of dilute and concentrated aqueous solutions of methylviologen cation radical in the monomeric and dimeric forms, respectively, are shown in Figure 3.23.⁷⁶ Comparison of these spectra to that of the singly reduced film in Figure 3.11 strongly suggest that dimerization is indeed occurring in the *poly-VBV*²⁺/PETA films.

This observation provides additional support to the assumed film morphology discussed earlier. Since aggregation only occurs in the cation radical state, there is no driving force for molecular orientation and close contact in the dicationic state, in which the film is initially cast and subsequently polymerized. There must, then, be sufficient mobility of viologen sites (implying a low degree of crosslinking) and reasonable initial proximity (suggesting the presence of viologen-rich phase domains) in order to allow this face-on π stacking to occur upon electrochemical reduction.

Diffraction Efficiency Modulation

As would be expected, the dynamics of the DE modulations are closely tied to the electrochemical behavior of the *poly-VBV*²⁺/PETA films. The charge transfer rate differences discussed above become quite obvious when the potential-step data in Figures 3.18-20 are examined. The slow decay of the current response curves shown in part (c) of Figure 3.18 indicates that only partial reduction and subsequent reoxidation of the film occurs during the 30 second potential step intervals. Since the diffraction efficiency modulation relies on this redox process, the diffracted beam intensity is not allowed to plateau during the timeframe of the experiment. Even a fourfold increase of the time increments between switching events to 2 minutes (Figure 3.19) allows for only the first subtle indications that cation radical formation may be nearing completion.

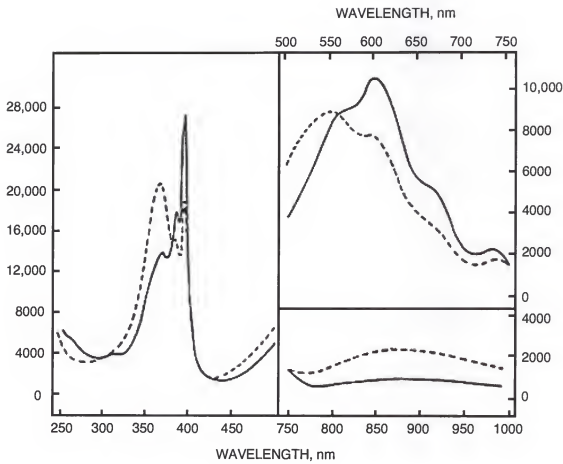


Figure 3.23. Comparative absorbance spectra of viologen cation radical monomer and dimer. The solid and dashed lines correspond to the absorbance of aqueous solutions of methylviologen monomer and dimer, respectively (reproduced from reference 76).

As implied by the cyclic voltammetry data, reduction to VBV^0 is quite facile by comparison. In this case, 2 min potential step intervals allow the electrode current (Figure 3.20, section d) to decay nearly completely to baseline for both the reductive and oxidative processes. This faster electrochemical transformation results in increased DE modulation kinetics. For both the $\text{VBV}^+ \rightarrow \text{VBV}^0$ and $\text{VBV}^0 \rightarrow \text{VBV}^+$ processes, beam intensities establish satisfactorily stable levels much faster than observed for the first redox couple. Close inspection of the diffracted beam intensity profile in part (b), however, reveals that reduction to VBV^0 is slightly faster than the return oxidation to VBV^+ , requiring, on average, approximately 35 s for the former and nearly 50 s for the latter. This may again be a manifestation of the electrochemically induced film shrinkage which was earlier mentioned as the likely cause for the large ΔE_p value for the second reductive couple. Since the film is in its most highly compacted state upon reduction to VBV^0 , ion diffusion into the film accompanying reoxidation is inhibited to a greater degree, and so the corresponding DE modulation is slowed accordingly.

The interesting bidirectional nature of the DE modulation for *poly*- VBV^{2+} /PETA gratings can be qualitatively understood by inspection of the absorptive characteristics at the 633 nm probe wavelength, as shown in Figure 3.11. When the initially unabsorptive film is electrochemically reduced, the optical density at the He-Ne wavelength increases as the 550 nm absorbance band grows in. From an amplitude grating perspective, this results in an increased peak-null absorptive difference between the polymer lines and the bare electrode gaps, giving rise to an increased diffraction efficiency. Upon further reduction to the neutral viologen state, the 550 nm band disappears and is replaced by the low energy tail of the new absorbance at 400 nm. Since the optical density at 633 nm is

reduced, but not entirely eliminated, the diffraction efficiency again drops to near its initial level.

The amplitude grating contribution to this DE modulation can be ascertained by application of equation 1-12, shown again here:

$$DE = \exp \left[\frac{-2.3OD}{\cos \theta} \left[\sinh^2 \frac{\pi \Delta k T}{\lambda \cos \theta} + \sin^2 \frac{\pi \Delta n T}{\lambda \cos \theta} \right] \right] \quad (1-12)$$

Recall that, in Chapter 2, equation 1-12 was manipulated so that the refractive index changes arising from oxidation of the *poly*-RuAAP²⁺/PETA film could be approximated by matching the calculated ΔDE values with those obtained experimentally. This was accomplished by neglecting the second term of the equation (since $\Delta OD = 0$, $\Delta k = 0$), and incrementing the only unknown variable for the oxidized films, Δn , to give a range of predicted ΔDE values.

In the present case, we can apply a similar strategy to calculate how a change in Δk will effect the diffraction efficiency of *poly*-VBV²⁺/PETA films by neglecting (for the time being) the third term, which describes the phase grating effects on diffraction efficiency. Using values of $OD = 0$, $\theta = 0$, $T = 400$ nm, $\lambda = 633$ nm, and Δk incremented from 0.0 to 0.20, a range of predicted ΔDE values was obtained, which is shown as the solid curve in Figure 3.24. The horizontal dotted lines in the figure represent the range of experimental $\% \Delta DE$ values from Tables 3.4 and 3.5 ($\Delta DE = 20-75\%$). Note that at the experimentally observed ΔOD of 0.07 (from Figure 3.11), a ΔDE value of only 0.9% is predicted.

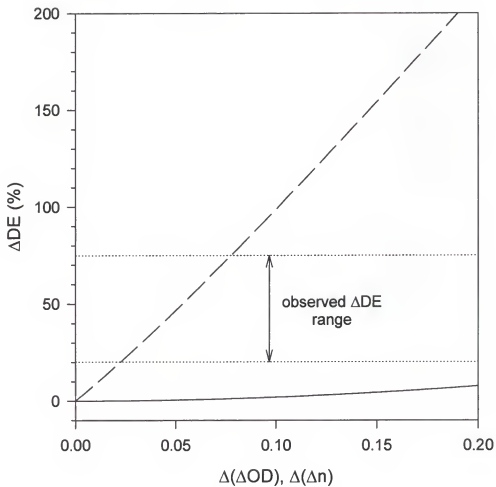


Figure 3.24. Comparative effects of refractive index and optical density changes on diffraction efficiency modulation for a *poly*-VBV²⁺/PETA film.

This result demonstrates that while amplitude grating effects can be called on to qualitatively explain the bidirectional DE modulation, it clearly cannot quantitatively account for these effects. The *poly*-VBV²⁺/PETA films must, then, behave as mixed gratings with substantial phase grating contributions. Since the amplitude grating contribution is so small (<1%), it can be neglected so that the phase grating contribution can be calculated exactly as described in Chapter 2 and above. Using values of OD = 0, θ = 0, T = 400 nm, λ = 633 nm, Δk = 0, an initial Δn = 0.217 ($n_{\text{film}} = 1.564$, $n_{\text{gap}} = 1.347$), and incrementing Δn by 0.002, the dashed line in Figure 3.24 was obtained. From this curve it is clear that for these thick films, the refractive index term dominates the experimentally observed diffraction efficiency modulations.

Experimental

N,N-dimethylformamide was purified by vacuum distillation and stored over molecular sieves. Acetonitrile for electrochemical experiments was distilled over calcium hydride. 4,4'-dipyridyl was purified by recrystallization from cyclohexane. Tetrabutylammonium hexafluorophosphate was recrystallized twice from ethanol/water. All other solvents, reagents, and electrolyte salts used are reagent grade and used as received without further purification, unless otherwise noted. ¹H and ¹³C NMR spectra were recorded on a General Electric QE-300 spectrometer. Elemental analyses were performed by the University of Florida Department of Chemistry Analytical Services. An Integrated Technologies P-6000 spin coater was used for spin casting of films prior to lithographic exposure. Photopolymer film thickness was measured using a Sloan Dektak profilometer with a 12 μm stylus tip. Optical transmission microscope images were obtained using a Nikon F4s 35 mm SLR camera attached to a Nikon Optiphot-POL

microscope. Scanning electron microscope images were obtained using a JEOL JSM-6400 SEM at the University of Florida Major Analytical Instrumentation Center.

Synthesis of Vinylbenzylviologen (VBV²⁺)

4,4'-dipyridyl (2.0 g, 12.8 mmol, Aldrich) was dissolved in 50 mL of absolute ethanol, and vinylbenzyl chloride (7.82 g, 51.2 mmol, Aldrich) was added with stirring. The solution was refluxed under a nitrogen atmosphere for 20 hours, after which most of the solvent was removed by rotary evaporation. Upon addition of acetone, a yellow solid was precipitated which was collected by filtration on a medium-porosity glass frit, washed with acetone, and dried under vacuum to yield 3.9 g (66%) of the dichloride salt.

Counterion metathesis to the bis-hexafluorophosphate salt was accomplished by dissolving a portion of the chloride salt in water and an approximately equal amount of acetone. A solution of ammonium hexafluorophosphate (4 equivalents) in water was added and the acetone was removed slowly by rotary evaporation, inducing precipitation of the insoluble hexafluorophosphate salt. The solid was collected by filtration, washed with water, and dried under vacuum, affording the yellow solid in near quantitative yield. ¹³CNMR spectra are complicated due to the mixture of isomers present: the vinylbenzyl chloride used in the synthesis is a mixture of 70% *meta* and 30% *para* isomers, giving three possible structural isomers of the diquaternized product (49% *meta/meta*, 42% *meta/para*, 9% *para/para*). NMR of PF₆⁻ salt (¹H, CD₃CN): 85.35 (d, 2H), 5.80 (s, 4H), 5.88 (d, 2H), 7.39-7.58 (m, 8H), 8.37 (d, 4H), 8.98 (d, 4H); (¹³C, CD₃CN): δ 64.7, 115.2, 115.5, 127.0, 127.1, 127.4, 127.7, 128.5, 128.6, 129.7, 129.8, 135.7, 135.8, 145.5. Anal. Calcd. for C₂₈H₂₆N₂P₂F₁₂: C, 49.42; H, 3.85; N, 4.12. Found: C, 49.75; H, 3.71; N, 3.90.

Electrochemical/Optical Experiments

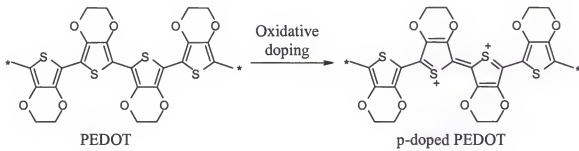
Indium-tin oxide (ITO) glass optically transparent electrodes (Delta Technologies, Stillwater, MN) are used as the substrate for photopolymer film fabrication. Cyclic voltammograms are recorded using a Bioanalytical Systems CV-27 voltammograph in conjunction with an ADInstruments MacLab/4e analog-to-digital converter and electrochemical software. All reported potentials are relative to a Ag wire quasi-reference electrode ($\approx +0.05$ V vs. SSCE in 0.1 M (n-Bu₄N)PF₆/CH₃CN) which is employed due to space constraints in the electrochemical cell used for the optical studies. The electrolyte solutions used for the experiments are 0.1 M (n-Bu₄N)PF₆/CH₃CN (dissolved monomer), 0.1 M (n-Bu₄N)PF₆/DMF (photopolymer film), and (n-Bu₄N)Cl/DMF (photopolymer film). All electrolyte solutions were degassed by bubbling with dry nitrogen before conducting electrochemical experiments. UV-visible absorbance is measured using a Hewlett-Packard 8452A diode-array spectrophotometer. Spectroelectrochemical experiments are performed using the HP 8452A in conjunction with the BAS CV-27 voltammograph. Instrumentation used for optical diffraction studies is described in the Appendix.

CHAPTER 4
TRANSMISSION GRATINGS BASED ON ELECTRONICALLY
CONDUCTIVE POLYTHIOPHENE

Introduction

Poly(alkylthiophene)s have emerged in recent years as important materials for a broad range of device applications, including nonlinear optics,⁸⁰ photodetectors,⁸¹ and electrochromic,⁸²⁻⁸⁴ solvatochromic,⁸⁵ and ionochromic devices.⁸⁶ These materials can be chemically or electrochemically doped (both p- and n-doping), which causes them to be electronically conductive. There have been several reports in the literature regarding lithographic patterning of polythiophenes to make practical use of their optoelectrochemical properties in waveguides, or for preparing conductive polymer wires. One of these strategies, reported by Lowe and Holdcroft,⁸⁷ is strikingly similar to the methods described in the previous two chapters. As depicted in Figure 4.1, a preformed polythiophene with methacrylate functionality is spin-cast onto a solid substrate, either quartz or silicon. Irradiation of the film through a lithographic mask initiates free-radical crosslinking of the polymer chains through the pendant methacrylate groups. Subsequent development of the image is accomplished by immersion in chloroform, which selectively rinses away the uncrosslinked material by virtue of the diminished solubility of the irradiated film regions. The resulting undoped (nonconducting) film pattern is then chemically doped by immersion in a AuCl_3 solution, giving a lithographic conducting polymer image.

For the present study, we chose to adopt a modified version of Lowe and Holdcroft's technique by employing an acrylate-substituted analog of *poly*(3,4-ethylenedioxythiophene) (PEDOT).⁴⁹ These materials possess several beneficial properties, which fit nicely into the DE modulation studies. The use of a preformed polymer eliminates many of the uncertainties regarding the physical and chemical nature of the material, such as the polymer backbone structure and the degree of polymerization. The need for crosslinking additives (PETA), which dilute the film and have questionable effects on the electrochemical properties of the material, is eliminated by this approach. Distinct color changes accompany electrochemical doping of PEDOT and related conjugated polymers. And finally, p-doping of PEDOT proceeds under low anodic applied voltage.⁸⁸⁻⁹² Low voltage means that less electrochemical stress is applied, which can favorably affect the lifetime and stability of these materials, and is also beneficial for rapid electrochemical switching applications.



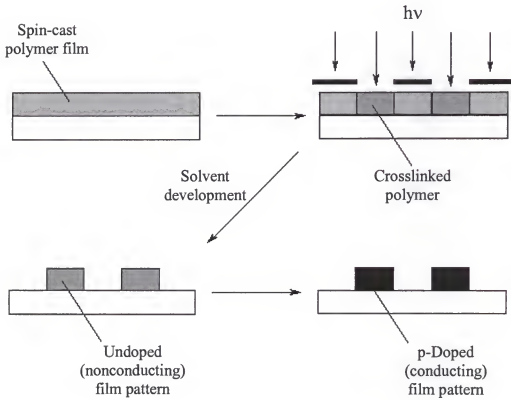
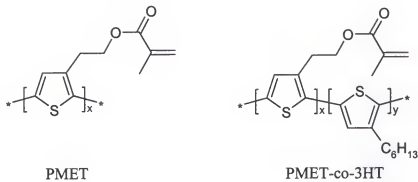


Figure 4.1. Lowe and Holdcroft's photolithographic process for fabrication of conductive polymer images comprised of PMET and PMET-co-3HT.

Results

Synthesis

Modified literature procedures were employed for the synthesis of the functionalized EDOT analogs.^{82,88} As shown in Figure 4.2, the reaction with epibromohydrin (step iv) results in the formation of two structural isomers having either a six- or a seven-membered fused heterocyclic ring (structures 4-3a and 4-3b). Separation of these two isomers by chemical and/or chromatographic means may be possible, but no rigorous effort was made to do so. It is assumed that this isomeric mixture prevails throughout the remaining synthetic scheme, so the monomers and polymers prepared therefrom will be referred to as functionalized PMDOTs (3,4-polymethylenedioxy-thiophene)s and *poly*-PMDOTs, respectively. The final step in the synthetic scheme is functionalization of the hydroxy-PMDOT monomers by reaction with either acryloyl chloride to yield PMDOT-acr for crosslinking functionality, or decanoyl chloride to yield PMDOT-dec for solubility enhancement.

Polymerization proceeds under typical ferric chloride conditions as described in the literature.^{93,94} Two types of polymer were prepared (Figure 4.3). The (pseudo-) homopolymer *poly*-PMDOT-acr was prepared from the acrylate monomers only, to provide a high degree of crosslinking upon eventual photopatterning. This strategy resulted in a very low yield of soluble material upon isolation. The greater portion of the material obtained was insoluble in all common solvents, either due to a high degree of polymerization, or a side reaction resulting in crosslinking via the acrylate side groups, possibly brought on by exposure to ambient light. Preparation of the copolymer poly-PMDOT-acr/dec, with monomer feed ratios of 1:2 to 2:3 PMDOT-acr:PMDOT-dec,

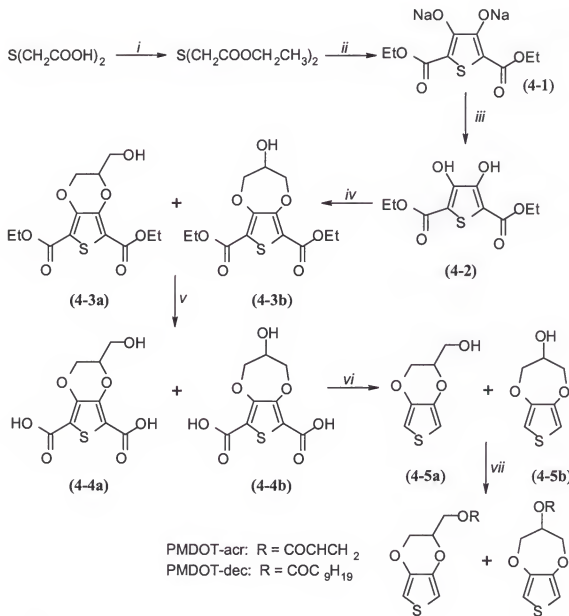


Figure 4.2. Synthesis of substituted PMDOT monomers. (i) EtOH , conc. H_2SO_4 , reflux 24 hr; (ii) NaOEt/EtOH , diethyl oxalate, reflux 1.5 hr; (iii) conc. HCl ; (iv) K_2CO_3 , epibromohydrin; (v) 10% NaOH , reflux 1 hr; (vi) quinoline, barium-promoted copper chromite, reflux 45 min; (vii) triethylamine, R-Cl , 24 hr.

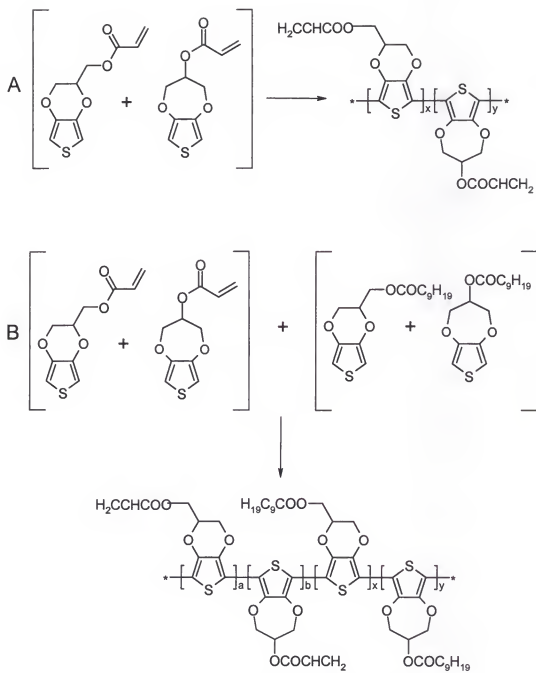


Figure 4.3. Synthesis of *poly*-PMDOT-acr (A) and *poly*-PMDOT-acr/dec. (B). General conditions and monomer feed ratios are discussed in the text, and specific reaction conditions are detailed in the Experimental section.

resulted in satisfactory yields of processable material, presumably due to the high degree of solubility-enhancing alkyl group substitution. Thirty three to 40% acrylate functionality in these materials has proven to be more than sufficient for the lithographic methodology, as even a small degree of crosslinking will substantially affect the solubility of the polymer film.

It was observed that if, upon workup of these polymers, the solvent was completely stripped off by rotary/vacuum evaporation, very little, if any, of the resulting solid could be redissolved in any available organic solvent. For this reason, the polymers were kept dissolved in chloroform at an approximately known concentration (ca. 30 $\text{mg}\cdot\text{mL}^{-1}$) and stored tightly sealed.

Photolithography

In addition to the polymer identity, a second modification of Lowe and Holdcroft's lithographic strategy was made. The authors attribute photoinduced crosslinking to initiation either by residual ferric salts which generate radicals upon irradiation, or singlet oxygen attack on the methacrylate double bond to yield hydroperoxide, followed by dissociation into free radicals.⁸⁷ Not wishing to rely on initiation by uncertain sources, we again employed the services of benzoin ethyl ether. The spin-casting mixture for film formation was prepared by addition of 10 μL of a 21 $\text{mg}\cdot\text{mL}^{-1}$ BEE stock solution to 20 μL of a (nominally) 30 $\text{mg}\cdot\text{mL}^{-1}$ *poly*-PMDOT / chloroform solution (3:1 PMDOT:BEE by weight). Due to the low concentration and high volatility of the solvent, films were prepared by dropwise addition of 10-15 μL of this mixture onto a substrate spinning at 3000-4000 rpm. As a consequence of this fabrication procedure, although the intensity of the film color implied otherwise,

extremely thin polymer films were obtained. Edge-on scanning electron microscopy of freeze-fractured polymer images failed to show film profiles, suggesting a thickness under 100 nm. Face-on optical microscopy, however, provides sufficient contrast to obtain well-defined photographic images, as shown in Figure 4.4. Despite the prevalent particulate matter on the substrates, reproduction of mask features as small 2.2 μm (top photo, group 7, element 6) is excellent.

Film Characterization

Electrochemistry. For preparation of polythiophene chemically modified electrodes, an electropolymerization technique is commonly employed with good results.⁹⁴ As a basis for comparison of the electrochemical properties of the *poly*-PMDOT lithographically patterned films, PMDOT-acr was anodically deposited on an ITO electrode substrate (Figure 4.5). Oxidative cycling of the applied electrode potential between -1.0 and 1.8 V in contact with a 5 mM solution of PMDOT-acr in 0.1 M tetra-n-butylammonium perchlorate / acetonitrile resulted in the growth of an electropolymerized *poly*-PMDOT-acr film in the electrode region in contact with the monomer solution (0.0396 cm^2). The film and electrochemical cell were rinsed with fresh acetonitrile several times, and the cell was filled with monomer-free electrolyte solution. The resulting CV scan is shown in Figure 4.6. Although the electrochemical wave is quite broad, the half-wave potential can be estimated at 0.35 V vs. Ag wire. This value falls slightly outside the range of oxidation potentials reported in the literature for other EDOT-based films, in which p-doping often occurs between 0.0 and -0.3 V, although these values are highly dependent on several factors, including alkyl functionalization, electrolyte composition, film deposition conditions, and film thickness.

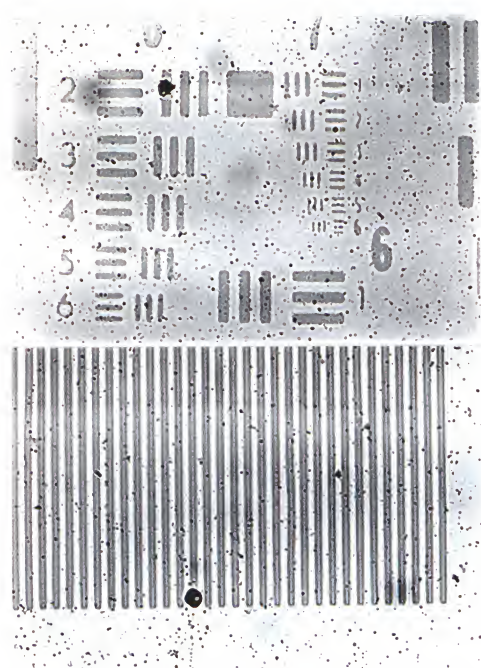


Figure 4.4. Optical transmission microscope images of *poly-PMDOT-acr/dec* lithographic films. Top: photopolymer image fabricated using the USAF 1957 lithographic mask showing groups 6 and 7 of the test pattern. Bottom: grating-patterned image having 5 μ m line- and gapwidths.

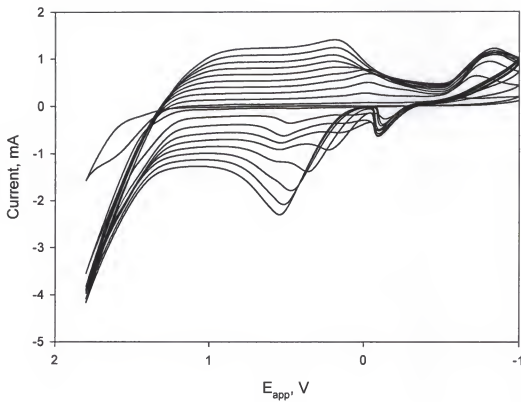


Figure 4.5. Electrochemical polymerization of PMDOT-acr. Conditions: ITO working electrode substrate, 0.0396 cm^2 active surface area, Pt wire auxiliary electrode, Ag wire quasi-reference electrode, 5 mM PMDOT-acr in 0.1 M (n-Bu₄N)ClO₄ / acetonitrile, -1.0 to 1.8 V, $100\text{ mV}\text{s}^{-1}$, 10 cycles.

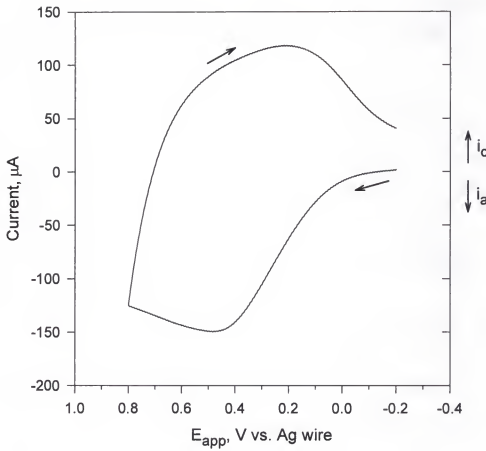


Figure 4.6. Cyclic voltammetry of an electropolymerized *poly*-PMDOT-acr film. Conditions: 0.1 M (n-Bu₄N)ClO₄ / acetonitrile electrolyte, ITO working electrode substrate, Ag wire quasi-reference electrode, 100 mV·s⁻¹ scan rate.

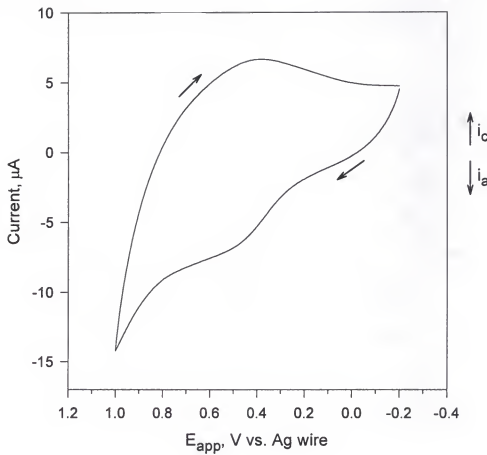


Figure 4.7. Cyclic voltammetry of a *poly*-PMDOT-acr/dec grating-patterned film. Conditions: 0.1 M (n-Bu₄N)ClO₄ / acetonitrile electrolyte, ITO working electrode substrate, Ag wire quasi-reference electrode, 100 mV·s⁻¹ scan rate.

The cyclic voltammetry of a grating-patterned *poly*-PMDOT-acr/dec film is shown in Figure 4.7. Continuous scanning through this potential region demonstrates that these films are quite robust, showing no diminishment of electrochemical activity. As observed for the electropolymerized film, the oxidative wave is rather broad and ill-defined, but a half-wave potential of approximately 0.5 V can be ascertained. This positive shift in oxidation potential is not surprising considering the comparative nature of the two polymer films. Since the compositions of the two films are not the same, a slightly different oxidation/doping potential is to be expected. It is also likely that there is a significant difference in the nature of the film-electrode interface due to the different film formation processes. By virtue of its means of growth, the electropolymerized film should exhibit a more intimate contact with the electrode surface, as well as optimized electron transfer pathways into the more remote regions of the film.

Spectroelectrochemistry. As demonstrated in the previous two chapters, the spectroelectrochemical response of these films is of particular interest. Shown in Figure 4.8 are UV-visible absorbance spectra at incrementally stepped applied potentials progressing through the oxidative doping region. As the potential is stepped from -0.2 V through 0.9 V, bleaching of the absorbance centered at approximately 520 nm is observed. Concomitant with this bleaching is the growth of a new absorbance band in the far visible-near IR region. This low-energy absorbance is well documented in the literature, and it attributed to the formation of two bipolaronic bands,^{95,96} typically situated at approximately 1.5 eV (1240 nm) and 0.5 eV (2500 nm). The vertical line shown in the figure corresponds to the wavelength of the He-Ne laser, which is instructive for the interpretation of the diffraction efficiency modulation experiments.

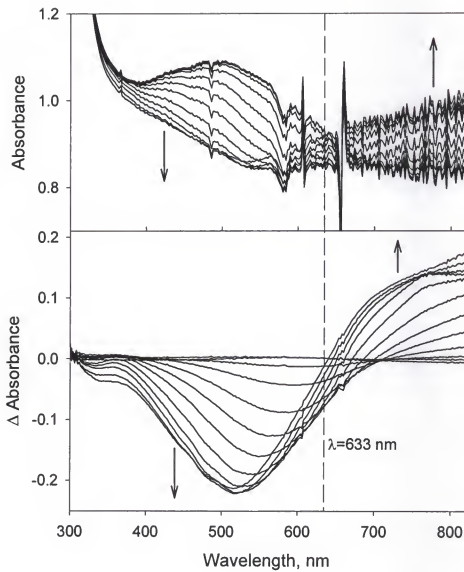


Figure 4.8. Spectroelectrochemical response of a poly-PMDOT-acr/dec grating-patterned film. Shown spectra were measured in 100 mV increments from -0.2 to 0.9 V vs. Ag wire quasi-reference electrode. Top: incremental absorbance spectra. Bottom: delta absorbance spectra calculated by subtraction of the film absorbance at 0.3 V. The dashed vertical line indicates the wavelength of the He-Ne laser probe (633 nm) used in the diffraction studies.

Diffraction Experiments

Cyclic potential experiments. As anticipated, grating-patterned *poly*-PMDOT lithographic films behave as optical diffraction gratings. Due to the substantially diminished thickness of these films relative to those described in the previous chapters, the initial diffraction efficiency, DE_0 , is quite low. Typically, the intensity of a first-order diffracted beam is <0.5% relative to that of the transmitted beam when the film is placed in contact with an electrolyte solution, and only two to three orders of diffraction can be observed. Application of an electrochemical signal (oxidative doping), however, results in a high degree of relative DE modulation. Figure 4.9 shows the results of a typical swept-potential DE modulation experiment. As the electrode potential is scanned from –0.1 to 0.9 V, the oxidation of the polymer results in an 80% decrease of the first-order diffracted beam intensity. Upon scan reversal, the beam intensity rises as the film is dedoped until it reaches a level of approximately 90% initial intensity before the subsequent potential scan commences. Repeated potential cycling demonstrates excellent reproducibility and stability of the DE modulation response. Collected in Table 4.1 is swept-potential experimental data for two *poly*-PMDOT-acr/dec gratings at several scan rates.

Stepped potential experiments. Given the encouraging results from the triangular wave voltammetry experiments, analogous potential-step DE modulation was investigated under several sets of experimental conditions. Shown in Figure 4.10 are the results of stepwise DE modulation experiments for *poly*-PMDOT-acr/dec gratings in contact with perchlorate, hexafluorophosphate, and chloride-containing electrolyte solutions. Part (a) of the figure shows the square-wave applied potential with 15 s step

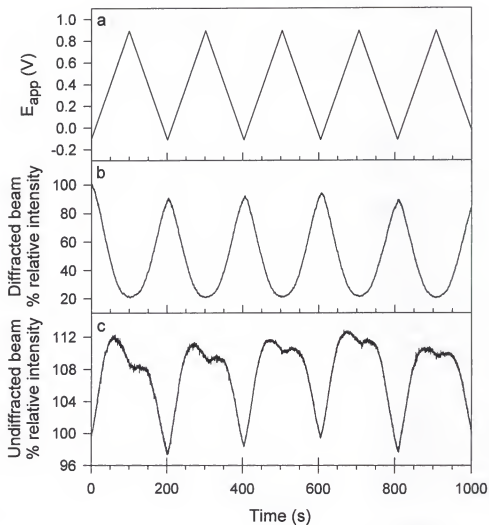


Figure 4.9. Swept-potential electrochemical modulation of the diffraction efficiency of a *poly*-PMDOT-acr/dec grating-patterned film. Conditions: 0.1 M (n-Bu₄N)ClO₄ / acetonitrile electrolyte solution, -0.1 to 0.9 V vs. Ag wire quasi-reference electrode, ITO working electrode substrate, 10 mV·s⁻¹ scan rate. (a) Applied potential scanned through the doping/dedoping region. (b) Relative intensity of a first-order diffracted beam (initial diffraction efficiency $DE_0=0.34\%$). (c) Relative intensity of the zero-order undiffracted beam.

Table 4.1. Collected swept-potential diffraction efficiency modulation data for two grating-patterned *poly*-EDOT-acr/dec films.

Exp. #	Scan rate ^a (mV·s ⁻¹)	DE ₀ ^b (%)	Δdiff ^c (%)	Δundiff ^d (%)
1	10	0.34	80	14
	25	0.34	77	13
	50	0.34	75	12
	100	0.34	74	12
2	10	0.27	72	14
	25	0.27	71	13
	50	0.27	70	13
	100	0.27	67	12
Ave.			73	13
Std. Dev.			4	1

a Conditions: 0.1 M (n-Bu₄N)ClO₄ / acetonitrile electrolyte, -0.1 to 0.9 V vs. Ag wire.

b Initial ratio of a first-order diffracted beam intensity to the zero-order undiffracted beam intensity prior to electrochemical cycling.

c Relative change in the intensity of a first-order diffracted beam upon electrochemical cycling.

d Relative change in the intensity of the zero-order undiffracted beam upon electrochemical cycling.

increments between 0.0 and 0.8 V. Parts (b), (c), and (d) show the temporal response of the diffracted beam intensity as a function of the anionic electrolyte constituent. In all three cases, oxidative doping leads to a nearly instantaneous drop in diffracted beam intensity to 30-35% of the initial level. Reductive dedoping at 0.0 V in the presence of perchlorate and hexafluorophosphate salts results in a slightly slower recovery of the beam intensity, requiring approximately 5 s or less. In the case of the chloride electrolyte, however, the recovery is significantly more sluggish, and is incomplete within the 15 s lag time before the subsequent doping cycle commences. Another interesting feature is the unusual spikes encountered at the beginning of each doping cycle shown in part (d). As will be discussed further, these are likely artifacts arising from mass-transfer dynamics between the film and the bathing electrolyte solution. Data from multiple experiments under these conditions, along with one experiment in which propylene carbonate is examined as the electrolyte solvent, is collected in Table 4.2.

As the stability of these films to continuous electrochemical cycling would suggest, the DE modulation characteristics are quite stable to long-term potential cycling. Shown in Figure 4.11 are the results of an experiment in which a *poly*-PMDOT-acr/dec grating was subjected to over 500 doping-dedoping cycles. The temporal diffracted beam intensity profiles during cycles 1 (a), 101 (b), 251 (c), and 501 (d) are overlaid for comparison. During the course of the experiment, Δ DE values decreased somewhat from an initial value of 73% for the first cycle to 64% five hundred switching events later. The rate of recovery upon dedoping at 0.0 V, as well as the intensity level attained, also exhibit some diminishment over the course of the experiment.

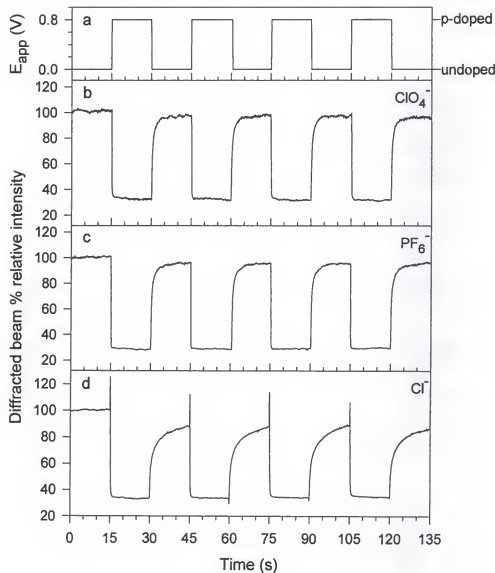


Figure 4.10. Electrolyte dependent potential-step electrochemical modulation of the diffraction efficiencies of *poly*-PMDOT-acr/dec grating-patterned films. Conditions: ITO working electrode substrate, 0.0 to 0.8 V vs. Ag wire quasi-reference electrode, 15 s step time. (a) Applied potential stepped between doping and dedoping potentials. (b-d) Relative intensities of a first order diffracted beam from a grating-patterned film in contact with 0.1 M acetonitrile solutions of $(n\text{-Bu}_4\text{N})\text{ClO}_4$, $(n\text{-Bu}_4\text{N})\text{PF}_6$, and $(n\text{-Bu}_4\text{N})\text{Cl}$ electrolyte salts, respectively.

Table 4.2. Collected stepped-potential diffraction efficiency modulation data for grating-patterned *poly*-EDOT-acr/dec films.

Exp. #	Electrolyte ^a (0.1 M)	Step time ^b (s)	DE ₀ ^c (%)	Δdiff ^d (%)	Δundiff ^e (%)
1	TBACl/AN	10	0.49	43 (63)	15
2	TBACl/AN	15	0.25	55 (67)	15
3	TBACl/AN	20	0.56	52 (57)	12
4	TBAH/AN	10	0.25	73	11
5	TBAH/AN	15	0.41	56 (64)	13
6	TBAH/AN	15	0.32	70	7
7	TBAH/AN	15	0.34	74	4
8	TBAP/AN	10	0.35	72	8
9	TBAP/AN	10	0.34	50	11
10	TBAP/AN	15	0.21	50	22
11	TBAP/AN	15	0.10	68	9
12	TBAP/AN	15	0.15	74	8
13	TBAP/AN	15	0.13	75	8
14	TBAP/AN	15	0.28	76	8
15	TBAP/AN	20	0.35	74	7
16	TBAP/PC	15	0.09	50 (60)	9

a TBACl = (n-Bu₄N)Cl; TBAH = (n-Bu₄N)PF₆; TBAP = (n-Bu₄N)ClO₄; AN = acetonitrile; PC = propylene carbonate.

b 0.0 to 0.8 V vs. Ag wire reference.

c Initial ratio of a first-order diffracted beam intensity to the zero-order undiffracted beam intensity prior to electrochemical switching.

d Reproducible relative change in the intensity of a first-order diffracted beam upon electrochemical switching. Values in parentheses denote the change during the first potential step for experiments in which the intensity does not fully recover to 100% upon dedoping at 0.0 V.

e Relative change in the intensity of the zero-order undiffracted beam upon electrochemical switching.

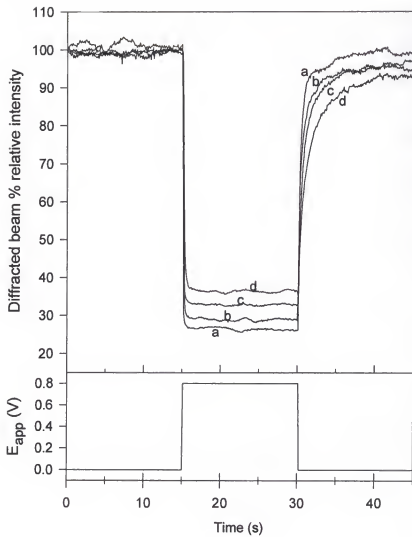


Figure 4.11. Stability of a *poly*-PMDOT-acr/dec film to repeated double potential-step cycling. Conditions: 0.1 M (n-Bu₄N)ClO₄ / acetonitrile electrolyte solution, grating-patterned *poly*-PMDOT-acr/dec film on an ITO working electrode substrate, Ag wire quasi-reference electrode, 0.0 to 0.8 V (15 s intervals). Top: First order diffracted beam intensity profiles upon subjection to multiple potential-switching events. Shown are cycles (a) 1, (b) 101, (c) 251, and (d) 501. Bottom: Square wave potential cycle applied to the working electrode.

Bidirectional modulation. In addition to oxidative doping, polythiophenes can also be reductively doped (n-doping). With the intent of observing bidirectional DE modulation such as that described in Chapter 3, a *poly*-PMDOT-acr/dec grating was subjected to several cycles of alternate electrochemical n- and p-doping. The results shown in Figure 4.12 demonstrate that bidirectional DE modulation does indeed occur, with an approximate 50% increase of diffracted beam intensity during the initial n-doping cycle. The dynamics of DE modulation from a reductive electrochemical signal appear initially to be quite good, although film integrity under these conditions rapidly deteriorates. Cathodic doping of the material appears to compromise the polymer integrity, as has been noted elsewhere, and may be attributed to the presence of trace amounts of water and/or oxygen. The irreversibility of the cathodic voltammetric wave shown in Figure 4.13 lends support to this conclusion.

Discussion

Film Characterization.

Both the cyclic voltammetric wave and the UV-visible absorption spectra of *poly*-PMDOT-acr/dec appear quite broad in nature, implying multiple local environments within the material. Examination of the spectroelectrochemical data in Figure 4.8 reveals that λ_{max} of the bleaching absorbance band blue-shifts at higher applied potentials, and no single isosbestic point is maintained as the lower energy absorbance band grows in. All of these characteristics are attributable to the complex nature of the polymer. The high polydispersity index of the polymers prepared by ferric chloride polymerization indicates that there is a range of intrinsic conjugated backbone chainlengths. There are also multiple local environments within the bulk of the film imposed by steric factors. This

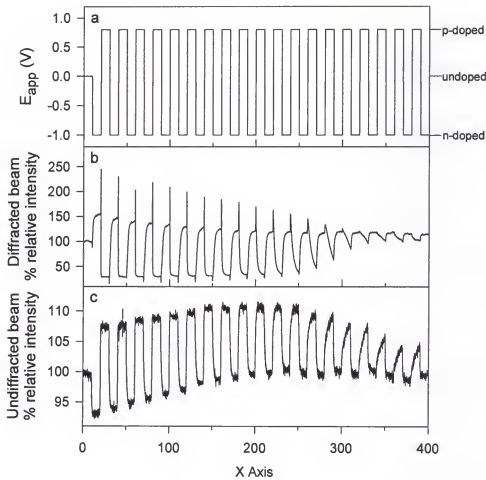


Figure 4.12. Bipolar potential-step electrochemical modulation of the diffraction efficiency of a poly-PMDOT-acr/dec grating-patterned film. Conditions: 0.1 M (n-Bu₄N)ClO₄ / acetonitrile electrolyte, ITO working electrode substrate, Ag wire quasi-reference electrode, 10 s potential step times. (a) Applied potential stepped between n-doping (-1.0 V) and p-doping (+0.8 V) potentials. (b) Relative intensity of a first-order diffracted beam ($DE_0 = 0.1\%$). (c) Relative intensity of the zero-order undiffracted beam.

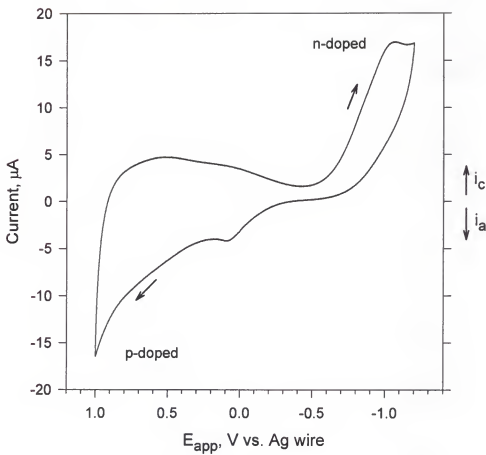


Figure 4.13. Cyclic voltammetric bipolar doping/dedoping of a *poly*-PMDOT-acr/dec grating-patterned film. Conditions: 0.1 M (n-Bu₄N)ClO₄ / acetonitrile electrolyte, Ag wire quasi-reference electrode, ITO working electrode substrate, -1.3 to 1.0 V, 10 mV·s⁻¹ scan rate.

causes variations in the coplanarity between adjacent rings, and thus a range of effective conjugation lengths, L_{eff} , along the same backbone structure. In the previous two chapters, the polymers had discrete redox centers (albeit with multiple local environments of their own). This is not the case for a conjugated polymer, in which the redox sites can be anywhere from one to several repeat units, depending largely on these steric-induced variations. In conjugated polymers, λ_{max} is primarily a function of L_{eff} : long conjugation length corresponds to low energy, and vice versa. In the spectroelectrochemical data it appears, then, that long L_{eff} sites are bleached first at the lower potentials. This is reasonable, since conductivity is higher for longer L_{eff} , so these sites are the ones experiencing oxidative doping at the lower potentials. As the bulk conductivity increases, the doping of the shorter L_{eff} sites is facilitated, causing the subsequent blue shift in the bleaching spectra. This same trend can be observed in the growth of the new low-energy absorbance band attributed to the p-doped polymer. Just as the lower energy sites are doped first (the lower-energy portion of the absorbance band is bleached), the new absorbance band appears first in the near IR region. At more positive potentials, the higher energy (short L_{eff}) bleaching gives rise to the growth of the new absorbance band reaching into the visible region.

Diffraction Experiments.

Cyclic DE modulation. The improved electrochemical dynamics of a conjugated polymer, relative to that of the redox polymers described in the previous chapters, carry over to the DE modulation experiments employing *poly*-PMDOT shown in Figure 4.9. The beam intensity modulations can be understood by examination of the spectroelectrochemical data shown in Figure 4.8. Looking first at the zero-order

transmitted beam profile, the effect of the decreasing-then-increasing absorbance at 633 nm is evident: as the absorbance at the probe wavelength initially decreases, the transmitted beam intensity initially rises. This continues until the growth of the low energy absorbance band starts to approach 633 nm, at which point the beam intensity drops slightly. Re-reduction of the film upon scan reversal leads to the reversal of these absorptive dynamics, creating the dip shown at the midpoint of the diffracted beam intensity profile.

Perhaps remarkably, the diffracted beam intensity response appears much 'cleaner'. In this case, as the film is p-doped, the diffracted beam intensity falls smoothly as the absorbance band between 500 and 600 nm is bleached. Given the proximity of the He-Ne wavelength to this absorbance band transition, it is likely that the film is behaving as a combination amplitude/phase grating: there is significant variation in the absorbance at 633 nm, coupled with a strong effect contributed by the refractive index factor. The contribution of Δn to the diffractive response is significant, since the profile of the DE modulation is smooth and continuous, unlike that of the transmitted beam. At some point during the doping process, the absorbance at 633 nm begins to rise near that of the undoped film, but the DE continues to fall nonetheless. This phenomenon is due to the fact that although the magnitude of Δn is the same on both sides of an absorbance band, the refractive index changes (positive or negative) are in *opposite directions*.⁹⁷ For example, the appearance of an absorption gives rise to an increased refractive index to the red of its λ_{max} , while the refractive index is diminished to the same degree on the blue side. By the same token, Δn is negative on the low energy side of a bleaching band, and positive on the high energy side. The DE profile of the diffracted beam is

understandable, then, because the negative Δn contribution from the new low energy absorbance band that is appearing (with its λ_{\max} to the red of 633 nm) reinforces the negative Δn from the bleaching band (whose $\lambda_{\max} < 633$ nm), thereby smoothing over the bidirectional amplitude grating contribution.

Square-wave DE modulation. By application of a stepped potential profile, the complex absorbance and refractive index contributions are essentially masked. Quickly stepping the applied potential into the doping region allows the various influences to rapidly equilibrate and establish a single diffraction efficiency level. This is demonstrated in Figure 4.10 by the extremely fast DE modulation resulting from oxidative doping of the film. In all cases shown in the figure, the dynamic response of the diffracted beam intensity is faster for the doping reaction than for the dedoping. This can be understood by considering the electrochemical processes occurring both at the film-electrode interface and within the bulk of the material. As the film is doped, the conductivity at the electrode interface is enabled, which facilitates further doping in the more remote regions of the film via inter- and intrachain electron transport. Conversely, as the polymer adjacent to the electrode surface is dedoped, conductivity is diminished, thereby eliminating some of the channels for electron transport. Under these conditions, the primary mode of electron transport between the electrode and the inner film regions may become interchain in nature, as intrachain transport along the polymer backbone is inhibited. Since interchain electron hopping is strongly distance dependent, the limiting factor in the dedoping kinetics may be the lattice mobility within the film.

It should be noted that Sotzing and Reynolds⁹⁸ have reported the opposite doping-dedoping dynamics of those described above. Electropolymerized PEDOT films,

when employed as electrochromic materials, display faster *dedoping* kinetics when the transmittance at ~600 nm is monitored as the diagnostic probe. Their rationale for explaining this observation is that reduction (dedoping) can occur at any point in the film due to the high conductivity of the doped film. Doping, on the other hand, proceeds as a conductivity 'front' which must proceed outwards from the electrode surface, which he believes to be an inherently slower process. Their explanation and that offered here are at odds with each other, and perhaps once again the comparative nature of electropolymerized versus spin-cast films comes into play. A second, possibly significant difference is that of film thickness and its effect on counterion diffusion. Sotzing and Reynolds' results are obtained using *unpatterned* films which are ca. 300 nm thick, a value which is probably at least five times that of our lithographic images. In order for the 'conductive front' to travel outward from the electrode surface, ionic mass transport can only progress along one vector (normal to the plane of the electrode) through the entire thickness of the film. Three-dimensional patterning, however, allows for additional lateral ion diffusion through inner film regions, facilitating the (otherwise inherently slower) process.

Electrolyte effects. It appears from the data in Figure 4.10 that the electrolyte plays a significant role in this process. In the presence of perchlorate or hexafluorophosphate electrolyte anions, beam intensity recovery upon film dedoping is quite similar. However, in contact with an electrolyte solution containing chloride the dedoping of the bulk material is quite inhibited. This may be attributed to a mass transport effect. As the film is reduced, there must be an egress of anions from the film in order to maintain charge neutrality. Chloride ion, due to its small size, may be

expelled at a much higher rate than either perchlorate or hexafluorophosphate. This results in conductive channels from the electrode surface being eliminated much more quickly, so that the lattice mobility requirement for interchain hopping can become quite pronounced.

The unusual diffracted beam intensity spikes that appear in part (d) of Figure 4.10 may also be attributed to mass transport dynamics. In this instance, though, anion transport in the bathing electrolyte solution plays an important role. Assuming that chloride ions are taken up by the film upon doping as quickly as they are expelled upon dedoping, transient refractive index changes can also occur in the bare electrode regions between adjacent photopolymer grating lines. This process is detailed schematically in Figure 4.14. The initial (undoped) refractive indices of the *poly*-PMDOT-acr/dec film and the bathing electrolyte solution are labeled as F_0 and S_0 , respectively, and the corresponding refractive index difference is labeled $\Delta\eta_0$. Upon oxidative doping, the refractive index of the film falls rapidly to the level designated F_d . Due to the fast uptake of electrolyte anions which this requires, the electrolyte in the grating gaps is initially depleted of anionic species. This electrolyte concentration diminishment causes the refractive index of the bathing solution to fall to the level marked S'_d . The resulting transient refractive index difference $\Delta\eta'_d$ is actually larger in magnitude than $\Delta\eta_0$, and consequently the diffraction efficiency rises. Diffusion of electrolyte anions from the bulk solution quickly replenishes these regions, causing the refractive index of the gaps to return to its initial level and establish the true refractive index difference of the doped film, $\Delta\eta_d$.

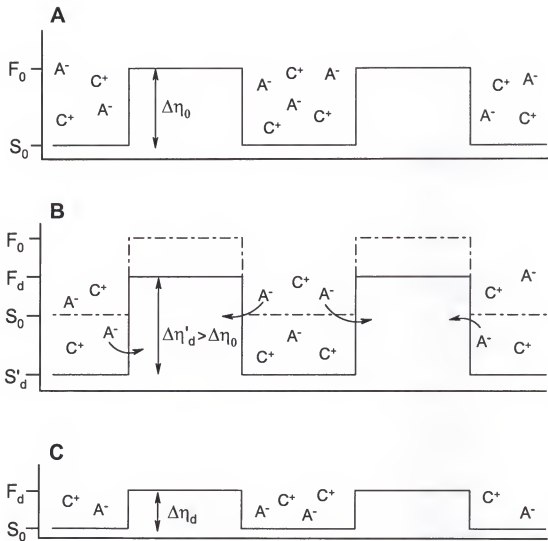


Figure 4.14. Illustration of the refractive index changes occurring during fast electrochemical doping of a grating-patterned *poly-PMDOT-acr/dec* film. In each of the three parts, refractive index is represented by the vertical axis (arbitrary scale; the vertical positions are exaggerated for illustrative purposes), while position along the patterned film is shown along the horizontal axis. The electrolyte cations and anions of the bathing solution are represented as C^+ and A^- , respectively. Part A: relative positions of the refractive indices of the film (F_0) and the bathing solution (S_0) prior to oxidative doping of the film. Part B: refractive index profile immediately after oxidative doping, showing the refractive index of the doped film (F_d) and the transient refractive index of the anion-depleted solution (S'_d) within the grating gaps. Part C: refractive index profile after film doping and replenishment of electrolyte between the polymer lines.

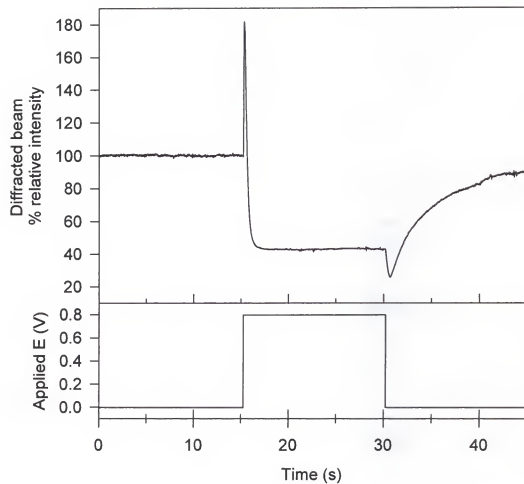


Figure 4.15. Diffraction efficiency modulation in the presence of a highly viscous electrolyte solvent. Conditions: grating-patterned *poly*-PMDOT-acr/dec film, ITO working electrode substrate, 0.0 to 0.8 V vs. Ag wire quasi-reference electrode, 15 s step time, 0.1 M (n-Bu₄N)ClO₄ / propylene carbonate electrolyte.

A few key points must be made here. When these diffracted beam intensity surges were observed, there were no similar features seen in the *undiffracted* beam intensity profiles, indicating that this is clearly not an absorbance effect. In addition, whereas these intensity spikes were observed *in every instance* when a chloride electrolyte salt was used, this phenomenon was not exclusive to chloride. Occasionally this would also be noted in the presence of either perchlorate or hexafluorophosphate salts. However, in these cases the spikes were much shorter-lived, and often required increased digitizer data sampling rates in order to be observed. Finally, this phenomenon can be clearly seen when electrolyte diffusion is retarded by choosing a highly viscous solvent. Shown in Figure 4.15 are the results of a step-diffraction experiment in which 0.1 M tetrabutylammonium perchlorate / propylene carbonate is employed as the bathing electrolyte solution. In this instance, not only can the diffraction efficiency spike be clearly seen upon doping with perchlorate, a similar, but even more sustained spike is observed upon reductive dedoping of the film. In this instance, however, an abundance of expelled anions in the gap regions causes a temporary reduction in the magnitude of $\Delta\eta$, producing an artificially low diffracted beam intensity.

Experimental

Acetonitrile for electrochemical experiments was distilled over calcium hydride prior to use. All other solvents, reagents, and electrolyte salts are reagent grade and used as received without further purification, unless otherwise noted. ^1H and ^{13}C NMR spectra were recorded on a General Electric QE-300 or Varian VXR-300 spectrometer. Elemental analysis was performed by the University of Florida Department of Chemistry Analytical Services. An Integrated Technologies P-6000 spin coater was used for spin

casting of polymer films prior to lithographic exposure. Optical transmission microscope images were obtained using a Nikon F4s 35 mm SLR camera attached to a Nikon Optiphot-POL microscope. Scanning electron microscope images were obtained using a JEOL JSM-6400 SEM at the University of Florida Major Analytical Instrumentation Center.

Syntheses

The synthetic strategy for the PMDOT monomers was based upon modification of previously reported procedures,^{82,88,91} and is outlined in Figure 4.2.

Synthesis of diethyl thiodiglycolate. Thiodiglycolic acid (50 g, 333 mmol) was dissolved in 500 mL of absolute ethanol in a 1 L round-bottom flask with a magnetic stir bar. Concentrated H₂SO₄ (60 mL) was added to the solution slowly while stirring. After final addition of the acid, the solution was refluxed for 24 hours. After the solution was cooled to ambient temperature, 500 mL of H₂O was added and the product was extracted into 400 mL of CHCl₃. The product solution was washed three times with a saturated aqueous solution of sodium bicarbonate and once with H₂O. The solution was dried over anhydrous magnesium sulfate, filtered, and evaporated under reduced pressure to afford the yellow oily liquid product in essentially quantitative yield (68.7 g). ¹HNMR (300 MHz, CDCl₃): δ1.29 (t, 6H), 3.38 (s, 4H), 4.20 (q,4H). Anal. calcd. for C₈H₁₄SO₄: C, 46.59; H, 6.84. Found: C, 46.63; H, 6.92.

Synthesis of 2,3-ethoxycarbonyl-3,4-dihydroxythiophene (4-2). A sodium ethoxide solution (2.17 M) was prepared by dissolving 50 g sodium metal in 1 L absolute ethanol with stirring. 730 mL of this solution was purged with dry nitrogen and cooled on an ice bath. The diethyl thiodiglycolate prepared above (68.7 g, 333 mmol) and

diethyl oxalate (77.86 g, 532.8 mmol) diluted with absolute ethanol were added dropwise while stirring via an addition funnel. After final addition, the reaction mixture was refluxed for 1.5 hours. Upon cooling, the resulting yellow-orange solid was collected by filtration, washed with absolute ethanol until no color was imparted to the filtrate, and partially dried under vacuum at room temperature. This solid, the disodium salt of the desired product (4-1), was divided into three ca. 45 g portions and each was slowly dissolved in 650 mL H₂O. Each solution was acidified with excess concentrated HCl, affording a thick white precipitate which was collected by filtration and partially dried by aspiration. The wet solid was dissolved in CHCl₃ and the resulting two-phase mixture was separated, the CHCl₃ solution was dried over anhydrous MgSO₄, filtered, and evaporated under reduced pressure to yield the beige-colored solid (60.9 g, 70%).

¹HNMR (300 MHz, CDCl₃): δ1.39 (t, 6H), 4.40 (q, 4H), 9.36 (s, 2H). Anal. calcd. for C₁₀H₁₂SO₆: C, 46.15; H, 4.65. Found: C, 46.08; H, 4.55.

Synthesis of PMDOT-OH diester (4-3a/b). In a typical reaction, 2,5-ethoxycarbonyl-3,4-dihydroxythiophene (4-2, 69 g, 265 mmol) was dissolved in 1.5 L absolute ethanol with heating. K₂CO₃ (7.33 g, 53 mmol) and epibromohydrin (47.2 g, 344.7 mmol) were added and the solution was refluxed. After 1.5 hours, a second portion of epibromohydrin (32.7 g, 238.6 mmol) was added. After 15 hours of continuous reflux, additional K₂CO₃ (3.66 g, 26.5 mmol) and epibromohydrin (18.2 g, 132.5 mmol) were added, and reflux was continued for a total of 48 hours. After cooling to room temperature, the mixture was poured over ca. 500 mL of each H₂O and saturated aqueous NaCl, and the product was extracted into CHCl₃. The solution was dried over anhydrous MgSO₄, filtered, and evaporated under reduced pressure to yield a dark brown

oil, which slowly solidified over the course of 1-2 hours. The product was purified either by column chromatography on silica, eluting with 30% CH₃CN/CHCl₃, or recrystallization from ethanol/H₂O. The latter method produced a slightly higher yield (64 g, 77%). The product of this reaction is a mixture of two isomers, a six-membered and a seven-membered ring product, as shown in Figure 4.x. Although these could conceivably be separated by column chromatography, no effort was made to do so.

¹HNMR (300 MHz, CDCl₃): δ1.36 (t, ester -CH₃), 1.91 (s, 4-3b -OH), 2.96 (t, 4-3a -OH), 3.93 (m, ~2H), 4.35 (q, 4H), 4.25-4.6 (m, ~3H). Anal. calcd. for C₁₃H₁₆SO₇: C, 49.36; H, 5.10. Found: C, 49.32; H, 5.08.

Synthesis of PMDOT-OH diacid (4-4a/b). PMDOT-OH diester (4-3a/b) was saponified in three ca. 20 g portions by dissolving and refluxing each in 250 mL 10 % aqueous NaOH for 2-3 hours. After cooling to room temperature, the solutions were acidified with concentrated HCl while stirring on an ice bath. The product slowly precipitated out of the ice cold acidic solution and was collected by filtration and washed with ice-cold H₂O. The wet solid was dissolved in absolute ethanol, dried over anhydrous MgSO₄, filtered, and evaporated under reduced pressure to afford the light gray solid product (38.5 g, 67%). ¹HNMR (300 MHz, CD₃OD): δ3.83 (d, 2H), 4.2 (dd, 1H), 4.3-4.4 (m, 3H), 4.47 (dd, 1H). Anal. calcd. for C₉H₈SO₇: C, 41.54; H, 3.10. Found: C, 41.49; H, 3.08.

Synthesis of PMDOT-OH (4-5a/b). PMDOT-OH diacid (4-4a/b, 10 g, 38.4 mmol), barium-promoted copper chromite catalyst (Acros, 4.0 g), and quinoline (100 mL) were added to a flask and flushed thoroughly with dry nitrogen. The mixture was stirred and heated to ca. 180° for 30 hours under a nitrogen purge. After cooling, the

mixture was diluted with ether and the insoluble catalyst was removed by filtration on a glass frit and washed with ether. The filtrate was washed repeatedly with 1.0 M HCl, 1.0 M NaOH, and H₂O, dried over anhydrous MgSO₄, filtered, and evaporated under reduced pressure to yield a viscous brown oil (2.96 g, 45%). ¹HNMR (300 MHz, CDCl₃): δ4.09 (ddd, 1H), 4.21 (dd, 1H), 4.22-4.28 (m, 3H), 6.38 (dd, 2H). Anal. calcd. for C₇H₈SO₃: C, 48.83; H, 4.68. Found: C, 48.84; H, 4.64.

Synthesis of PMDOT acrylate (PMDOT-acr, two isomers). PMDOT-OH (4-5a/b, 2.96 g, 17.2 mmol) was dissolved in 80 mL CH₂Cl₂ which was freshly dried and distilled over calcium hydride. Triethylamine (3.48 g, 34.4 mmol) was added with stirring, followed by dropwise addition of acryloyl chloride (7.78 g, 86 mmol, Aldrich). The reaction flask was flushed thoroughly with dry nitrogen, and the solution was stirred under a nitrogen purge at room temperature for 4 hours. The reaction mixture was transferred to a separatory funnel and washed repeatedly with 1.0 M HCl, saturated aqueous NaHCO₃, and H₂O. The solution was dried over anhydrous MgSO₄, filtered, and evaporated under reduced pressure to yield a yellow-orange oil. The product was purified by chromatography on silica, eluting with CHCl₃ or 12-25% ether / petroleum ether, affording a viscous yellow oil (1.21 g, 31%). ¹HNMR (300 MHz, CDCl₃): δ4.06 (dd, 1H), 4.25 (dd, 1H), 4.35-4.47 (m, 3H), 5.89 (dd, 1H), 6.17 (dd, 1H), 6.36 (dd, 2H), 6.46 (dd, 1H).

Synthesis of PMDOT decanoate (PMDOT-dec, two isomers). PMDOT-OH (4-5a/b, 1.0 g, 5.81 mmol) was dissolved in 30 mL CH₂Cl₂ which was freshly dried and distilled over calcium hydride. Triethylamine (1.18g, 11.6 mmol) was added with stirring, followed by dropwise addition of decanoyl chloride (5.54 g, 29 mmol). An

additional 10 mL CH₂Cl₂ was added to dissolve the thick solid formed upon addition of the acid chloride. The flask was purged with nitrogen and stirred at room temperature for 4 hours under a nitrogen purge. Workup and purification were the same as for the acrylate above, yielding a thin yellow oil (1.3 g, 69%). ¹HNMR (300 MHz, CDCl₃): δ0.88 (t, 3H), 1.2-1.4 (m, 12H), 1.63 (m, 2H), 2.36 (t, 2H), 4.04 (dd, 1H), 4.2-4.45 (m, 4H), 6.35 (dd, 2H). Anal. calcd. for C₁₇H₂₆SO₄: C, 62.55; H, 8.03. Found: C, 62.65; H, 8.11.

Synthesis of poly-PMDOT-acr/dec. A typical procedure for the preparation of poly-PMDOT-acr/dec (2:3 ratio) is as follows: to a 25 mL round-bottom flask with a magnetic stir bar was added PMDOT-acr (50 mg, 0.221 mmol), PMDOT-dec (108 mg, 0.331 mmol), anhydrous FeCl₃ (134 mg, 0.828 mmol), and 15 mL freshly dried and distilled acetonitrile. The flask was purged with nitrogen, sealed with a rubber septum, and stirred at room temperature for 2 hr. After this time, the reaction mixture was poured over 200 mL of methanol, precipitating the deep blue doped polymer. This solid was collected by filtration, washed with methanol, and transferred to a 50 mL flask containing 15 mL each of chloroform and concentrated aqueous NH₄OH. The mixture was stirred vigorously for 2 hr, during which time the dedoped polymer dissolved in the chloroform, lending it a deep purple color. Any remaining undissolved solid was removed by filtration, and the two phase mixture was transferred to a separatory funnel and the aqueous phase removed. The chloroform solution was then sequentially washed once with 1.0 M HCl, twice with 0.1 M HCl, three times with saturated aqueous NaCl, and three times with water. Often during the initial washing procedures, a thick, persistent emulsion formed, which required the addition of a saturated NaCl solution to the funnel

in order to facilitate phase separation. After washing, the solution was dried over anhydrous $MgSO_4$ and filtered, the solvent was removed by rotary evaporation, and the dark purple solid was weighed (yield = 34 mg, 22%). Gel permeation chromatography (GPC) characterization of these materials indicate rather low molecular weights and broad polydispersity indices: M_w 2500-3800, M_n 1100-2500, PDI 1.6-2.7. If the solid was allowed to dry completely (i.e. under vacuum or by prolonged storage), addition of chloroform failed to redissolve the bulk of the material. For this reason, immediately after weighing, the polymer was dissolved in 2-3 mL of chloroform for storage and subsequent spin-casting.

Electrochemical/Optical Experiments

Indium-tin oxide (ITO) glass optically transparent electrodes (Delta Technologies, Stillwater, MN) are used as the substrate for photopolymer film fabrication. Cyclic voltammograms are recorded using a Bioanalytical Systems CV-27 voltammograph in conjunction with an ADInstruments MacLab/4e analog-to-digital converter and electrochemical software. All reported potentials are relative to a Ag wire quasi-reference electrode ($\approx +0.05$ V vs. SSCE in 0.1 M (n-Bu₄N)PF₆/CH₃CN) which is employed due to space constraints in the electrochemical cell used for the optical studies. The electrolyte solutions used for the experiments are 0.1 M solutions of tetrabutylammonium chloride, perchlorate, or hexafluorophosphate in acetonitrile. UV-visible absorbance is measured using a Hewlett-Packard 8452A diode-array spectrophotometer. Spectroelectrochemical experiments are performed using the HP 8452A in conjunction with the BAS CV-27 voltammograph. Instrumentation used for optical diffraction studies is described in the Appendix.

Film Preparation/Lithographic Patterning

Since the PMDOT polymer was stored dissolved in chloroform, both the polymer and initiator were measured and dispensed as stock solutions. In contrast to the *poly*-RuAAP and *poly*-VBF²⁺ photopolymer films, no PETA crosslinking agent was used. The photoinitiator stock solution was prepared by dissolving 0.021 g of benzoin ethyl ether in 1 mL of chloroform. Typical spin-coating solutions were prepared by mixing 20 μ L of the *poly*-PMDOT-acr/dec solution (ca. 30 mg/ml) and 10 μ L of the BEE stock solution. The ITO substrate was placed in the spin-coater and spun at 3000-4000 rpm while 10-15 μ L of the polymer/initiator solution was added dropwise to the center of the spinning substrate in 5 μ L increments via an autopipet. The film was allowed to dry in ambient air for several minutes and then placed in direct contact with the chrome surface of a lithographic mask (USAF target or grating-patterned, Rolyn Optics). The film was irradiated face-on through the mask with a Pyrex-filtered medium-pressure mercury lamp (intensity \approx 60 mW-cm⁻²) at a distance of ca. 1 in. for 2 minutes. Following exposure, the coated substrate was removed from the mask and developed by immersion and gentle agitation in o-dichlorobenzene for 15-20 s, and dried under a gentle stream of nitrogen. If the feature resolution of the patterned film was unsatisfactory (background film in unirradiated areas, as determined by optical microscopy), it could often be improved by prolonged (1-2 min.) immersion in chloroform.

Electropolymerization.

Unpatterned films of *poly*-PMDOT-acr were prepared by anodic electro-polymerization of PMDOT-acr monomer for comparison of the cyclic voltammetric properties to those of the lithographically prepared films. An ITO substrate was placed in

the electrochemical cell used for the diffraction studies (see Appendix), and the cell was filled with a 5 mM solution of PMDOT-acr in 0.1 M (n-Bu₄N)ClO₄ / acetonitrile. The polymer was deposited on the working electrode by cycling the applied potential between -1.0 and +1.8 V vs. Ag wire (10 scans) at a scan rate of 100 mV·s⁻¹. The electrode was removed from the cell and rinsed with clean acetonitrile, producing a circular film (diameter \approx 0.0396 cm²) with a slightly microcrystalline appearance.

APPENDIX INSTRUMENTATION FOR DIFFRACTION STUDIES

The experimental instrumentation used for the electrochemically modulated diffraction efficiency experiments described in Chapters 2-4 is shown in Figure A.1. All experiments were performed using the same instrumentation, unless otherwise noted.

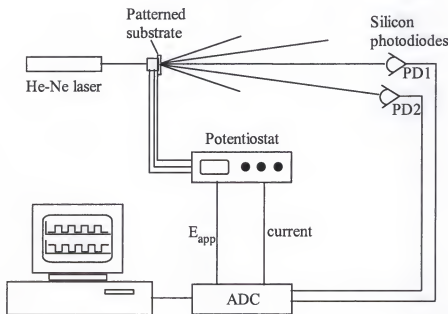


Figure A.1. Instrumentation for diffraction studies.

Diffraction experiments are conducted using a He-Ne laser (Chapter 2: Aerotech, 5 mW; Chapters 3 and 4: Aerotech Synchrolase 100 series, 0.5 mW, frequency and amplitude stabilized) as the illumination source. An electrochemical cell (Figure A.2)

was constructed in-house which provides an open light path for the incident laser beam and the exiting diffracted beams of several orders of diffraction. The cell body is constructed of teflon with a horizontally-bored electrolyte solution chamber sealed at the front face with a quartz window. To the rear is mounted the grating-patterned indium-tin oxide (ITO) optically transparent electrode (OTE) and a Viton seal, which serve as the window for the emerging diffracted light. The aperture in the Viton seal determines the electroactive area of the photopolymer film in contact with the electrolyte solution. The platinum wire auxiliary and silver wire quasi-reference ($\approx +0.05$ V vs. SSCE in 0.1 M (n-Bu₄N)PF₆/CH₃CN) electrodes are inserted through a rubber septum placed in a vertical bore which intersects with the electrolyte solution chamber, and all three electrodes are connected to a potentiostat (Bioanalytical Systems CV-27 voltammograph). The grating-patterned ITO substrate is mounted such that the ITO/photopolymer film surface is in contact with the electrolyte solution, either 0.1 M (n-Bu₄N)PF₆/CH₂Cl₂ (Chapter 2), 0.1 M (n-Bu₄N)PF₆/DMF (Chapter 3), 0.1 M (n-Bu₄N)Cl/DMF (Chapter 3), 0.1 M (n-Bu₄N)PF₆/CH₃CN (Chapter 4), 0.1 M (n-Bu₄N)ClO₄/CH₃CN (Chapter 4), or 0.1 M (n-Bu₄N)Cl/CH₃CN (Chapter 4).

The intensities of the zero-order undiffracted beam and one first-order diffracted beam are monitored using two matched silicon photodiodes (Motorola), which are each powered by four AA dry cells in series and connected with a reverse potential bias (Figure A.3). Adjustable gain of the diode output was achieved by connection of a fixed and a variable resistor wired in a voltage divider configuration. To minimize output signal drift resulting from variations in ambient air temperature, the photodiodes are each mounted in a brass plate which has water from a temperature-controlled bath flowing

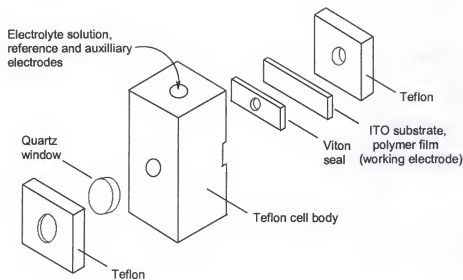


Figure A.2. Electrochemical cell used for diffraction experiments and electrochemical characterization of photopolymer films.

through chambers surrounding the photodiode (Chapters 3 and 4 only). To eliminate extraneous noise from stray light, optical filters which pass only a narrow band centered at the He-Ne laser wavelength (632.8 nm) are placed in front of the photodiodes. Neutral-density filters are used to attenuate the impinging light in order to avoid saturation of the photodiode response, i.e. to assure linearity of the output voltage with illumination intensity.

The positive analog voltage output signals from the two photodiodes (relative to each negative output at ground) are digitized by an analog-to-digital converter (ADC, Chapter 2: LabPC+, National Instruments; Chapters 3 and 4: MacLab/4e, ADInstruments), and collected, stored, and analyzed by computer (Chapter 2: 80286 PC; Chapters 3 and 4: Macintosh Centris). Electrochemical control of the applied potential to the working electrode is provided by a potentiostat (Chapter 2: BAS CV-27 alone; Chapters 3 and 4: BAS CV-27 in conjunction with MacLab/4e and ADInstruments electrochemical software), and the applied potential and current output signals are also digitized and collected by computer.

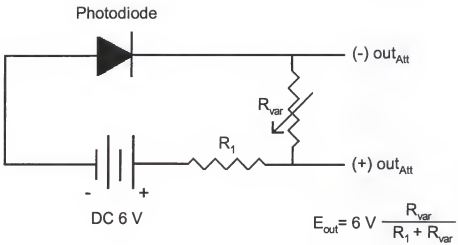


Figure A.3. Schematic representation of photodiode connected with reverse potential bias and adjustable gain. The potential difference between $(+)$ out and $(-)$ out is linearly proportional to the intensity of the light impinging upon the photodiode.

REFERENCES

1. Murray, R. W. *Electroanalytical Chemistry*; Bard, A. J., Ed.; Marcel Dekker: New York, 1984; Vol. 13, pp 191-368.
2. Murray, R. W. *Molecular Design of Electrode Surfaces*; Murray, R. W., Ed.; Wiley Interscience: New York, 1992; Vol. 22, pp 1-48.
3. Ellis, C. D.; Meyer, T. J. *Inorganic Chemistry* 1984, 23, 1748-1756.
4. Gould, S.; Leasure, R. M.; Meyer, T. J. *Chemistry in Britain* 1995, 31, 891-893.
5. Leasure, R. M.; Ou, W.; Moss, J. A.; Linton, R. W.; Meyer, T. J. *Chemistry of Materials* 1996, 8, 264-273.
6. Bookbinder, D. C.; Wrighton, M. S. *Journal of the American Chemical Society* 1980, 102, 5123-5125.
7. Cosiner, S.; Deronzier, A.; Moutet, J.-C. *Journal of Physical Chemistry* 1985, 89, 4895-4897.
8. Facci, J. S. *Langmuir* 1987, 3, 525.
9. Zhang, X.; Bard, A. J. *Journal of the American Chemical Society* 1989, 111, 8098.
10. Matsuda, H.; Aoki, J.; Tokuda, K. *Journal of Electroanalytical Chemistry* 1987, 217, 15.
11. Lane, R. F.; Hubbard, A. T. *Journal of Physical Chemistry* 1973, 77, 1401.
12. Brown, A. P.; Anson, F. C. *Journal of Electroanalytical Chemistry* 1977, 83, 203.
13. Gorman, C. B.; Biebuyck, H. A.; Whitesides, G. M. *Chemistry of Materials* 1995, 7, 252-254.
14. Frisbie, C. D.; Martin, J. R.; Duff, R. R., Jr.; S. Wrighton, M. *Journal of the American Chemical Society* 1992, 114, 7142-7145.

15. Rozsnyai, L. F.; Wrighton, M. S. *Langmuir* **1995**, *11*, 3913-3920.
16. Rozsnyai, L. F.; Wrighton, M. S. *Chemistry of Materials* **1996**, *8*, 309-311.
17. Weisshaar, D. E.; Lamp, B. D.; Porter, M. D. *Journal of the American Chemical Society* **1992**, *114*, 5860-5862.
18. Moses, P. R.; Wier, L.; Murray, R. W. *Analytical Chemistry* **1975**, *47*, 1882-1886.
19. Lenhard, J. R.; Murray, R. W. *Journal of Electroanalytical Chemistry* **1977**, *78*, 195-201.
20. Dulcey, C. S.; Georger, J. H., Jr.; Krauthamer, V.; Stenger, D. A.; Fare, T. L.; Calvert, J. M. *Science* **1991**, *252*, 551-554.
21. Fodor, S. P. A.; Read, J. L.; Pirrung, M. C.; Stryer, L.; Lu, A. T.; Solas, D. *Science* **1991**, *251*, 767-773.
22. von Kiederowski, G. *Angewandte Chemie-International Edition in English* **1991**, *30*, 822-823.
23. Kang, D.; Wrighton, M. S. *Langmuir* **1991**, *7*, 2169-2174.
24. Rozsnyai, L. F.; Benson, D. R.; Fodor, S. P. A.; Schultz, P. G. *Angewandte Chemie-International Edition in English* **1992**, *31*, 759-761.
25. Bhatia, S. K.; Hickman, J. J.; Ligler, F. S. *Journal of the American Chemical Society* **1992**, *114*, 4432-4433.
26. Dulcey, C. S.; Georger, J. H., Jr.; Chen, M.-S.; McElvany, S. W.; O'Ferrall, C. E.; Benezra, V. I.; Calvert, J. M. *Langmuir* **1996**, *12*, 1638-1650.
27. Surridge, N. A.; McClanahan, S. F.; Hupp, J. T.; Danielson, E.; Gould, S.; Meyer, T. J. *Journal of Physical Chemistry* **1989**, *93*, 294-304.
28. Surridge, N. A.; Hupp, J. T.; McClanahan, S. F.; Gould, S.; Meyer, T. J. *Journal of Physical Chemistry* **1989**, *93*, 304-313.
29. Bard, A. J.; Faulkner, L. R. *Electrochemical Methods: Fundamentals and Applications*; John Wiley & Sons: New York, 1980.
30. *Electroactive Polymer Electrochemistry*; Plenum Press: New York, 1994.
31. Venugopal, G.; Quan, X.; Johnson, G. E.; Houlihan, F. M.; Chin, E.; Nalamasu, O. *Chemistry of Materials* **1995**, *7*, 271-276.

32. *Introduction to Microlithography*; 2nd ed.; American Chemical Society: Washington, DC, 1994.
33. Fayer, M. D. *Annual Reviews in Physical Chemistry* **1982**, *33*, 63-87.
34. Nelson, K. A.; Casalegno, R.; Miller, R. J. D.; Fayer, M. D. *Journal of Chemical Physics* **1982**, *77*, 1144-1152.
35. Jenkins, F. A.; White, H. E. *Fundamentals of Optics*; 3rd ed.; McGraw-Hill: New York, 1957.
36. Rossi, B. B. *Optics*; Addison-Wesley: Reading, Mass, 1957.
37. Hutley, M. C. *Diffraction Gratings*; Academic Press: New York, 1982; Vol. 6.
38. Meyer, T. J. *Accounts of Chemical Research* **1978**, *11*, 94-100.
39. Rillema, D. P.; Dressick, W. J.; Meyer, T. J. *Journal of the Chemical Society, Chemical Communications* **1980**, 247-248.
40. DeLaive, P. J.; Sullivan, B. P.; Meyer, T. J.; Whitten, D. G. *Journal of the American Chemical Society* **1979**, *101*, 4007-4008.
41. Dressick, W. J.; Meyer, T. J.; Durham, B.; Rillema, D. P. *Inorganic Chemistry* **1982**, *21*, 3451-3458.
42. Leasure, R. M.; Moss, J. A.; Meyer, T. J. *Inorganic Chemistry* **1994**, *33*, 1247-1248.
43. Abruna, H. D.; Denisevich, P.; Umana, M.; Meyer, T. J.; Murray, R. W. *Journal of the American Chemical Society* **1981**, *103*, 1-5.
44. Nagle, J. K.; Bernstein, J. S.; Young, R. C.; Meyer, T. J. *Inorganic Chemistry* **1981**, *20*, 1760-1764.
45. Durham, B.; Dresick, W. J.; Meyer, T. J. *Journal of the Chemical Society, Chemical Communications* **1979**, 381-382.
46. Westmoreland, T. D.; Calvert, J. M.; Murray, R. W.; Meyer, T. J. *Journal of the Chemical Society, Chemical Communications* **1983**, 65-66.
47. Black, K. J.; Huang, H.; High, S.; Starks, L.; Olson, M.; McGuire, M. E. *Inorganic Chemistry* **1993**, *32*, 5591-5596.
48. Hauser, B. T.; Bergstedt, T. S.; Schanze, K. S. *Journal of the Chemical Society, Chemical Communications* **1995**, 1945-1946.

49. Schanze, K. S.; Bergstedt, T. S.; Hauser, B. T. *Advanced Materials* **1996**, *8*, 531-534.
50. Bergstedt, T. S.; Hauser, B. T.; Schanze, K. S. *Journal of the American Chemical Society* **1994**, *116*, 8380-8381.
51. Schanze, K. S.; Bergstedt, T. S.; Hauser, B. T. *Proceedings, Polymeric Materials: Science and Engineering* **1995**, *72*, 561-562.
52. Roffey, C. G. *Photopolymerization of Surface Coatings*; John Wiley & Sons: New York, 1982.
53. Wicks, Z. W., Jr.; Jones, F. N.; Pappas, S. P. *Organic Coatings: Science and Technology*; John Wiley & Sons: New York, 1994; Vol. 2.
54. Durham, B.; Caspar, J. V.; Nagle, J. K.; Meyer, T. J. *Journal of the American Chemical Society* **1982**, *104*, 4803-4810.
55. Leung, A. F.; George, S. *American Journal of Physics* **1989**, *57*, 854-856.
56. Lewis, T. J.; White, H. S.; Wrighton, M. S. *Journal of the American Chemical Society* **1984**, *106*, 6947-6952.
57. Kepley, L. J.; Bard, A. J. *Journal of the Electrochemical Society* **1995**, *142*, 4129-4138.
58. Hauser, B. T. Ph.D. Dissertation, University of Florida, 1996.
59. Smith, G. F.; F William Cagle, J. *Journal of Organic Chemistry* **1947**, *12*, 781-783.
60. Gillard, R. D.; Hill, R. E. E. *Journal of the Chemical Society, Dalton Transactions* **1974**, 1217-1236.
61. Bird, C. L.; Kuhn, A. T. *Chemical Society Reviews* **1981**, *10*, 49-82.
62. Van Emon, J.; hammock, B.; Seiber, J. N. *Analytical Chemistry* **1986**, *58*, 1866-1873.
63. Margerum, L. D.; Murray, R. W.; Meyer, T. J. *Journal of Physical Chemistry* **1986**, *90*, 728-730.
64. Bock, C. R.; Connor, J. A.; Gutierrez, A. R.; Meyer, T. J.; Whitten, D. G.; Sullivan, B. P.; Nagle, J. K. *Journal of the American Chemical Society* **1979**, *101*, 4815-4824.

65. Denisevich, P.; Willman, K. W.; Murray, R. W. *Journal of the American Chemical Society* **1981**, *103*, 4727-4737.
66. Park, J. Y.; Lee, S. B.; Park, Y. S.; Park, Y. W.; Lee, C. H.; Lee, J. I.; Shim, H. K. *Applied Physics Letters* **1998**, *72*, 2871-2873.
67. Stepp, J.; Schlenoff, J. B. *Journal of the Electrochemical Society* **1997**, *144*, L155-L157.
68. Dominey, R. N.; Lewis, T. J.; Wrighton, M. S. *Journal of Physical Chemistry* **1983**, *87*, 5345-5354.
69. Kim, J.-H.; Lee, K. A. B.; Uphaus, R. A.; Cotton, T. M. *Thin Solid Films* **1992**, *210/211*, 825-827.
70. Bidan, G.; Deronzier, A.; Moutet, J.-C. *Journal of the Chemical Society, Chemical Communications* **1984**, 1185.
71. Shu, C.-F.; Wrighton, M. S. *Journal of Physical Chemistry* **1988**, *92*, 5221-5229.
72. Lapkowski, M.; Bidan, G. *Journal of Electroanalytical Chemistry* **1993**, *362*, 249-256.
73. Hatozaki, O.; Ohsaka, T.; Oyama, N. *Journal of Physical Chemistry* **1992**, *96*, 10492-10497.
74. Dalton, E. F.; Murray, R. W. *Journal of Physical Chemistry* **1991**, *95*, 6383-6389.
75. Terrill, R. H.; Hutchison, J. E.; Murray, R. W. *Journal of Physical Chemistry B* **1997**, *101*, 1535-1542.
76. Kosower, E. M.; Cotter, J. L. *Journal of the American Chemical Society* **1964**, *86*, 5524-5527.
77. DeLong, H. C.; Buttry, D. A. *Langmuir* **1992**, *8*, 2491-2496.
78. Tang, X.; Schneider, T. W.; Walker, J. W.; Buttry, D. A. *Langmuir* **1996**, *12*, 5921-5933.
79. Lee, C.; Lee, Y. M.; Moon, M. S.; Park, S. H.; Park, J. W.; Kim, K. G.; Jeon, S.-J. *Journal of Electroanalytical Chemistry* **1996**, *416*, 139-144.
80. Kutsche, C.; Targrove, J.; Haaland, P. *Journal of Applied Physics* **1993**, *73*, 2602-2604.

81. Yu, G.; Zhang, C.; Pakbaz, K.; Heeger, A. J. *Synthetic Metals* **1995**, *71*, 2241-2242.
82. Blohm, M. L.; Pickett, J. E.; VanDort, P. C.; Park, C. *Substituted 3,4-polymerized methylenedioxythiophenes and polymers and electroresponsive devices made therefrom*; General Electric Company: United States, 1992.
83. Kumar, A.; Welsh, D. M.; Morvant, M. C.; Piroux, F.; Abboud, K. A.; Reynolds, J. R. *Chemistry of Materials* **1998**, *10*, 896-902.
84. Sapp, S. A.; Sotzing, G. A.; Reynolds, J. R. *Chemistry of Materials* **1998**, *10*, 2101-2108.
85. Chao, S.; Wrighton, M. S. *Journal of the American Chemical Society* **1987**, *109*, 2197-2199.
86. Levesque, I.; Leclerc, M. *Journal of the Chemical Society, Chemical Communications* **1995**, 2293-2294.
87. Lowe, J.; Holdcroft, S. *Macromolecules* **1995**, *28*, 4608-4616.
88. Pei, Q.; Zuccarello, G.; Ahlskog, M.; Inganäs, O. *Polymer* **1994**, *35*, 1347-1351.
89. Dietrich, M.; Heinze, J.; Heywang, G.; Jonas, F. *Journal of Electroanalytical Chemistry* **1994**, *369*, 87-92.
90. Havinga, E. E.; Mutsaers, C. M. J.; Jenneskens, L. W. *Chemistry of Materials* **1996**, *8*.
91. Sankaran, B.; Reynolds, J. R. *Macromolecules* **1997**, *30*, 2582-2588.
92. Sotzing, G. A.; Reynolds, J. R.; Steel, P. J. *Advanced Materials* **1997**, *9*, 795-798.
93. Pomerantz, M.; Tseng, J. J.; Zhu, H.; Sproull, S. J.; Reynolds, J. R.; Uitz, r.; Arnott, H. J.; Haider, M. I. *Synthetic Metals* **1991**, *41-43*, 825-830.
94. Roncali, J. *Chemical Reviews* **1992**, *92*, 711-738.
95. Chung, T.-C.; Kaufman, J. H.; Heeger, A. J.; Wudl, F. *Physical Review B* **1984**, *30*, 702-710.
96. Kaneto, K.; Kohno, Y.; Yoshino, K. *Solid State Communications* **1984**, *51*, 267-269.
97. Sasaki, K.; Nagamura, T. *Applied Physics Letters* **1997**, *71*, 434-436.

98. Sotzing, G. A.; Reynolds, J. R. *Chemistry of Materials* **1996**, *8*, 882-889.

BIOGRAPHICAL SKETCH

Troy Scott Bergstedt was born and raised in northern Minnesota, just a stone's throw from Duluth. Most of his youth was spent wandering through the woods behind his parents' house, developing a love for the great outdoors which endures to the present.

After graduation from Esko High School in 1987, he spent the next four years commuting just across the bridge to attend college at the University of Wisconsin-Superior. It was here where this aimless youth discovered his knack for chemistry (between hands of rummy in the Student Center). Between his third and fourth years of college, he spent the summer in sunny southern California pursuing undergraduate research under the tutelage of Professor Nicos Petasis. It was this experience that convinced him to pursue further study after receiving his Bachelor of Science degree in 1991.

The next several years were spent honing his skills in the Schanze lab, learning how to endure a winter without snow and discovering the soul-soothing rhymes of Jimmy Buffett. It was during this time that he was finally able to 'catch' the blonde girl he'd had his eye on since first grade, and he proudly made her his wife.

Since leaving the University of Florida, Troy has been expanding his chemical horizons working in the lab of Professor Guillermo Bazan, and discovering that the more he knows about chemistry, the more he needs to know about chemistry.

I certify that I have read this study and that in my opinion it conforms to acceptable standards of scholarly presentation and is fully adequate, in scope and quality, as a dissertation for the degree of Doctor of Philosophy.

Kirk S. Schanze
Kirk S. Schanze, Chairman
Professor of Chemistry

I certify that I have read this study and that in my opinion it conforms to acceptable standards of scholarly presentation and is fully adequate, in scope and quality, as a dissertation for the degree of Doctor of Philosophy.

William R. Dolbier
William R. Dolbier, Jr.
Professor of Chemistry

I certify that I have read this study and that in my opinion it conforms to acceptable standards of scholarly presentation and is fully adequate, in scope and quality, as a dissertation for the degree of Doctor of Philosophy.

J. Eric Enholm
J. Eric Enholm
Associate Professor of Chemistry

I certify that I have read this study and that in my opinion it conforms to acceptable standards of scholarly presentation and is fully adequate, in scope and quality, as a dissertation for the degree of Doctor of Philosophy.

David E. Richardson
David E. Richardson
Professor of Chemistry

I certify that I have read this study and that in my opinion it conforms to acceptable standards of scholarly presentation and is fully adequate, in scope and quality, as a dissertation for the degree of Doctor of Philosophy.

Peter G. Ifju
Peter G. Ifju
Assistant Professor of Aerospace
Engineering, Mechanics and
Engineering Science

This dissertation was submitted to the Graduate Faculty of the Department of Chemistry of the College of Liberal Arts and Sciences and to the Graduate School and was accepted as partial fulfillment of the requirements for the degree of Doctor of Philosophy.

August, 1999

Dean, Graduate School